A STUDY OF RARE EARTH DOPED SILICATE AND PHOSPHATE GLASSES

A THESIS SUBMITTED TO

THE UNIVERSITY OF KENT AT CANTERBURY

IN THE SUBJECT OF PHYSICS

FOR THE DEGREE

OF DOCTOR OF PHILOSOPHY.

By

Daniel Timothy Bowron

September 1994

Abstract

The complementary techniques of X-ray diffraction and EXAFS have been applied to silicate and phosphate glass systems containing varying quantities of rare earth elements.

The silicate systems that have been studied are rare earth doped fibre optic preforms of interest to the optoelectronics and telecommunications industry. Techniques were developed to allow spatially resolved diffraction and EXAFS data to be taken from the small $\sim$1mm diameter core region of the preforms. Absorption maps were made displaying the distribution of the rare earth ions as a function of radial position, and similarly for the germanium codopant incorporated in these systems. The diffraction results show as expected, that silica dominates the structure evident in the preforms whilst EXAFS measurements taken at the germanium K-edge, suggest that this codopant occupies an eightfold coordinated site surrounded by oxygen atoms at 1.7Å.

The phosphate glasses studied are rare earth metaphosphates of the composition $R(PO_3)_3$. X-ray diffraction measurements were taken showing that the network structure of these systems is essentially constructed from PO_4 tetrahedra. The EXAFS experiments, performed on a range of glasses over the rare earth L_{III} edges, show a trend in the first shell distance rare earth-oxygen, consistent with the Lanthanide contraction, the rare earth ions occupying sites with between six and eight-fold coordination of oxygen atoms about the rare earth ions.

Acknowledgements

I would like to thank the many people who have helped and guided me throughout the duration of my studies: firstly my supervisor Dr. Bob Newport for giving me the opportunity and being a fount of worthwhile suggestions each of the many times I ran aground; Dr. Eleanor Tarbox of Pirelli Cables Ltd. who has helped keep my optics knowledge in the realms of reality; Professor George Saunders and Professor Brian Rainford for the opportunity to climb aboard the phosphate project, a subject that restored my faith in science; Dr. Steve Gurman who's help with the EXAFS was invaluable; Mr. Menno Oversluizen and Dr. Graham Bushnell-Wye the 8.1 and 9.1 station masters respectively; Dr. Dave Huxley who helped me sort out the diffraction; Dr. Bernard Hurle for preparing my samples and Mr. Don Riley for being a genius in the workshop.

Of the many characters at the university, to add colour to the last three years I would like to mention the scattering group, its members both past and present especially Adriano, Ashley, Benoit, Chris, Dave, Ian, Jane, Jennifer, Jon, Michelle, Paul, Stuart and Theresa; Alan Chadwick and his chemistry crew (No, it isn't a vanity case!) and Phil and the other theoreticians who made room 8 such an interesting place to visit.

Several of my friends deserve particular mention for without their help and support, I doubt I would ever have finished: Adam, Wendy, Ian and Jessica who shared the unforgettable experience of life in Parkwood - the kitchen, the characters and... the unusual bathroom implements and, Ian and Sue with whom I've shared the trials and tribulations of life in the rented sector.

Last but by no means least, I wish to thank my parents and brother for being there whenever I needed them.

I would like to acknowledge The University of Kent at Canterbury and Pirelli Cables Ltd. for the financial support that made this work possible and DRAL for access to their synchrotron, a most vital part in this research.

Contents

List of Tables

List of Figures

Chapter 1

Oxide Glasses

Interest in the structure of oxide glasses such as phosphate and silicate systems i.e. with P_2O_5 and SiO_2 base units respectively, has recently increased. This is mainly due to the wide range of uses that these materials may be put to in the field of optoelectronics and optical communications; they are especially important in the manufacture of fibre optic cable and devices such as fibre lasers, fibre sensors and optical amplifiers. These kinds of glasses are imbued with novel properties by the inclusion of dopant atoms such as rare earths into the base glass network; these dopant atoms provide suitable electronic states to support phenomena such as lasing. Rare earth dopants in high concentrations can also lead to the final glasses possessing remarkable magnetic properties along with the optical phenomena, again due to their electron configuration.

Before progressing to doped glass systems it is useful to consider the simple undoped materials, pure vitreous silica and phosphate glass, and also the models which are currently used to describe them, notably the Continuous Random Network or CRN, and the paracrystallite models.

1.1 Vitreous Silica

The atomic structure of vitreous silica is a contentious topic, as is the structure of most amorphous systems, for which no wholly satisfactory solution has yet been found. Various structural models have been developed but none as yet can describe all of the properties these materials display. The study of amorphous systems such as $v - SiO_2$ is pursued using many experimental techniques, for example neutron and X-ray diffraction, Nuclear Magnetic Resonance, Infra Red spectroscopy etc. each of which allows the study of particular physical characteristics of the material. Due to the nature of an amorphous solid, no individual technique can provide all of the information required to fully characterise the system, results being of a statistical ilk to account for the average bulk structure of a randomly oriented network of molecules.

When studying amorphous materials, the best approach is the use of a cocktail of techniques to probe specific properties of the material, for example, its short range atomic structure, its atomic network vibrational properties, its medium range network structure etc.. Then attempt to coalesce the information gained into a larger picture of the overall structure.

Short range structural methods probe the base molecular environment for distortion of bond angles from those predicted by crystalline structural studies, and atomic coordination numbers of the constituent atoms. This usually corresponds to a length scale out to perhaps 4 or 5 Ångströms. Medium range properties, present on a length scale of 5 to 15Å include structure due to features such as molecular rings or chains. From the definition of an amorphous material, no long range order is present, i.e. no infinite crystal lattice or similar correlations and therefore the study of large length scales is fruitless in yielding anything other than bulk properties such as density.

The morphological study of amorphous materials is greatly aided by the use of

model structures, for which physical properties can be calculated and compared with the results of experiment. These networks have been created in many ways, the most laborious being construction by hand, but with the advent of modern computational devices this process of model construction has been greatly enhanced. Many models now exist, but a completely satisfactory structure has not yet been found. The two extreme cases postulated for the structure of silica are based upon:

- a network of randomly oriented crystallites
- a continuous random network of fully bonded molecules

Both these models can be shown to be flawed in that neither will account for the full set of physical properties measured for silica. The standard test of a model is the quality of agreement of theoretically calculated scattering profiles with those obtained experimentally by neutron or X-ray diffraction. Most current models can fit the short range atomic structure of silica, but many have trouble when trying to account for the medium range structural features with effects evident in the experimental data e.g. diffraction data and vibrational spectra.

1.2 Models

Many structural models for vitreous silica have been proposed over the years, the most influential being based upon the continuous random network theory of Zachariasen [1], examples being given in [2, 3, 4, 5, 6, 7, 8]. Models based upon microparacrystal structure within the glass have also been suggested by various authors as well e.g. [9, 10, 11, 12]. Both structural models have their champions and experimental evidence can be found in disagreement with either theoretical basis.

The problems which arise stem principally from the difficulty in generating models that produce medium range structure which agrees with experimental data. The difficulties arise in that the diffraction experiments from amorphous materials produce results which are hard to interpret beyond short range atomic correlation effects. This has lead to a large number of theoretical models for medium range structure including molecular rings, intersticial voids and other structures [13].

A difficult feature to interpret in the diffraction pattern obtained from a covalent amorphous solid is the first sharp diffraction peak which appears in the range of 1-2Å^{-1}. This feature is thought to be characteristic of medium range order, as on Fourier transformation to real-space its presence would be most visible on this length scale. This peak has unusual properties as a function of temperature and pressure which have lead to uncertainties in the interpretation of its significance [14].

Throughout model construction it is important to remember that consistency with bulk material properties has to be maintained, notably bulk density. Early controversy between the two basic theories for glass structure included arguments based upon crystallization properties, and when constructing models for vitreous silica, this is yet another feature which should be considered.

1.2.1 Random Network Models

These models, as previously stated, are based upon the basic principles suggested by Zachariasen [1]; early work on vitreous silica, interpreted using the random network theory, was performed by Warren [2]. The basis for a continuous random network or CRN structure is the idea that an infinite network lacking periodicity and symmetry can be constructed by the linking together of molecular polyhedra, sharing corners such that an extended three dimensional network may be formed.

The form of connectivity of the molecular polyhedra is an important feature of model construction as it has great influence over the medium range order that develops in the model. The short range order remains mostly unaffected as the molecular unit is fundamentally the same. The joining together of molecules to form a random network involves the inclusion of a distribution of bond angles between units, a necessary factor if symmetry is not to be introduced e.g. figure 1 [15].

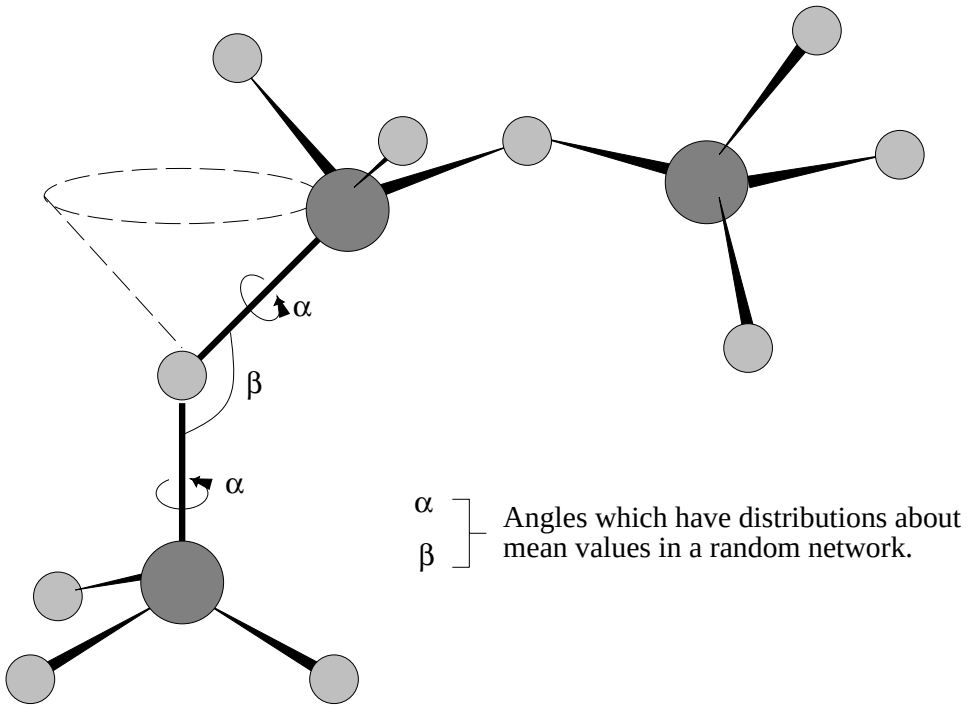

Figure 1: Example of variable bond angles between tetrahedral units.

The classic random network model for vitreous silica is the model constructed by Bell and Dean [4], this model being of ball and stick construction, using a tetrahedral base unit i.e. SiO_4 and corner sharing to construct a three dimensional network. This network was constructed having a mean $Si-O-Si$ bond angle of 153°. Analysis of this model showed that too much strain energy was present in its structure for it to be a true representation of silica, although it has shown the viability of the construction

technique.

Further work on the Bell and Dean model was carried out by Gaskell and Tarrant [6], who relaxed the model using a Keating potential force field. They found that the relaxed model possessed too little strain energy, showing that the true structure of silica must be of a slightly modified form if the physical properties of the material are to be adequately described.

Analysis of network structures often involves the study of ring structures which may be present, i.e. the size of loops present within the material, this giving an indication of the strain energy in the structure. Work on the computer simulation of random network models has progressed apace. These techniques have the advantage of being able to produce models with much greater efficiency than any manual technique. Work by Gladden [8] has produced good fits to much of the experimental data, the best model being that using a minimum ring size of five units and an average $Si - O - Si$ bond angle of 150°.

Many other papers have been produced on the random network theory, applied to a multitude of different amorphous solids, making it a very well supported theory. This proliferation of work on CRN models can partly be attributed to the flexibility in structural constraints which allows many different networks to be constructed, this being a great advantage over more rigid structural models which can preclude the inclusion of important properties. It must however be noted that just because a model is flexible, it still may not satisfy all the criteria needed for characterisation of a material.

1.2.2 The Crystallite Models

The crystallite model for vitreous silica has existed for many years [9], but work on the CRN model tended to gain the most interest. Recently, support for a paracrystallite model has arisen to help explain some of the anomalies present in interpreting the results of some experiments in terms of the random network model.

Crystalline silica exists in many forms [16], notably quartz, tridymite, cristobalite, coesite and keatite. The Paracrystalline models for vitreous silica seem to favour a base cristobalite structure for the small crystallites [10, 11].

The motivation for work on possible crystalline structures for vitreous silica is firstly the discrepancies between the vibrational spectra calculated for CRN models and experimental values and secondly the idea that the glassy state is determined by factors other than topology i.e. the ability of oxygen to form double bonds with only a small cost in enthalpy. This model, for a granular structure for vitreous silica, comprises of small β-cristobalite paracrystallites, of approximately 66Å in size. These crystallites are thought not to coalesce because their surfaces are saturated with $Si = O$ double bonds.

A critique of this model is given by Galeener and Wright [17], arguing that the paracrystallite model does not agree with neutron diffraction or Raman spectroscopic data when properly interpreted.

A more unusual crystallite model has been suggested by Hosemann et al. [12]. This model is based upon tetrahedral units, these units being twisted vice versa against each other through an angle of 22° along one of the cell axes. The micro paracrystallites are of the order of 12.5Å in size and the model leads to $O - Si - O$ angles of 106° and 117° and $Si - O - Si$ angles in the range of 141° to 149°. The model fits the experimental data of Mozzi and Warren [5] to *'within the thickness of*

a drawn line'; further comparisons with other sets of data are necessary, for example calculations of the structure's vibrational properties that could be compared with Infra Red spectroscopy results, before it can truly be accepted as a viable model.

1.3 Doped Silicate Glass

Silicate networks incorporating varying quantities and types of dopant atoms are increasingly finding uses in modern optical systems. This has lead to a great deal of interest in the structural environment of the sites occupied by these dopants, typically metals. The physical/optical properties of these glasses are sensitive to the environment into which the dopant atoms are placed but as yet no definitive models have been constructed.

Of particular interest to the optics community are systems doped with rare earth atoms since, due to the complex electronic structure of these atoms, many possibilities exist for exploitation of the wide range of energy states available, for example in the construction of devices such as lasers.

Since it is the dopant atoms incorporated into the glass network that provide the novel properties, a chemically specific study of the sites occupied by such atoms is crucial if any understanding of their properties is to be gained. It is the short range order about the dopant atom site which will have most direct effect on the electronic states available, although the effect of the dopant inclusion upon the longer range structure becomes more important as concentrations increase.

A suggested model for doped glasses is the modified random network model of Greaves [18], (see figure 2), in which the structure of doped silicate glasses is suggested to consist of regions of network former i.e. silica, and internetwork regions of modifier atoms. These two types of structure forming interlacing regions within the overall

system. The extent of this kind of structure will be dependent upon the quantities of dopant atoms incorporated into the silica basis. This model was developed from Extended X-ray Absorption Fine Structure (EXAFS) spectroscopy studies of doped glasses, a chemically specific technique useful for extracting short range structural information about a selected atom type within a sample.

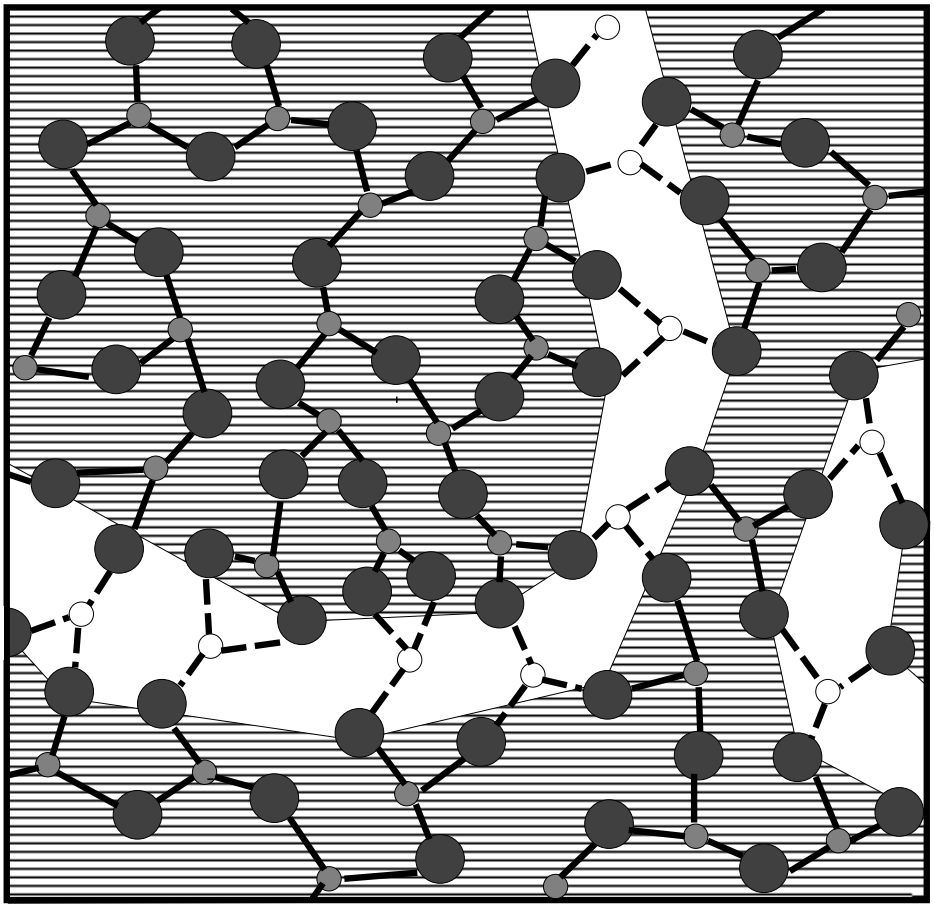

Figure 2: 2-Dimensional example of a Modified Random Network, showing the covalently bonded network forming regions and the ionically bonded modifier atoms residing in percolation channels running through the network.

Dopant atoms are often thought to find positions in the overall network, modifying the regions around themselves to satisfy their bonding requirements, but making no

longer range distortions. If this is the case, atom specific techniques, for example EXAFS spectroscopy, can elucidate the majority of the structural information.

1.4 Phosphate Glasses

The structural study of phosphate glass systems (based on P_2O_5) is very similar to silicate network studies, in this case CRN models are based upon PO_4 tetrahedra. The classic text on phosphorus and its compounds written by J.Van Wazer [19] and more recently a review article by Martin [20] present the ideas upon which structural models for phosphate glasses have been established.

Due to the valency of phosphorus one of the bonds is a double bond i.e. $P = O$ whilst the other three are single, producing what are termed *bridging* oxygen atoms which are free to form a second bond with, for example, a second neighbouring phosphorus atom i.e. these bridging oxygen atoms are the main network forming atoms.

In phosphate glasses doped with metal cations such as the rare earths, three main network building units can be considered, these being the *branching*,*middle* and *end* units, PO_4, PO_4^- and PO_4^{2-} respectively. It is envisaged that each negative charge is *soaked up* by the metal cations and that the oxygen atoms not contributing to the charge on the unit are involved in P-O-P bridging links.

Examples of experimental studies of phosphate glass systems are numerous, e.g. [21, 22, 23, 24].

CRN models are the usual models used for describing phosphate glasses, lending themselves quite well to the description of systems incorporating dopant atoms. The structure of phosphate glasses is highly sensitive to their manufacturing process, since they are particularly prone to network incorporation of water and evaporation losses incurred on heating the initial melt of starting compounds. It is therefore necessary

to note carefully the conditions under which phosphate glasses have been made if useful studies are to be made.

Phosphate glass systems doped with metal cations have attracted much attention, and glass networks incorporating a wide spectrum of dopant atom species and concentrations have been produced. Many structural units can be created in phosphate glass systems of which ultraphohsphates, metaphosphates and pyrophosphates are three examples. Basic definitions being (figure 3) [24]:

- *Ultraphosphate* Where the glass is predominantly P_2O_5, i.e. the dopant metal cations are present in relatively small quantities.

- *Metaphosphate* Glasses where the phosphorus to oxygen ratio is $\frac{1}{3}$, for example when the stoichiometric formula is $M(PO_3)$ where M is a monovalent metal cation such as silver, or $R(PO_3)_3$, where R is a trivalent metal cation such as a rare earth ion.

- *Pyrophosphate* The presence of dopant metal cations in quantities such that PO_4 dimers are effectively embedded in a sea of metal cations.

Theoretical modelling of the various possible structures and their effects on bonding and electronic states have recently been performed [25].

EXAFS studies of phosphate glasses have lead to the modified random network structure being proposed for doped phosphate glasses, key work being performed on lead-iron-phosphate glasses by Greaves et al. [26].

Doped phosphate glasses of metaphosphate composition are thought to consist of chains of PO_4 tetrahedra between which are the sites occupied by the dopant atoms. The stoichiometry of the metaphosphate composition lends itself to structures based entirely upon *middle* units, such as long chains and rings.

Systems with lower concentrations of dopants can be considered to be modifications of the basic pure P_2O_5 network moving towards the metaphosphate composition as the number of metal cations are increased. The metaphosphate composition is thought to be particularly stable, especially for glass formation using rare earth dopants.

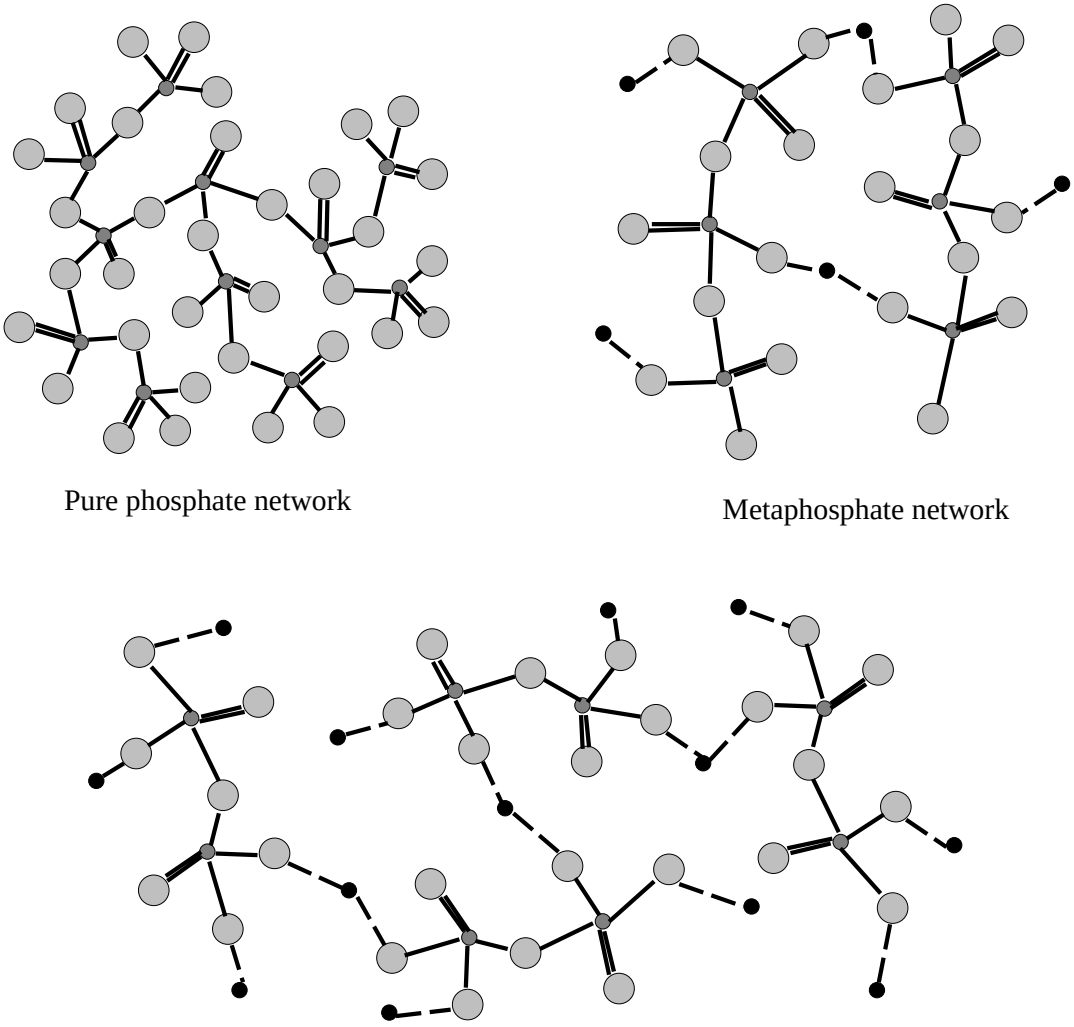

Figure 3: Schematic of example phosphate glass structures

Of the many probes used to study the structure of phosphate glasses, one of the most significant has been Raman spectroscopy [27, 28]. This technique offering an indirect measure of the structure, based on calculations of the vibrational modes relating to the units of composition of the glass, for example $P-O-P$ stretching modes which give a peak in the spectra at approximately 700cm^{-1}. It is studies such as these that have led to the idea of mataphosphate glasses being formed from chains of PO_4 units.

1.5 Rare Earths as Glass Dopants

A useful review of the Rare Earths as glass dopants with applications to optical properties has been written by Urquhart [29]. He presents a general overview of the Rare Earths and the properties that their inclusion in a glass matrix can produce.

The Rare Earths or Lanthanides occupy the section of the periodic table corresponding to the range in atomic numbers from 57 to 71. All these elements have the same outer electronic structure, namely $5s^2 5p^6 6s^2$ and core electronic structure identical to xenon, table 1. The optical characteristics of these elements are dependent upon the number of electrons that are present in the $4f$ shell i.e. lanthanum has has none whilst lutetium has fourteen. The optical absorption and emission properties arise from electron transitions within this shell.

Rare Earths usually ionize to give di/trivalent ions for example Nd^{2+} or Nd^{3+}, the electron loss typically being the two $6s$ electrons and one of the $4f$ electrons. The main significance of this being that the $5s$ and $5p$ shells remain intact thus partially shielding the $4f$ orbital.

When elements are added to a glass matrix as a dopant, a change in their electronic energy level structure will be induced. This modification has direct effects upon the

Lanthanide Element	Electronic Configuration Xenon [Xe] $2s^2 2p^6 3s^2 3p^6 3d^{10} 4s^2 4p^6 4d^{10} 5s^2 5p^6$
Lanthanum	[Xe] $6s^2 5d$
Cerium	[Xe] $6s^2 4f 5d$
Praseodymium	[Xe] $6s^2 4f^3$
Neodymium	[Xe] $6s^2 4f^4$
Promethium	[Xe] $6s^2 4f^5$
Samarium	[Xe] $6s^2 4f^6$
Europium	[Xe] $6s^2 4f^7$
Gadolinium	[Xe] $6s^2 4f^7 5d$
Terbium	[Xe] $6s^2 4f^9$
Dysprosium	[Xe] $6s^2 4f^{10}$
Holmium	[Xe] $6s^2 4f^{11}$
Erbium	[Xe] $6s^2 4f^{12}$
Thulium	[Xe] $6s^2 4f^{13}$
Ytterbium	[Xe] $6s^2 4f^{14}$
Lutetium	[Xe] $6s^2 4f^{14} 5d$

Table 1: Electronic Configuration of The Rare Earths.

dopant's optical properties:

1. Spectral substructure will probably become evident due to Stark splitting i.e. any degeneracies in the energy level structure will be removed due to the influence of the inter-atomic electric fields (i.e. chemical bonds). It should be noted that in an amorphous matrix such as silicate glass, the fields will have a non-uniform distribution and spatial variations throughout the bulk of the sample can occur.

2. Spectral broadening of the energy levels will be induced, the two main contributing factors being:

   - Phonon broadening.
   - Electronic perturbation broadening - a further result of the Stark effect in an amorphous material.

Phonon broadening is due to the fact that electron transitions between energy levels often include the creation of a phonon along with the photon. The energy of the phonon being dependent upon the ambient temperature, there being a distribution of such energies for any particular temperature. The spread in phonon energies causes a spread in the energy of the emitted photons due to conservation of energy within the system. This kind of spectral broadening is termed homogeneous as it effects the entire system equally.

The spectral broadening induced by the perturbations in the inter atomic electric field due to random atomic arrangement, leads to an additional, but in this case temperature independent broadening of the spectral lines.

Hence, the Rare Earth elements have a distinct advantage when used as dopant atoms to modify the optical properties of a glass. The partial shielding offered by the complete $5s$ and $5p$ shells to the optically active $4f$ level reduces the effect that inter atomic electric fields will have on the energy level structure of the dopants. This results in a reduction in the spectral broadening, an important characteristic when trying to construct devices such as glass host lasers.

The doping levels used when manufacturing novel optical glasses are critical to the performance of the envisaged devices. The efficiency of devices such as fibre lasers and amplifiers are dependent upon effects such as *concentration quenching*, an effect that occurs more prevalently in systems with higher dopant concentrations. This is essentially a problem of cross-relaxation of the excited state energy levels, induced by the close proximity of the dopant atoms to each other. This concentration quenching reduces the probability of achieving population inversion. Also, if the dopant concentration is too high, crystallization within the glass matrix can occur, dramatically increasing optical losses within the material.

Where the glasses are of interest due to their magnetic properties, having low dopant concentrations is not so critical a limiting factor, the shielded $4f$ orbital again being a major contributor to the unusual properties of the system.

At present doped glasses can broadly speaking be separated into two classes: those of optical significance in communications technology, and those of interest due to their magnetic properties. These two classes tend to divide very well between silicate and phosphate glass host materials for optical and magnetic properties respectively primarily due to the generally higher dopant level concentrations required for magnetic properties to be evident; silicate glasses tend to be unfavourable to support high rare earth ion concentrations without phase separation effects. Silicate glasses generally have greater resistance to many environmental factors that make phosphate glasses currently non-viable for use in the field, e.g. water contamination, which is a severe problem for phosphate glass systems (although rare earth metaphosphates have been found to be highly resistant to water absorption, compared to other phosphate glass systems). Silicate systems are also much easier to produce with low dopant atom content, with techniques such as chemical vapour deposition being developed for producing high quality optical glass suitable for optical fibre production. A more accurate description would be that silicate glasses, doped with rare earth elements are restricted to low dopant concentrations if clustering of the rare earth ions is to be prevented [30]. An upper limit of about 1 wt.% is achievable in silicate systems before clustering and phase separation occurs between the rare earth dopants and the bulk silica network. It is possible to reduce the propensity for rare earth ions to cluster within silica glass, if Al_2O_3 is used as a codopant; the incorporated aluminium ions have a tendency to aid in the dispersion of the rare earth ions throughout the glass. Other parameters that favour silicate systems for the production of fibre optic

devices generally arise from compatibility criteria; modern communications systems are generally based around undoped silica fibre as the primary optical link, hence simplifying the splicing of new devices into networks i.e. no material compatibility problems.

Phosphate glasses are still generally produced from a melt of pure P_2O_5 and then poured into moulds, any dopants being added as pure compounds to the initial melt chemicals.

Chapter 2

Optical Fibres and their Manufacture

2.1 Introduction

In the field of modern electronics, the use of light to carry signals for purposes of control and information transfer is becoming prevalent, giving rise to the specialist study of the new domain of optoelectronics. Optical devices have many advantages over conventional electronic systems such as allowing the transfer of signals through regions subject to electromagnetic "noise" without corruption, by using glass fibre to carry light waves rather than copper wires carrying electric current. Another advantage often associated with optical devices is their potential operational speed, which can far outstrip electron based systems. A good introductory text to optical fibre technology has been written by Kao [31] which provides a basic grounding in the general state of the technology.

Optical fibres are already widely used in telecommunication systems due to the

large amounts of information that it is possible to carry on the fibre and the ability to transmit many individual signals through the same fibre simultaneously without interference. One of the major problems in telecommunications is signal amplification, since the signal strength must be boosted periodically if it is to travel a long distance, the losses being due to imperfections in the optical transmission medium. Typically, when manufacturing optical fibre the purity of the glass must be such that attenuation losses are less than 0.5 dB per kilometre in the optical "window" chosen for transmission examples being 0.38dB/km at 1300nm and 0.21dB/km at 1550nm. The method of amplification in current use involves converting the optical signal into an electrical signal, amplifying this by conventional means then reconverting to an optical signal on exit from the booster station spliced into the line.

Recent investigations into the properties of glass fibres doped with small amounts of impurity atoms have shown that these systems are capable of selective absorption, signal amplification or even lasing if certain conditions are met. The possibilities for exploitation opened by these novel properties are endless, e.g. it is now possible to build a completely optical communication system using optical amplifiers rather than electronic amplifiers, thus reducing costs and system maintenance requirements.

2.2 Optical Fibres: Their Manufacture

Fibres to be used in optoelectronic devices and systems must be manufactured to very stringent operational parameters. Fibre used for telecommunications purposes is required to have very low losses (0.5dB/km) , since it is typically desired to have lengths of fibre at least 80km in length before signal amplification is necessary. Fibre used for optoelectronic devices has different criteria notably reliability, stability and low loss at signal wavelengths (10dB/km); optoelectronic devices tend to use much

shorter lengths of fibre, for example a few centimetres for fibre lasers and a few tens of metres for fibre amplifiers, hence loss characteristics are less relevant. These requirements led to the development of several manufacturing techniques which take advantage of the physical properties of silicate glasses. It is quite feasible to create optical fibres from other materials, but those based upon SiO_2 are currently the most widely used. Optical fibre should be easy to handle, have high tensile strength, reasonable flexibility and be of near perfect geometry over continuous lengths of several kilometers. Manufacturing methods which are in use are:

1. Molten glass allowed to flow from a nozzle in the bottom of a crucible.
2. Molten glass drawn upwards from a pool.
3. Drawing the fibre from a softened glass tube.
4. Chemical Vapour Deposition CVD.
   (a) Modified Chemical Vapour Deposition MCVD.
   (b) Outside Vapour Deposition.
   (c) Vapour-Axial-Deposition.

Methods one to three have the disadvantage that they have glass as raw material upon which the fibre manufacturing process is performed. This means that a highly pure source of glass must be obtained and all the materials which will come into contact with the molten glass must be chosen so as not to contaminate the developing fibre. The last three methods make use of easily purified source chemicals combining them *in situ* to produce the glass making up the optical fibre and these are the favoured methods used in the production of telecommunications fibre.

2.2.1 Molten Glass Methods

Fibre manufacture from molten glass is usually performed using one of the methods shown in Figure 4 i.e. the double crucible technique and the creation of a clad fibre from a twin layer system of pooled molten glass. When fibre is made using this

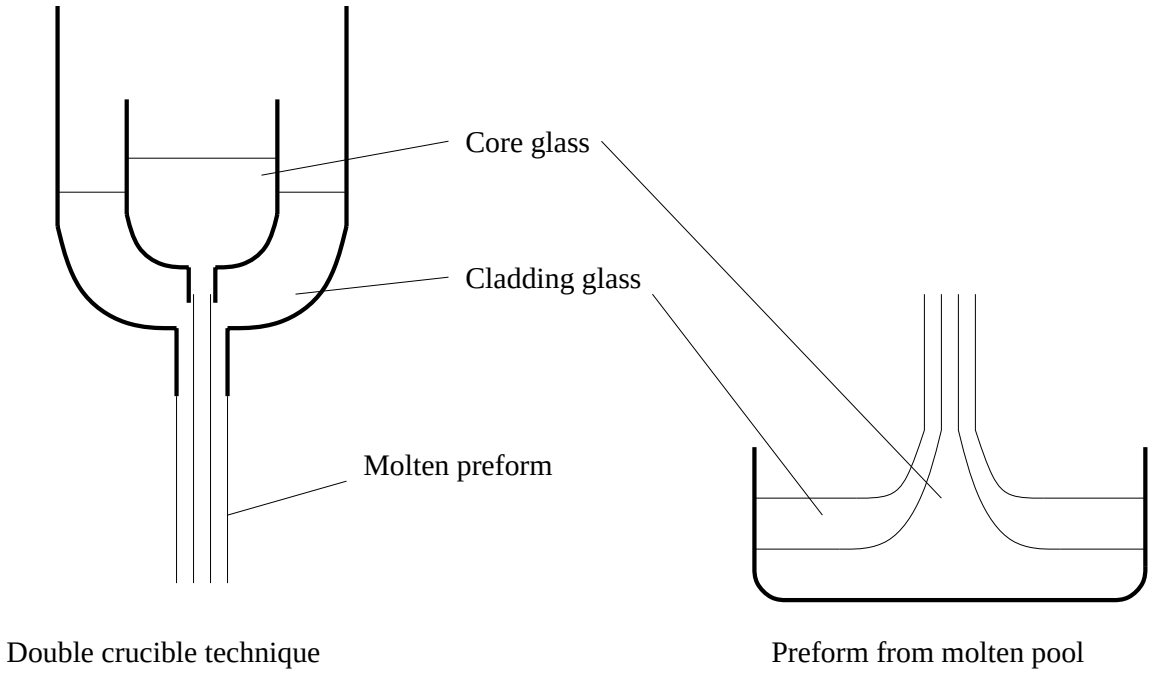

Figure 4: Molten glass preform preparation techniques

kind of system, care must be taken to avoid using materials which could release contaminants into the glass at the high temperatures involved e.g. 800^oC. Typically radio frequency induction heating techniques are used on the system since the energy coupling is directly to the glass.

Fibres manufactured using these techniques have an almost perfect core-cladding interface since the glasses making up these regions come into contact in the liquid state. This produces a grading in the refractive index across the interface between the two regions.

2.2.2 Drawing a heat softened, glass rod/tube system

This method entails the production of fibre by drawing a rod-tube system i.e. the glass to constitute the core is produced as a rod which is placed inside a tube of cladding glass. The tube is then collapsed onto the rod as the preform is heated and drawn out into a fibre. Both the collapse and draw processes are performed simultaneously so as to avoid cracking at the interface due to stress, induced by slightly different expansion coefficients between the rod and tube glass. A disadvantage of this technique is that any imperfections in the core cladding interface are preserved in the preform and fibre reducing the quality of the end product.

2.2.3 Chemical Vapour Deposition

This method is really a glass production technique which can be adapted to allow the production of low loss fibre in a manner allowing *in situ* purification of the end product. The method allows the production of glasses with high silica content since the temperatures involved are between 1500^oC and 2000^oC (above crucible operating temperatures). As a technique, CVD is useful in fibre production due to it's versatility, allowing simple changes in glass recipes, a useful trait for research and development processes.

The production of fibre by variants on this method is a four stage process, each stage having its own characteristic temperature of operation, they are:

1. Glass formation at approximately 800^oC.

2. Fusing the particles of SiO_2 produced, at 1500^oC.

3. Collapsing the fused "boule" at 1900^oC.

4. Drawing the glass at 2100^oC.

A schematic of a plasma torch method for producing glass on a rotating pedestal is shown in Figure 5 [32]:

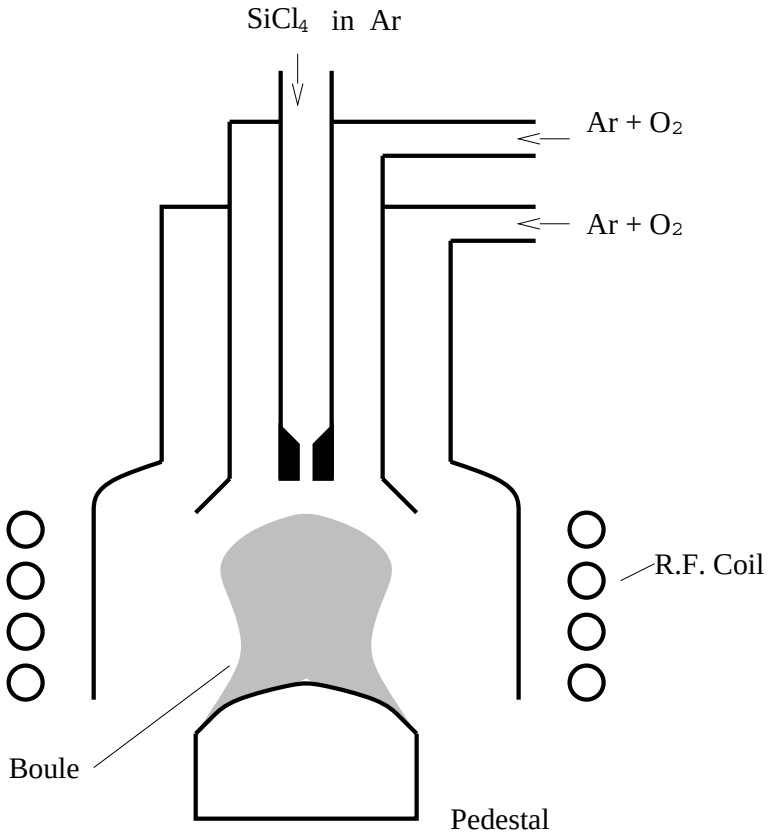

Figure 5: C.V.D. Torch

$$SiCl_4 + O_2 \longrightarrow SiO_2 + 2Cl_2$$

When producing low loss fibre using one of the adaptations to the CVD technique, the *in situ* purification arises due to the vapour pressure differences between the glass making materials and contaminants. (The vapour pressures for $SiCl_4$ and $GeCl_4$ are higher than the main contaminants at temperatures below approximately 200^oC

therefore, if they are extracted as a vapour from the liquid state e.g. by bubbling through oxygen gas, the contaminants should not be taken up in any great quantity).

Modified Chemical Vapour Deposition

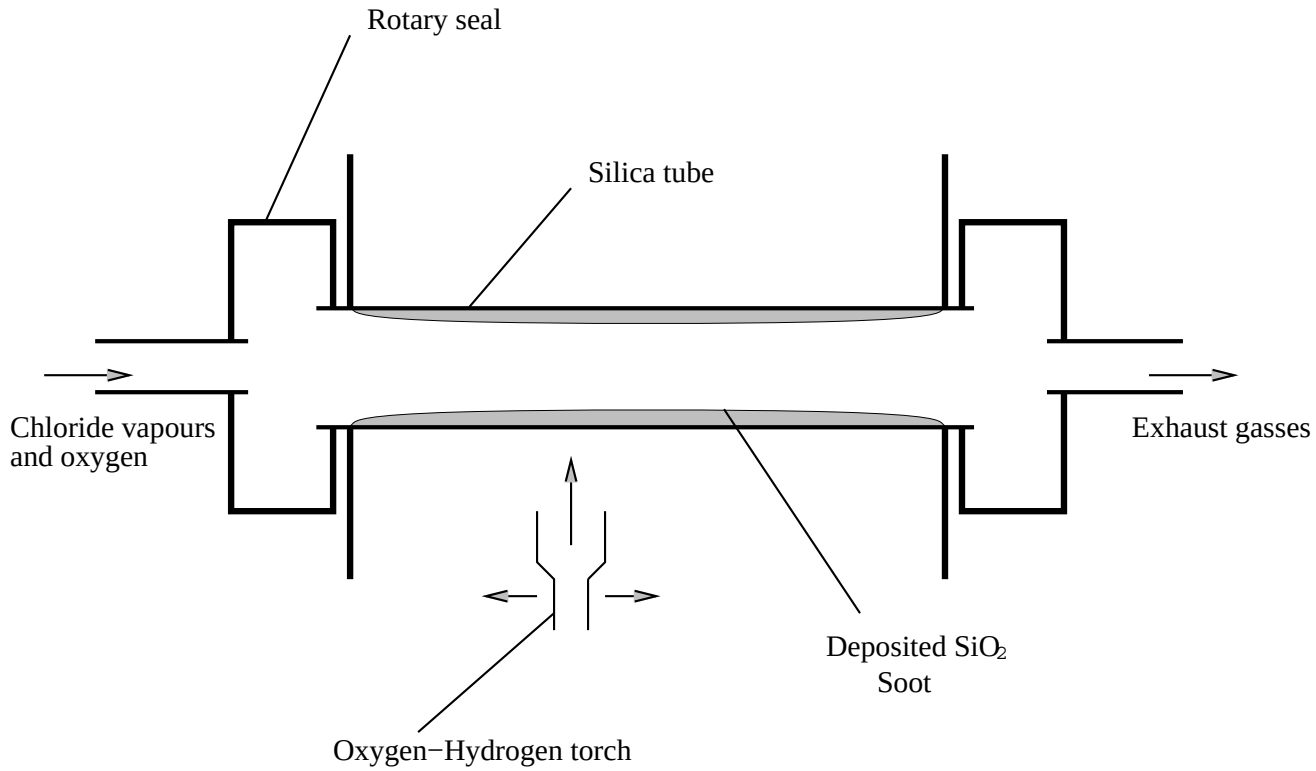

Figure 6: Modified Chemical Vapour Deposition, MCVD

The high purity glass making chemicals such as $SiCl_4$, $POCl_3$ etc. are stored in glass or stainless steel vessels. Oxygen gas is bubbled through each liquid halide separately and the vapours are carried into the reaction chamber (the silica tube). Mass flow controllers are used to control the proportions of vapours added to the reaction mixture and a pure oxygen line is added to provide oxidising conditions and control the total flow rate. The temperature of the storage vessels is kept at a constant value (e.g. 20^oC) so that known quantities of vapour are given off, care is

taken to avoid condensation in the pipework. CVD techniques generally make use of high purity chemicals with low transition metal (Fe, Cu etc.) ion content as only a little purification occurs due to chemical feed being vapour pressure dependent

In the above configuration the reaction point is determined by the position of the oxy-hydrogen flame and small particles of glass are created in this region, slowly coating the inside of the rotating silica tube with a glassy layer; cladding layers are deposited first, followed by the core layers. Sometimes helium gas is added to the flow gases to improve heat conductivity ensuring thermal homogeneity across the tubes diameter.

Alternative methods for heating the reactant gases revolve around the use of r.f. induction heating similar to that used in the CVD process shown earlier. By tracking the heating mechanism along the length of the silica tube many times, thin layers of the glassy material are built up and hence it is very easy to adjust the proportions of the constituents for each deposited layer to control the optical properties of the core and cladding regions of the fibre. Once the layers have been deposited, the silica tube is collapsed to form the "preform" for the optical fibre. This preform is then drawn to give the optical fibre.

Outside Vapour Deposition

This technique makes use of an oxyhydrogen torch that allows the glass constituent vapours to be fed into the flame through a nozzle concentric to the fuel gases. The soot particles produced in the flame are deposited onto a rotating mandrel and the torch tracked back and forth to build up layers of glass. The outside processes have an advantage over MCVD in that they can make glasses with a lower melting point since they do not require an elevated temperature to collapse a silica substrate tube.

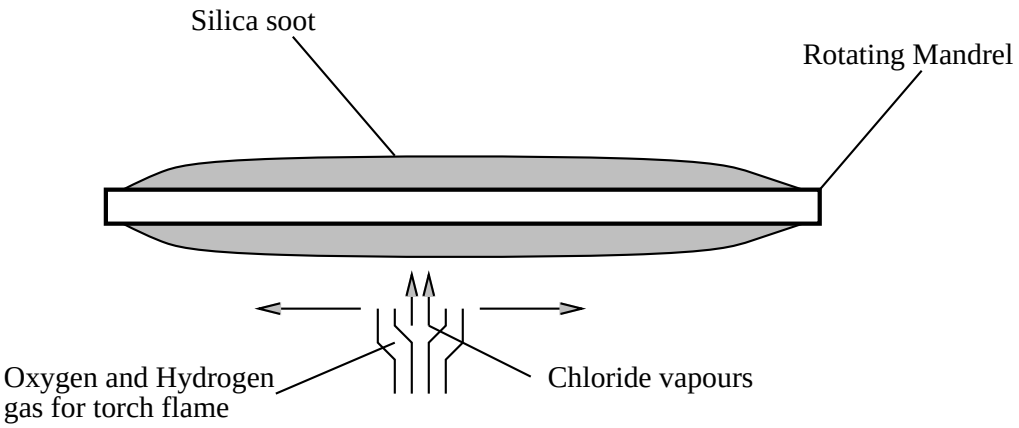

Figure 7: Outside Vapour Deposition, OVD

Once a soot preform has been created (its layer constitution controlled as in the MCVD process), the supporting start mandrel is withdrawn. The preform is then dried, sintered and collapsed into a preform rod in a controlled atmosphere furnace. The soot rod must be dried before sintering since it is highly porous and the glass formation process is hydrolytic. Often this is done by heating in Cl_2 to produce HCl as a waste gas.

One advantage offered by this method is its ability to be easily scaled up for production i.e. more deposition torches are easily added, care must be taken to ensure an even stress distribution as the soot is deposited on the mandrel, and care must also be taken to try and minimise this at the core cladding interface. Along with vapour axial deposition, this technique forms the main process by which modern optical fibre is produced.

Vapour Axial Deposition

The basic principles involved in this technique have been outlined in the for the OVD process. The main difference being the use of a vertical rotating seed rod which is

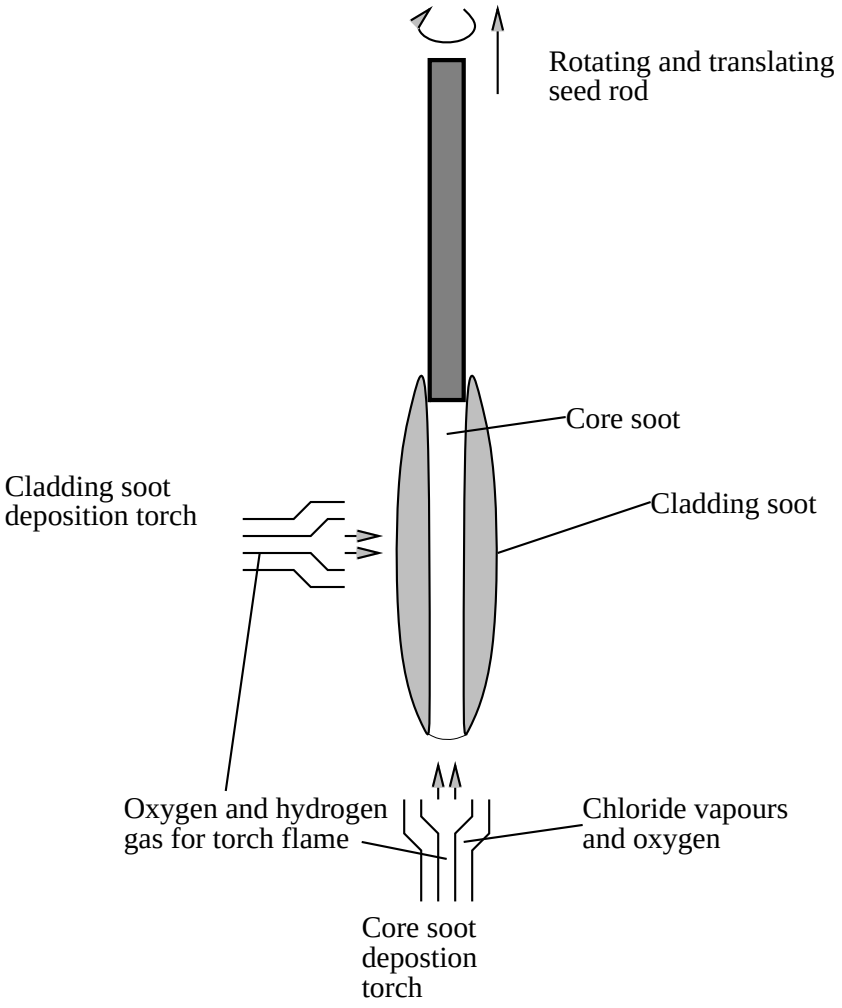

Figure 8: Vapour Axial Deposition, VAD

gradually drawn upwards instead of a horizontal support mandrel for the deposition of the soot boule, thus resulting in system which does not have the difficulties of removing a mandrel before drying and sintering. The method allows the creation of very large boules and is well suited to industry.

2.2.4 From Preform to Fibre

Once fibre preforms have been manufactured by one of the above methods, it is necessary to draw and coat them to produce useful optical fibre. The coating of the fibre is very important since the fibre must be protected against fracture caused by dust and other abrasive environmental dirt. Typically the coating materials are acrylate resins which must meet the criteria of :

- Abrasion resistance
- Flexibility
- Easy application and curing to the fibre
- Buffer for microbending effects

Fibre drawing involves heating the fibre to approximately 2000^oC in some kind of furnace (either induction or direct heating), feeding the preform into the furnace whilst pulling the fibre at a rate controlled by a feedback loop to maintain the drawn fibre dimensions (typically $125\pm1\mu$m). The fibre coating mechanism is placed after the furnace with some method of force cooling the fibre to a temperature at which coating can be undertaken. The entire drawing process must be monitored continuously as the fibre must be kept within very tight tolerance bands for concentricity and diameter and strength. A schematic of fibre drawing apparatus is shown in figure 9.

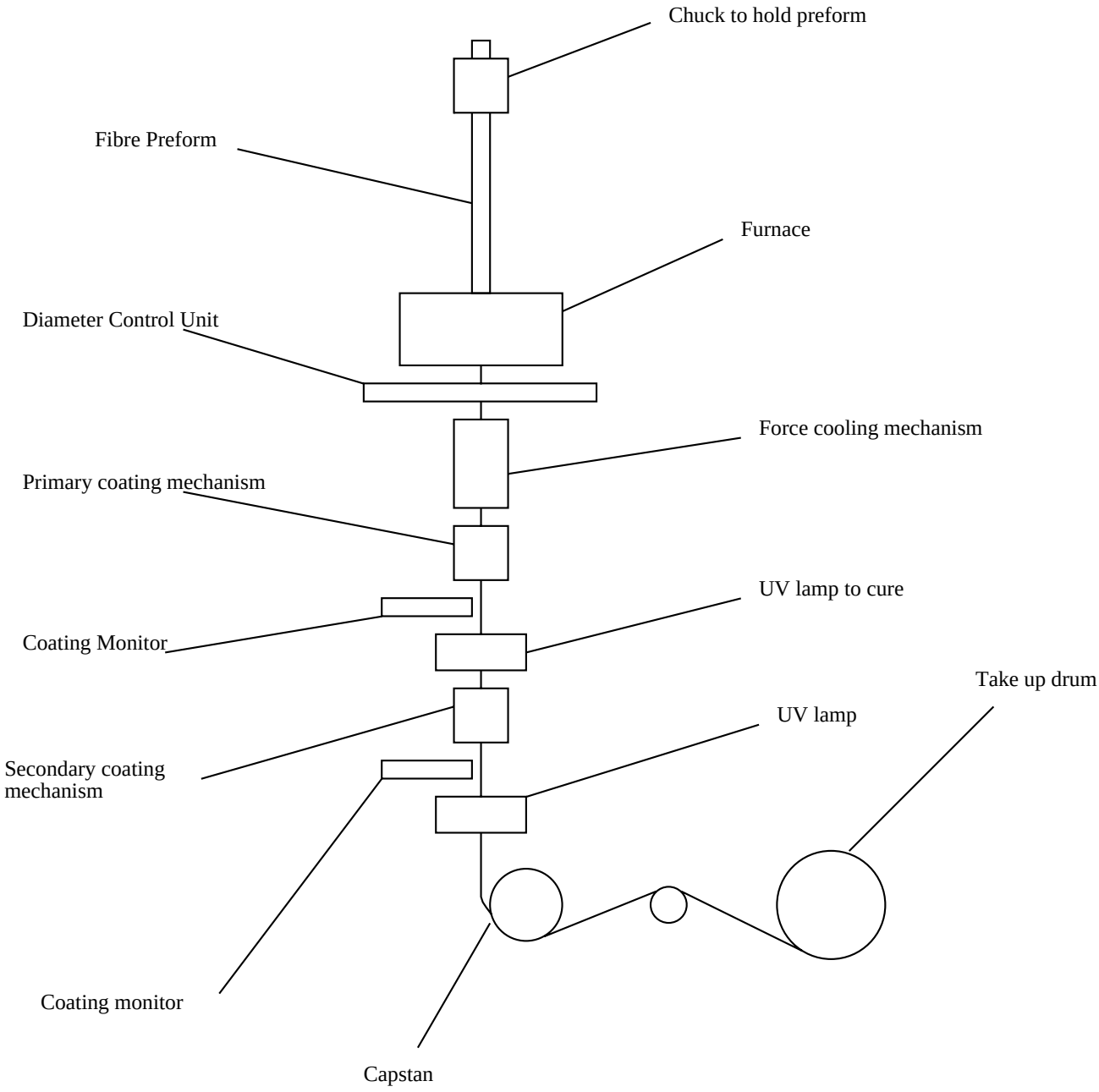

Figure 9: Schematic of fibre drawing mechanism

2.3 Doped Fibre, its Uses and Characteristics

In recent years interest has become focused upon a type of optical fibre which can display novel optical properties, opening fields of research in areas such as fibre lasers and amplifiers. These fibres are manufactured by incorporation of small quantities of dopant atoms in the core region, typical dopants being rare-earth elements e.g. neodymium, erbium, praseodymium, thulium etc..

Doped fibre is the essential component in the development of fibre lasers and amplifiers due to its ability to absorb energy from a pump light source, placing the dopant atoms in an excited state, then coupling this energy either into a signal carrying guided wave i.e. an amplifying action, or if suitably engineered, into stimulated emission of light at a characteristic wavelength i.e. laser action. There are many papers and references to doped fibre systems in the current literature, a good background review of optical fibre amplifiers is [33], but there are many more detailed papers on this topic to be found e.g. [34, 35, 36, 37].

There are many uses for fibre amplifiers and lasers due to the versatility of the systems and their relatively low cost. A good example of the benefits of a fibre amplifier system is illustrated in the field of long distance telecommunications, i.e. to carry a signal over long distances, periodic booster stations are required to overcome the intrinsic power losses that even a low loss optical fibre system experiences. As previously mentioned before the introduction of fibre amplifiers it was necessary to take the optical signal, convert to an electrical one which could then be conventionally amplified, then reconvert to an optical signal for further propagation, each stage introducing a set of engineering problems as well as possible data errors. The development of fibre amplifiers allowed the direct amplification of the optical signal in a package which offer:

- Bit rate transparent systems that can easily be upgraded
- High bit rates and multiwavelength operation
- Reasonable cost and high reliability

Very important factors in telecommunications where oceans, quite literally, have to be crossed [38].

The choice of dopant atom in the fibre influences the wavelength of operation of the device, due to the characteristic energy level distribution of the particular rare earth incorporated. Most interest has so far rested with the erbium doped fibre amplifier (EDFA) which operates in the 1.55 micron telecommunications spectral window, but investigation into the production of amplifiers operating at 1.33 microns is under way, possibly by the use of praseodymium as the dopant atom in a different glass matrix. (The reason being the possibility of dispersion free signal transmission at this wavelength.)

Other rare earth dopants, for example neodymium, have been incorporated into silicate glass fibres in relatively high concentrations for the production of temperature sensor devices [39, 40]. These many diverse applications of doped fibres, demonstrate the general importance of materials of this nature to developing technologies.

Complementary dopants which are incorporated into optical fibre are the elements germanium, aluminium and phosphorus which have properties complementary to the inclusion of the rare earth elements as well as allowing the control of the refractive index profile of the core, a very important fibre characteristic. These elements are included as glass formers i.e. GeO_2, Al_2O_3 and P_2O_5, in contrast to the rare earths which are network modifiers, incorporated into the silicate network as ions e.g. Er^{3+}. Germania generally being included in the core region of fibre to raise the core glass

refractive index, whilst alumina assists in allowing the incorporation of rare earth ions without clustering or phase separation in silicate systems.

Silica fibres doped with germanium in high concentrations have the property of photosensitivity [41], which can be exploited in many useful ways. Photosensitivity is when on irradiation by UV light (e.g.257.3nm), a core defect is created in the germanium atom, i.e. a free electron and a core hole, the free electron then moves under influence from the optical field and relocates into higher or lower energy, potential wells. This phenomenon, gives rise to a change in the UV absorption spectrum which in turn causes a change in the material's refractive index (Kramers-Kronig relations) of the order 10^{-4}.

One useful application of this property is the optical etching of Bragg gratings in the core region of a doped silica fibre, by side irradiation of the fibre with coherent UV light arranged to form an interference pattern along the core [42]. This fibre can then be used to filter out frequencies of light not passed by the grating. Other applications of photosensitivity could include optical storage of information as the material retains the variations in refractive index until the changes are wiped by re-exposure to a uniform irradiation of UV light.

2.4 The Manufacture of Doped Fibre

Doped optical fibre is usually made using one of the vapour deposition techniques outlined in the previous chapter, the most important of which being MCVD and VAD. Vapour deposition techniques lend themselves to the production of this type of fibre due to the porous nature of the deposited silica soot. The porous soot can be impregnated with dopant atoms by various methods, permanently capturing them on sintering and consolidation into the glassy state.

The procedures which have been pioneered for dopant introduction are based around three main methods, these being:

- Vapour Doping
- Aerosol Doping
- Solution Doping

Each of which allows the doping of fibres from rare earth chlorides which can be obtained in a very pure state, important if transmission losses are to be minimised. These chlorides tend to be awkward to work with since they are hygroscopic and have high melting points, solutions also have much lower vapour pressures than the main glass making constituents of $SiCl_4$ and $GeCl_4$ making it impractical to incorporate the dopant in the deposition vapour mixture produced by bubbling oxygen gas through the liquid chlorides.

2.4.1 Vapour Phase Doping

A technique to introduce dopant atoms into the fibre preform (ultimately the fibre) as a vapour was developed in the mid 1980's at Southampton University [43]. A simple outline of the technique which is based on MCVD follows.

A section near the feed end of the silica substrate tube is enlarged, the rare earth chloride is then introduced into this enlarged region and heated to its melting point. The whole tube is rotated in a glass working lathe, thus coating the inside of the enlarged region of the substrate tube with a layer of rare earth chloride.

The cladding layers are then deposited as usual for MCVD, once this has been done and the doped core is to be deposited, the region of the silica tube coated with the rare earth chloride is heated to a temperature above 1000^oC by a stationary

burner, this ensures a reasonable vapour pressure so as to provide enough dopant to be carried into the deposition zone along with the main core glass constituents. The tube is then collapsed to form the preform which can subsequently be drawn into a fibre.

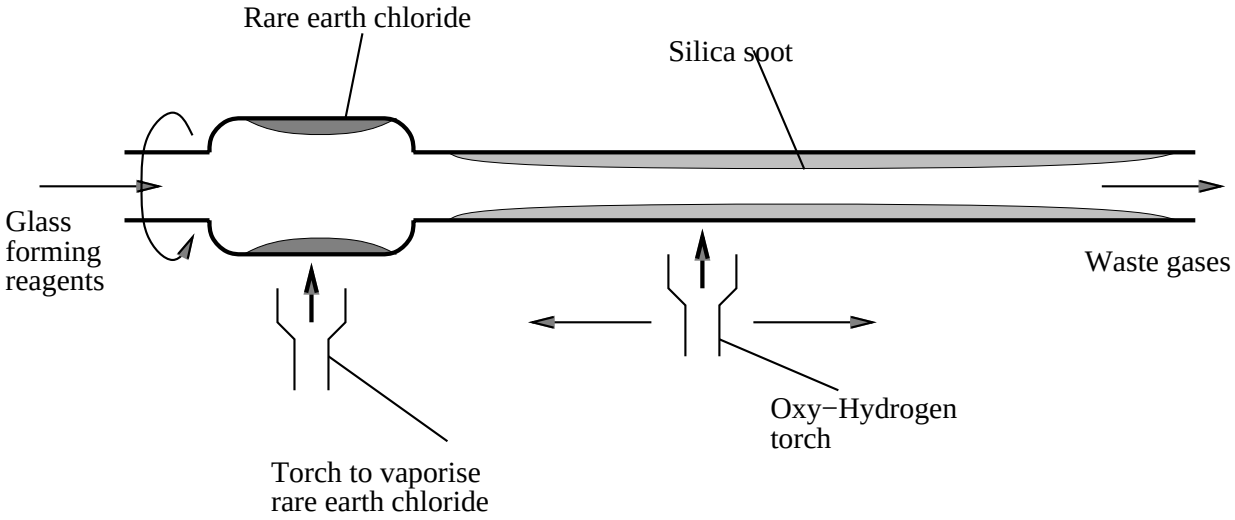

Figure 10: Vapour deposition of dopant atoms

2.4.2 Aerosol Doping

An aerosol technique for including dopants in preforms produced by MCVD and OVD/VAD was investigated by Morse et al. [44], in a search for a technique which would allow the controlled introduction of a dopant during deposition of the core layers. The technique is based around introducing an aerosol of nebulised particles produced from a solution of the dopant in a suitable solvent.

Problems which can occur with this technique are regions of microcrystallinity probably produced by the evaporation of the solvent as the dopant aerosol passes into the hot zone of the deposition tube, leaving crystalline rare earth compounds

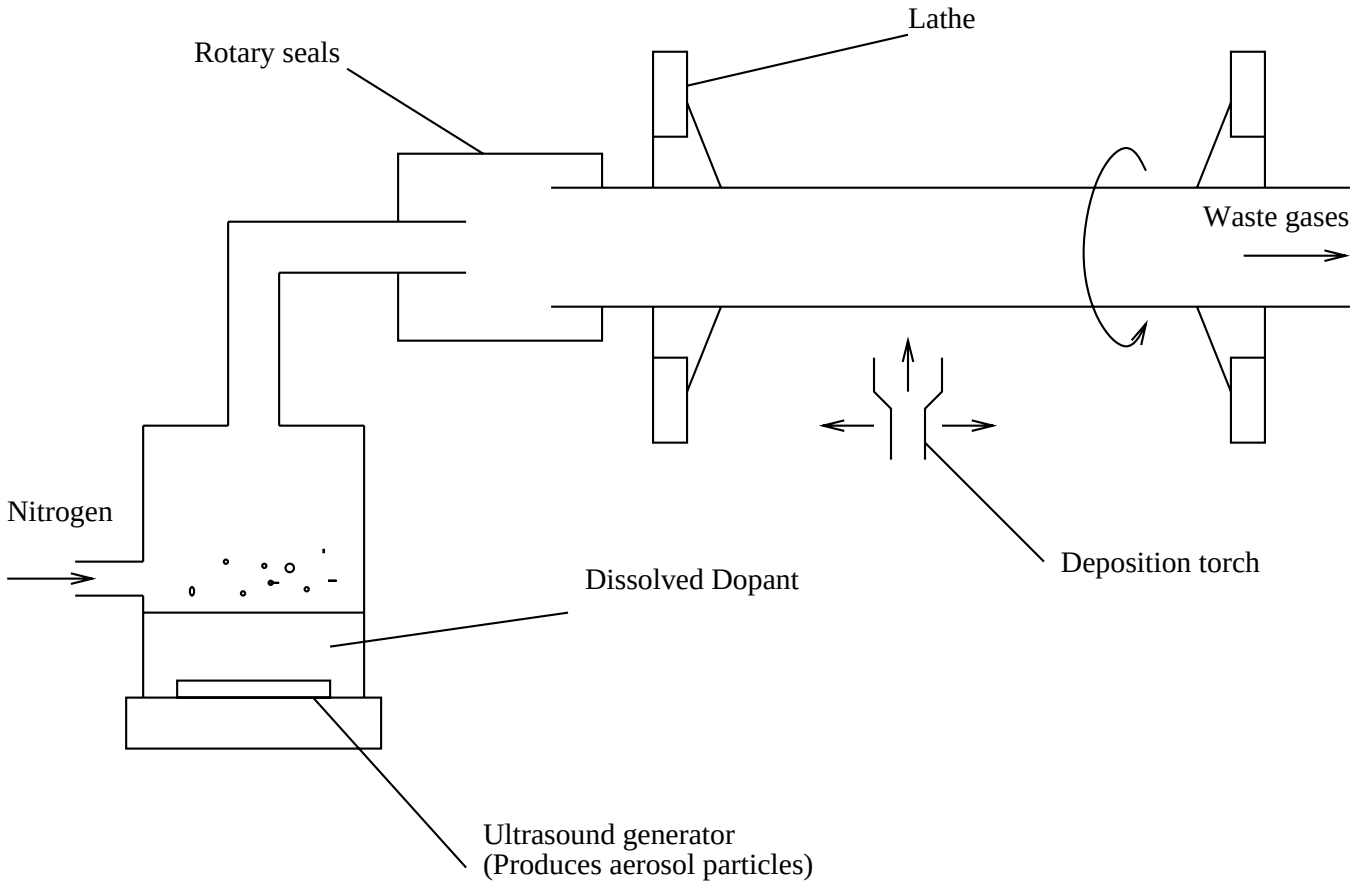

Figure 11: Aerosol delivery system for MCVD

contaminating the silica soot. Work with different solvents is hoped to improve on this situation.

More recently aerosol doping techniques have been applied to the production of rare earth doped silica waveguides, an example being given in [45].

2.4.3 Solution Doping

This is a technique which allows reasonably reproducible doping of optical fibre preforms. As a technique, it has the advantage of simplicity since it is based around the standard MCVD or OVD/VAD process. An outline of the process as presented by

Townsend et al. [46] is:

Manufacture a fibre preform as usual by MCVD, laying down and sintering the cladding layers within the silica substrate tube then at a lower temperature, so as to lay down an unsintered porous soot, deposit the core layers. The silica tube is then removed from the lathe and an aqueous solution of dopant is poured into the tube and left for one hour, after this the solution is removed and the tube is rinsed with acetone to remove excess water. The silica tube is replaced in the lathe and dried by heating at $600^{o}C$ in a stream of chlorine gas, then the preform is collapsed as usual.

Modifications to the process have improved the technique [47], notably the use of alcoholic solutions of the dopant to reduce water contamination and the avoidance of the acetone rinse which had the rather unfortunate side effect of washing out an unknown amount of the dopant.

The technique has been easily adapted to OVD and VAD since the dopant can be incorporated in the unsintered core boule by immersion in the alcoholic solution before further deposition of the cladding glass. Quantity of dopant incorporation can be influenced by control of the concentration of dopant in solution and by the pore size of the deposited core soot, a slower soot deposition temperature leading to larger pore sizes.

Chapter 3

Basic Theory of X-ray Diffraction

3.1 Introduction

The interaction of X-ray photons with matter is a fairly complex process which results in one of two occurrences; the absorption of the photon by one of a multitude of processes or its elastic/inelastic scattering. Interpretation of X-ray diffraction experiments is based on the analysis of the diffraction pattern produced by the elastically scattered X-rays deflected on passing through a sample, corrections being made for absorption and inelastic interactions. These diffraction patterns were historically collected using photographic film, but advances in technology have led to the use of electronic, energy discriminating detectors which can collect the data in a more convenient form. Development of superior methods of X-ray production has culminated in the advent of the synchrotron radiation source, offering a wavelength tunable, high flux beam of linearly polarized X-rays.

The development of the theory of X-ray diffraction can follow one of two lines, that of classical electrodynamics leading to an approximate final result or the more

rigorous quantum mechanical approach. In this text, the classical approach will be presented with reference to the quantum mechanical results when required, this is a justifiable method since the final results of the more rigorous treatment are very well approximated. The two main texts which shall be followed throughout this section are by Warren [48] and Huxley [49], although much useful information on general diffraction can be found in the review articles by Gingrich [50], Furukawa [51], Kruh [52] and Paalman and Pings [53].

3.2 Theory

3.2.1 Scattering from a single electron

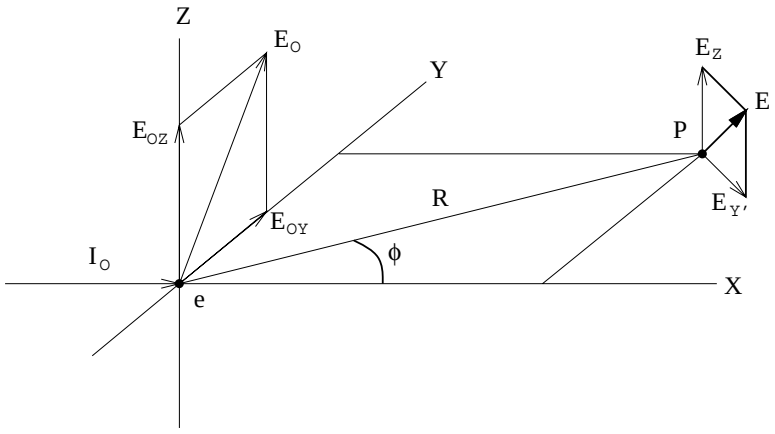

Figure 12: The scattering of an unpolarized beam of X-rays by a single free electron

First, considering the scattering from a single electron in the path of an unpolarized beam of X-rays, using cgs units for simplicity. This electron would experience the time varying electric field:

$$\mathcal{E} = \mathbf{E_o} \sin 2\pi\nu t \tag{1}$$

E_o is the amplitude of the wave, ν the frequency and t is time. A charged particle in an electric field experiences a force and hence an acceleration given by:

$$\mathcal{A} = \frac{e\mathcal{E}}{m} \tag{2}$$

e is the charge on the electron and m is its mass. Classical electrodynamic theory tells us that a charged particle experiencing continuous oscillatory acceleration in an electric field will radiate electromagnetic radiation of a frequency equal to that of the induced oscillation, i.e. the frequency of the wave in the incident beam. The electric field at a point P, produced by the radiation of the electron can be shown to be [48]:

$$\epsilon = \frac{eA\sin\alpha}{c^2R} \tag{3}$$

Where α is the angle between $\mathcal{A}$ and $\mathbf{R}$, the vector between the electron and the observation point P. Breaking the problem down by introducing the components of the various oscillatory motions i.e. E_{oy},E_{oz},$E_{y'}$ (see Figure 12) and E_z etc. It can then be shown that the electric field at P due to the acceleration of the electron is given by:

$$E_{y'} = \frac{e^2E_{oy}}{mc^2R}\cos\phi \tag{4}$$

$$E_z = \frac{e^2E_{oz}}{mc^2R} \tag{5}$$

Summing the two components to get the total resultant amplitude gives:

$$E^2 = E_z^2 + E_{y'}^2 = \frac{e^4}{m^2c^4R^2}\left(E_{oz}^2 + E_{oy}^2\cos^2\phi\right) \tag{6}$$

Averaging E_o over all orientations in the YZ-plane and noting that both axes are equivalent ends in the result that:

$$\langle E^2\rangle = \langle E_o^2\rangle\frac{e^4}{m^2c^4R^2}\left(\frac{1+\cos^2\phi}{2}\right) \tag{7}$$

Remembering that in cgs units, the conversion to intensity is given by:

$$I = \frac{c}{8\pi}\langle E^2 \rangle \tag{8}$$

The Thompson equation for the intensity of classical scattering from a free electron results:

$$I = I_o \frac{e^4}{m^2 c^4 R^2}\left(\frac{1+\cos^2\phi}{2}\right) \tag{9}$$

Where $\frac{1+\cos^2\phi}{2}$ is termed the polarization factor for an unpolarized incident beam.

3.2.2 Compton scattering

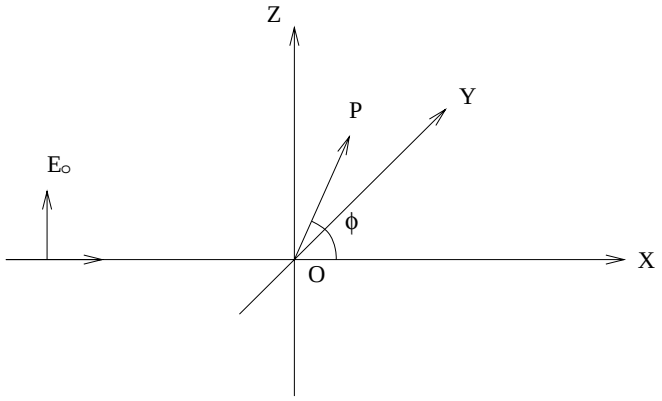

Figure 13: Polarized X-ray incident on a free electron

The wave mechanical treatment of X-ray diffraction shows that in reality electrons do not always scatter as predicted by the classical approach. This difference in result is due to the electron recoil in the collision which effectively takes energy from the scattered photon hence increasing its wavelength, i.e. the collision is not perfectly elastic. The nature of this interaction was calculated by Compton in 1926, a brief outline is as follows.

The equation for conservation of energy in the collision between the photon and the electron is:

$$h\nu = h\nu' + mc^2\left(\frac{1}{\sqrt{1-\beta^2}} - 1\right) \tag{10}$$

and the equations governing the conservation of momentum in the X and Z directions respectively, are:

$$\frac{h\nu}{c} = \frac{h\nu'}{c}\cos\phi + \frac{m\beta c}{\sqrt{1-\beta^2}}\cos\theta \tag{11}$$

$$\frac{h\nu}{c} = \frac{h\nu'}{c}\sin\phi + \frac{m\beta c}{\sqrt{1-\beta^2}}\sin\theta \tag{12}$$

The terminology being ν the incident photon frequency, ν' the scattered photon frequency, c the speed of light,m the mass of the electron, β the ratio of the electron recoil velocity to the speed of light, h is Planck's constant, θ is the angle between the electron recoil vector and the incident photon axis and ϕ the scattering angle for the photon as measured from the incident axis.

The solution of these three equations in terms of the scattered photon wavelength is:

$$\lambda' = \lambda + \frac{h}{mc}(1 - \cos\phi) \tag{13}$$

which demonstrates that the change in wavelength is independent of the incident energy of the photon.

3.2.3 Atomic scattering

The next step in the consideration of X-ray diffraction is the theory of scattering from electrons bound to atoms. This process is essentially quantum mechanical and is best described by assuming that the electrons are clouds of continuous charge density ρ about the atomic nucleus. It is possible to define a scattering factor f_e per electron

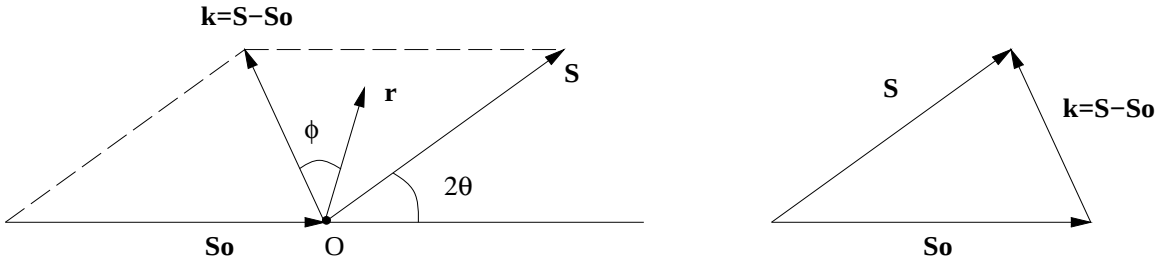

Figure 14: Diagram showing the relationship between the various scattering vectors

as the ratio of the amplitude of unmodified scattering (i.e. non-Compton) from one electron, to the classical amplitude of scattering i.e. Thompson theory, equation (9).

Using the vectors shown in Figure 14, i.e. $\mathbf{S_o}$ the incident photon vector, $\mathbf{S}$ the scattered photon vector, $\mathbf{r}$ the vector to a point in the atom's electron charge distribution and $\mathbf{k}$ is the difference vector as defined in the diagram, it can be shown that [48]:

$$f_e = \int_0^\infty 4\pi r^2 \rho(r) \frac{\sin kr}{kr} dr \tag{14}$$

where

$$k = \frac{4\pi \sin\theta}{\lambda} \tag{15}$$

and λ is the wavelength of the incident beam of X-rays. It should be noted that an assumption of spherical charge distribution about the atom nucleus has been made, giving rise to the $\frac{\sin kr}{kr}$ term, this approximation is more valid for high-$\mathcal{Z}$ elements than for low-$\mathcal{Z}$ elements and covalently bonded systems where the electron distribution about the atoms is non-spherical ($\mathcal{Z}$ being the atomic number).

For multi-electron atoms, the equation for the amplitude of the unmodified scattering becomes the sum of the amplitudes for each atomic electron i.e.

$$f = \sum_n f_{en} = \sum_n \int_0^\infty 4\pi r^2 \rho_n(r) \frac{\sin kr}{kr} dr \tag{16}$$

f is termed the *atomic scattering factor*, and in the above formalism is expressed in terms of electron units i.e. in units of the classical scattering from a single electron as given by the Thompson equation (9). The intensity of the coherently scattered radiation is then given by:

$$I_{coh} = I_e f_e^2 \tag{17}$$

where I_e is the Thompson intensity for a single electron. The f^2 term arises from the fact that the theory of the scattering factor was developed in terms of the electric field amplitude of the incident X-rays and not the incident wave intensity.

The above much simplified theory neglects the effects of non-spherical electron distributions and assumes that the scattering factor is calculated far from any absorption edge, i.e. where the energy of the incident X-ray would cause an atomic electron in the K or L shells (for example) to be released into an unbound continuum energy state. If this is the case, the form of the atomic scattering factor must be modified to include dispersion effects i.e.

$$f \Rightarrow f_0 + \Delta f' + i\Delta f'' \tag{18}$$

Where f_0 is the uncorrected atomic scattering factor and $\Delta f'$,$\Delta f''$ the real and imaginary parts of the dispersion correction.

These two dispersion terms can be used in the technique of *anomalous X-ray scattering*, which allows the environment about particular atom types within a sample to be probed. The amplitude of the scattering factor is calculated by taking the modulus of the above equation i.e.

$$|f| = \left[(f_0 + \Delta f')^2 + \Delta f''^2\right]^{\frac{1}{2}} \tag{19}$$

For normal (non-anomalous) scattering there is a π phaseshift in the wave on scattering, in the anomalous scattering case this becomes $\pi - \psi$ where:

$$\psi = \tan^{-1} \frac{\Delta f''}{f_0 + \Delta f'} \tag{20}$$

In most cases, especially where light atoms and low X-ray wavelengths are used, the anomalous corrections to the atomic scattering factor can be ignored, it is only necessary to consider them when operating at a wavelength close to an absorption edge. The values for the various components of the atomic scattering factor can be found in the *International Tables of X-ray Crystallography* [54].

Another useful result from the wave mechanical treatment, is the equation for the intensity of the modified or Compton scattering. The relevant result is that the sum of the modified and unmodified scattering intensities is equal to the classical scattering for each electron involved i.e.

$$I_{inc} = I_e - I_{coh} = I_e(1 - f_e^2) \tag{21}$$

Another useful relation is that for small values of $\frac{\sin\theta}{\lambda}$ it can be shown that f (in electron units) approaches $\mathcal{Z}$ the atomic number for the atom. Bearing this in mind, the sum of the modified intensities of the scattering from the electrons in an atom can be shown to be:

$$I_{inc} = \sum_n I_{inc_{en}} = \mathcal{Z} - \sum_{n=1}^{\mathcal{Z}} f_{en}^2 \tag{22}$$

3.2.4 Scattering from an amorphous solid

Having presented a basic outline of the processes involved in X-ray scattering, it is now a relatively simple matter to progress to the scattering from an amorphous solid i.e. a material possessing no long range atomic order.

The general equation for the intensity of scattering from a material consisting of differing atom types can be presented in terms of the difference vectors $\mathbf{r_{mn}}$ which are the vectors between atoms at two positions associated with the labels m and n summed over all atoms in the sample i.e. $\mathbf{r_{mn}} = \mathbf{r_m} - \mathbf{r_n}$:

$$I_{eu} = \sum_m \sum_n f_m f_n e^{\frac{2\pi i}{\lambda}(\mathbf{s}-\mathbf{s_o}).\mathbf{rmn}} \tag{23}$$

Since this array of atoms has no directional preferences due to its amorphous nature, the intensity equation can be averaged over all spatial orientations. Performing this averaging in spherical polar coordinates one arrives at the *Debye scattering equation* [48] i.e. :

$$I_{eu} = \sum_{m,n} f_m f_n \frac{\sin kr_{mn}}{kr_{mn}} \tag{24}$$

Where $k = \frac{4\pi \sin\theta}{\lambda}$ as previously defined. The Debye equation represents the average unmodified intensity of scattering from a spatially averaged atomic array.

Considering equation (23) the scattering intensity can be presented as:

$$I_{eu} = \sum_m f_m^2 + \sum_m f_m \sum_{n \neq m} f_n \exp\left[\frac{2\pi i}{\lambda}(\mathbf{s} - \mathbf{s_o}).\mathbf{r_{nm}}\right] \tag{25}$$

Defining a unit of composition uc, (for example a molecule from which the sample is constructed or similarly a stoichiometrically balanced group of atoms suitable for defining the base structure of a glass) and the total number of such units in a sample as N, it is possible to define an average atomic scattering factor per electron as:

$$f_e = \frac{(\sum_{uc} f_m)}{\sum_{uc} \mathcal{Z}_m} \tag{26}$$

Where $\mathcal{Z}$ is the atomic number of atom type m and f_e the scattering factor for an electron. Introducing the constant K_m, the effective electron number, the following relationship is established:

$$f_m = K_m f_e \tag{27}$$

The above pair of equations is an approximation, since K_m will vary with $\frac{\sin\theta}{\lambda}$ but for the present argument it will be treated as a constant. Using this approximation, equation (25)can be rewritten as:

$$I_{eu} = \sum_m f_m^2 + f_e^2 \sum_m K_m \sum_{n \neq m} K_n \exp\left[\frac{2\pi i}{\lambda}(\mathbf{s} - \mathbf{s_o}).\mathbf{r_{nm}}\right] \tag{28}$$

Introducing $\rho_m(\mathbf{r}_m n)dV_n$ as the number of atoms multiplied by their associated K_n, in the volume element dV_n, allows the replacement of the sum with an integral over the sample volume:

$$I_{eu} = \sum_m f_m^2 + f_e^2 \sum_m K_m \int \rho_m(\mathbf{r}_n m) \exp\left[\frac{2\pi i}{\lambda}(\mathbf{s} - \mathbf{s_o}).\mathbf{r_{nm}}\right] dV_n \tag{29}$$

Adding (and later subtracting) a term in the average electron density ρ_e, and disregarding the added term since it corresponds to small angle scattering intensity we have:

$$\begin{aligned} I_{eu} = \sum_m f_m^2 \quad &+ \quad f_e^2 \sum_m K_m \int [\rho_m(\mathbf{r_{nm}}) - \rho_\mathbf{e}] \exp\left[\frac{2\pi i}{\lambda}(\mathbf{s} - \mathbf{s_o}).\mathbf{r_{nm}}\right] dV_n \\ &+ \quad f_e^2 \sum_m K_m \int \rho_e \exp\left[\frac{2\pi i}{\lambda}(\mathbf{s} - \mathbf{s_o}).\mathbf{r_{nm}}\right] dV_n \end{aligned} \tag{30}$$

and let

$$f_e^2 \sum_m K_m \int \rho_e \exp\left[\frac{2\pi i}{\lambda}(\mathbf{s} - \mathbf{s_o}).\mathbf{r_{nm}}\right] dV_n \longrightarrow 0 \tag{31}$$

(This being due to the small angle scattering falling below the angular range of the detector). Then by introducing $\rho_j(\mathbf{r}) = \langle \rho_m(\mathbf{r}_{nm}) \rangle_v$, where j is the atom type index, $\mathbf{r}$ a fixed displacement and the average is over all $\rho_m(\mathbf{r})$ in the sample, i.e. the density at a distance $\mathbf{r}$ from an atom of type j. It is possible to write:

$$I_{eu} = N \sum_{uc} f_j^2 + f_e^2 N \sum_{uc} K_j \int [\rho_j(\mathbf{r}) - \rho_e] \exp\left[\frac{2\pi i}{\lambda}(\mathbf{s} - \mathbf{s_o}).\mathbf{r_{nm}}\right] dV \tag{32}$$

having multiplied through by the total number of atoms of each kind since in an amorphous sample $\rho_j(\mathbf{r}) - \rho_e \to 0$ for distances greater than a few atomic dimensions.

By noting that spherical symmetry applies to an amorphous sample one may write:

$$I_{eu} = N\sum_{uc} f_j^2 + f_e^2 N \sum_{uc} K_j \int_0^\infty 4\pi r^2[\rho_j(\mathbf{r}) - \rho_e]\frac{\sin kr}{kr}dr \tag{33}$$

By introducing

$$i(k) = \frac{\left(\frac{I_{eu}}{N} - \sum_{uc} f_j^2\right)}{f_e^2} \tag{34}$$

the intensity function can be written as:

$$ki(k) = 4\pi \int_0^\infty \sum_{uc} K_j r[\rho_j(\mathbf{r}) - \rho_e]\sin(kr)dr \tag{35}$$

Using the Fourier transform pair of integral equations i.e.

$$\phi(k) = 4\pi \int_0^\infty f(r)\sin(kr)dr \tag{36}$$

$$f(r) = \frac{1}{2\pi^2}\int_0^\infty \phi(k)\sin(kr)dk \tag{37}$$

It is evident from equation (35) that:

$$\sum_{uc} K_j 4\pi r^2 \rho_j(r) = 4\pi r^2 \rho_e \sum_{uc} K_j + \frac{2r}{\pi}\int_0^\infty ki(k)\sin(kr)dk \tag{38}$$

Experiment will most often produce a measure of the sum of the modified and unmodified scattering. This experimental curve can be scaled to absolute units by dividing out the polarization contribution then scaling the curve until it oscillates about the unmodified scattering curve predicted by theory:

$$\sum_{uc}[f_j^2 + i_j(M)] \tag{39}$$

$i_j(M)$ being the intensity of modified scattering in electron units. The final curve represents the sum of the radial distribution functions for each atom type in the compositional unit i.e.:

$$\sum_{uc} K_j 4\pi r^2 \rho_j(r) \tag{40}$$

The peak positions in this curve correspond to interatomic distances within the sample, and the areas beneath the peaks are proportional to the coordination numbers associated with the atoms at the appropriate separations. In fact, in this approximate treatment, the area of the peak is a weighted sum of the contributions from the various atoms at each distance, i.e. weighted as the effective electron number K_m, e.g. in SiO_2 the separation between the atoms gives a peak at 1.62 Å, the area beneath this peak is given by:

$$A = 1K_{Si}n_O K_O + 2K_O n_{Si} K_{Si} \tag{41}$$

with n_O and n_{Si} representing the number of oxygen atoms about silicon and vice versa in the SiO_2 unit.

The above theory is only approximate, and depending on the complexity of the system may or may not be applicable. One of the reasons for this state of affairs is the approximation made when defining the average scattering factor properties, and defining the various K_m which, as previously mentioned, are dependent upon $\frac{\sin\theta}{\lambda}$. These various K_m are also particularly susceptible to the definition of the compositional unit, since if this unit contains atoms from widely different areas of the periodic table of the elements, the heavier atoms tend to dominate the form of the average self scattering factor due to the greater number of electrons they possess. This skewing of the weightings, can lead to problems when evaluating approximate coordination numbers from the radial distribution curve, equation (38).

A more exact formulation of the scattering theory as presented by Warren [48], can be summarised as follows, using the same definitions as above and beginning from equation (25).

Letting $\rho_m(\mathbf{r_{nm}})dV_n$ be the total number of atoms weighted by their respective f_n

in the volume element dV_n at $\mathbf{r_{nm}}$ from atom m. So,

$$I_{eu} = \sum_m f_m^2 + \sum_m f_m \int_{Sample} \rho_m(\rho(\mathbf{r_{nm}}) e^{(2\pi i/\lambda)(\mathbf{S}-\mathbf{S_0}).\mathbf{r_{nm}}}) dV_n \tag{42}$$

Labelling the atom types in the unit of composition as j, $\rho_m(\mathbf{r_{nm}})dV_n$ can be written as:

$$\left(\frac{N}{V}\right) \sum_{uc} f_j dV_n \tag{43}$$

Adding and subtracting a term in ρ_e, as before and, then using the fact that the small angle scattering is generally unobserved, the intensity of scattering can now be written as:

$$I_{eu} = \sum_m f_m^2 + \sum_m f_m \int_S \left[\rho_m(\mathbf{r_{nm}}) - \frac{N}{V}\sum_{uc} f_j\right] e^{(2\pi i/\lambda)(\mathbf{S}-\mathbf{S_0}).\mathbf{r_{nm}}} dV_n \tag{44}$$

where the term added and subtracted is:

$$\sum_m f_m \int_S \frac{N}{V} \sum_{uc} f_j e^{(2\pi i/\lambda)(\mathbf{S}-\mathbf{S_0}).\mathbf{r_{nm}}} dV_n \tag{45}$$

For a fixed displacement $\mathbf{r_{nm}} = \mathbf{r}$, let $\rho_j(\mathbf{r}) = \langle \rho_{\mathbf{m}}(\mathbf{r_{nm}}) \rangle_{\mathbf{j}}$ where the averaging is over all $\rho_m(\mathbf{r})$ at a displacement $\mathbf{r}$ from an atom of type j, then,

$$\rho_j(\mathbf{r}) - \left(\frac{N}{V}\right) \sum_{uc} f_j \to 0 \tag{46}$$

when $|\mathbf{r}|$ is greater than a few atomic dimensions. This then allows the use of the Debye average upon the exponential term in the intensity equation 44, i.e.

$$\langle e^{(2\pi i/\lambda)(\mathbf{S}-\mathbf{S_0}).\mathbf{r_{nm}}} \rangle = \frac{\sin kr_{nm}}{r_{nm}} \tag{47}$$

hence,

$$I'_{eu} = \sum_m f_m^2 + \sum_m f_m \int_S \left[\rho_m(\mathbf{r_n m}) - \frac{N}{V}\sum_{uc} f_j\right] \frac{\sin kr_{nm}}{kr_{nm}} dV_n \tag{48}$$

The $\rho_m(\mathbf{r_{nm}})$ term was only introduced to allow the averaging to be performed, reverting to the use of $\sum_{n\neq m} f_n$ gives,

$$I'_{eu} = \sum_m f_m^2 + \sum_m f_m \sum_{n\neq m} f_n \frac{\sin kr_{nm}}{kr_{nm}} - \sum_m \int_S \frac{N}{V} \sum_{uc} f_j \frac{\sin kr_{nm}}{kr_{nm}} dV_n \qquad (49)$$

At this stage of the theory, it becomes convenient to replace the sum over n by a sum over shells of neighbours, labelled i. N_{ij} is the average number of atoms in a shell i at a distance r_{ij} from an atom of type j. Letting $q_m(r)$ be the fraction within the sample of the surface of a sphere of radius r which is centered on an atom m. Introducing these quantities and extending the integral to infinity since $q_m(r) \to 0$ for large r, the following expression is obtained:

$$I'_{eu} = N \sum_{uc} f_j^2 + N \sum_{uc} f_j \sum_i N_{ij} f_i \frac{\sin kr_{ij}}{kr_{ij}} - \frac{N}{V} \sum_{uc} f_j \sum_m f_m \int_0^\infty \frac{\sin kr}{kr} 4\pi r^2 q_m(r) dr \qquad (50)$$

Now, let $q(r) = \langle q_m(r) \rangle$, where the average is over all atoms m. From it's definition, $q(r) = 1.0$ for $r = 0$ and $q(r) = 0$ for $r >$sample size. Then,

$$k\left(\frac{I'_{eu}}{N} - \sum_{uc} f_j^2\right) = \sum_{uc} f_j \sum_i \frac{N_{ij}}{r_{ij}} f_i \sin kr_{ij} - \frac{N}{V}\left(\sum_{uc} f_j\right)^2 4\pi \int_0^\infty r q(r) \sin kr dr \qquad (51)$$

Multiply by a window function $W(k)$ to improve the convergence of the experimental signal [55] and apply a sharpening factor $\frac{1}{g^2(k)}$ which has the property of decreasing with increasing k and $g(k) = 1.0$ at $k = 0$, an example function could be f_e as used in the approximate theory above. The application of the sharpening function [52] effectively corrects the scattering intensity to that expected from point scatterers, rather than that from diffuse electron distributions; this is mathematically achieved by weighting the interference function to emphasize the contributions of oscillations at high k. The window function [55] serves to reduce spurious peaks introduced into the final Fourier transform of the interference function, by suppressing errors at high

k where the sharpening function has greatest effect. The eventual reliability of the data is somewhat dependent on the balance of these two functions, $g(k)$ and $W(k)$.

Following the application of modification functions $g(k)$ and $W(k)$, equation (51) can be abbreviated using:

$$i(k) = \frac{1}{g^2(k)}\left(\frac{I'_{eu}}{N} - \sum_{uc} f_j^2\right) \tag{52}$$

$$Y(k) = 4\pi \int_0^\infty rq(r)\sin krdr \tag{53}$$

thus,

$$\begin{aligned} ki(k)W(k) &= \sum_{uc} f_j \sum_i \frac{N_{ij}}{r_{ij}} f_i \frac{W(k)}{g^2(k)} \sin kr_{ij} \\ &- \frac{N}{V}\left(\sum_{uc} f_j\right)^2 \frac{W(k)}{g^2(k)} Y(k) \end{aligned} \tag{54}$$

Multiplying by $\sin kr$, and integrating from $k = 0$ to $k = k_m$:

$$\begin{aligned} \int_0^{k_m} ki(k)W(k)\sin krdk &= \sum_{uc}\sum_i \frac{N_{ij}}{r_{ij}} \int_0^{k_m} \frac{f_i f_i}{g^2(k)} W(k) \sin kr_{ij} \sin krdk \\ &- \frac{N}{V}\int_0^{k_m} \left(\sum_{uc} f_j\right)^2 \frac{W(k)}{g^2(k)} Y(k)\sin krdk \end{aligned} \tag{55}$$

By performing a series of integrations by parts, it is possible to show that $Y(k)$ is very small except at small k. Thus it is acceptable to replace the slowly varying quantities in the last term of equation (55) by their values at $k = 0$, and integrating to ∞ i.e.:

$$\frac{N}{V}\left(\sum_{uc} Z_j\right)^2 \int_0^\infty Y(k)\sin krdk \tag{56}$$

Noticing that Y(k) is the Fourier transform of $rq(r)$ we have,

$$2\pi^2 rq(r) = \int_0^\infty Y(k)\sin krdk \tag{57}$$

so the last term of equation (55) is:

$$2\pi^2 rq(r)\frac{N}{V}\left(\sum_{uc} Z_j\right)^2 = 2\pi^2 r\rho_e \sum_{uc} Z_j \tag{58}$$

since $q(r) = 1.0$ for small values of r. Hence equation (55) becomes:

$$\sum_{uc}\sum_{i}\frac{N_{ij}}{r_{ij}}\int_0^{k_m}\frac{f_j f_i}{g^2(k)}W(k)\sin kr_{ij}\sin krdk = 2\pi^2 r\rho_e\sum_{uc}Z_j + \int_0^{k_m} ki(k)W(k)\sin krdk \tag{59}$$

Introducing a set of pair functions $P_{ij}(r)$,

$$P_{ij}(r) = \int_0^{\infty}\frac{f_j f_i}{g^2(k)}W(k)\sin kr_{ij}\sin krdk \tag{60}$$

Since $\sin kr_{ij}\sin kr = [\cos(r - r_{ij})k - \cos(r + r_{ij})k]/2$, an auxiliary function $Q_{ij}(x)$ may be defined to simplify matters,

$$Q_ij(x) = \frac{1}{2}\int_0^{k_m}\frac{f_i f_j}{g^2(k)}W(k)\cos xkdk \tag{61}$$

where

$$P_{ij}(r) = Q_{ij}(r - r_{ij}) - Q_{ij}(r + r_{ij}) \tag{62}$$

It can be noted that the second term, $Q_{ij}(r + r_{ij})$ is generally very small and the first term tends to dominate. Finally, it is possible to write:

$$\sum_{uc}\sum_{i}\frac{N_{ij}}{r_{ij}}P_{ij}(r) = 2\pi^2 r\rho_e\sum_{uc}Z_j + \int_0^{k_m} ki(k)W(k)\sin krdk \tag{63}$$

To make use of this relation, the right side of the equation is evaluated from the experimental data. Various $P_{ij}(r)$ are calculated for specific r_{ij} obtained from knowledge as to the sample composition and calibrating systems such as crystal forms of the material. To evaluate the N_{ij} the area of the pair function peak is scaled to the area of the corresponding peak in the radial distribution function calculated from the right hand side of equation (63) and the required value of N_{ij} noted. When the pair function area has been scaled to coincide with that of the peak in the radial distribution function, its appearance will be as a somewhat higher peak with a narrower width, this being due to its calculation at a specific r_{ij}, whereas the peak in the distribution

function obtained from the amorphous sample will contain contributions from a distribution of such distances. Careful interpretation is required if useful information is to be obtained from this observation.

It can be noted that:

$$\int P_{ij}(r)dr = \frac{\pi}{2} Z_i Z_j \tag{64}$$

although this relationship can only be used with care due to the problems of Fourier transformation of data within a finite range.

Chapter 4

Introduction to EXAFS

In the measurement of X-ray absorption as a function of energy, for any particular sample, observation of absorption edges at energies corresponding to the photoionization of core electrons of atomic species present in the sample are made. An absorption edge can be defined as a step function evident in the probability of X-ray absorption, see Figure 15.

Beyond the absorption edge, the absorption coefficient is seen to possess an oscillatory nature, these oscillations being termed X-ray absorption fine structure. EXAFS spectroscopy or Extended X-ray Absorption Fine Structure spectroscopy is the study of the oscillations from approximately 50 eV beyond an edge out to a distance of a few hundred eV. These oscillations contain structural information on the short range (<6Å) atomic environment of the atom-type whose edge is being probed. Information being gained on interatomic distances, types of surrounding atoms, coordination numbers and short range structural disorder.

As a structural probe, the technique is very useful due to it being atom type specific, generally non-destructive, sensitive to small concentrations of atoms and

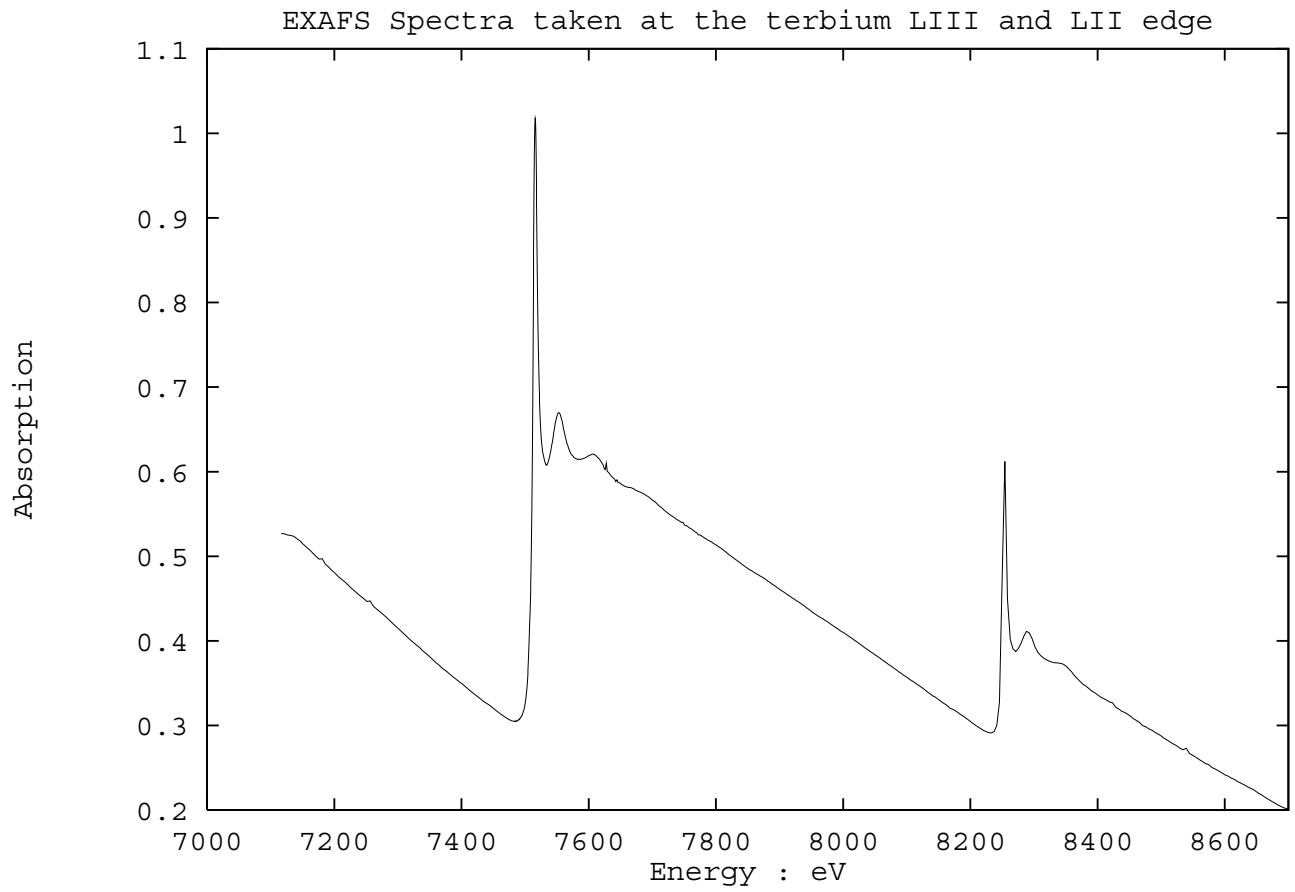

Figure 15: Example of the L_{III} and L_{II} absorption edges for terbium.

providing the above mentioned structural information.

4.1 Simple Theory

The theory of EXAFS has been presented in many papers, books and reviews over the past few years, notably [56, 57, 58, 59, 60, 61]. Here a simplified theory will be presented since a full quantum mechanical treatment is highly complex and a simplified model can provide a conceptual basis for the processes involved. However, it is useful to refer to quantum mechanical results where they are fundamental to the description of the phenomenon.

EXAFS is best considered as an electron scattering process which modulates the absorption properties of the material under investigation. The incident X-ray photon strikes an atom of the species susceptible to excitation at this energy, $h\nu$, where h is Plancks constant and ν is the photon frequency, liberating a core electron from either the K or L shell (figure 16). This freed electron propagates away from the excited atom, and is backscattered from surrounding atoms, the backscattered waves interfering with the outgoing wave. This interference is the cause of the modulation seen in the absorption signal.

Provided that the wavelength of the the incident photon is larger than the size of the electron initial state, the process can be modelled using Fermi's Golden Rule with the dipole approximation i.e. the probability of absorption being given by:

$$P = \frac{2\pi^2 e^2}{hc^2\omega} \left| \int \psi_f^* \boldsymbol{\epsilon}.\mathbf{r}\psi_i d^3r \right|^2 \rho(E_f) \tag{65}$$

where ψ_i is the initial state wave function of the electron, ψ_f the final state wave function, $\boldsymbol{\epsilon}$ the polarization state vector of the incident X-ray, $\mathbf{r}$ the position vector of the electron and $\rho(E_f)$ the density of final states to which the electron is excited. The

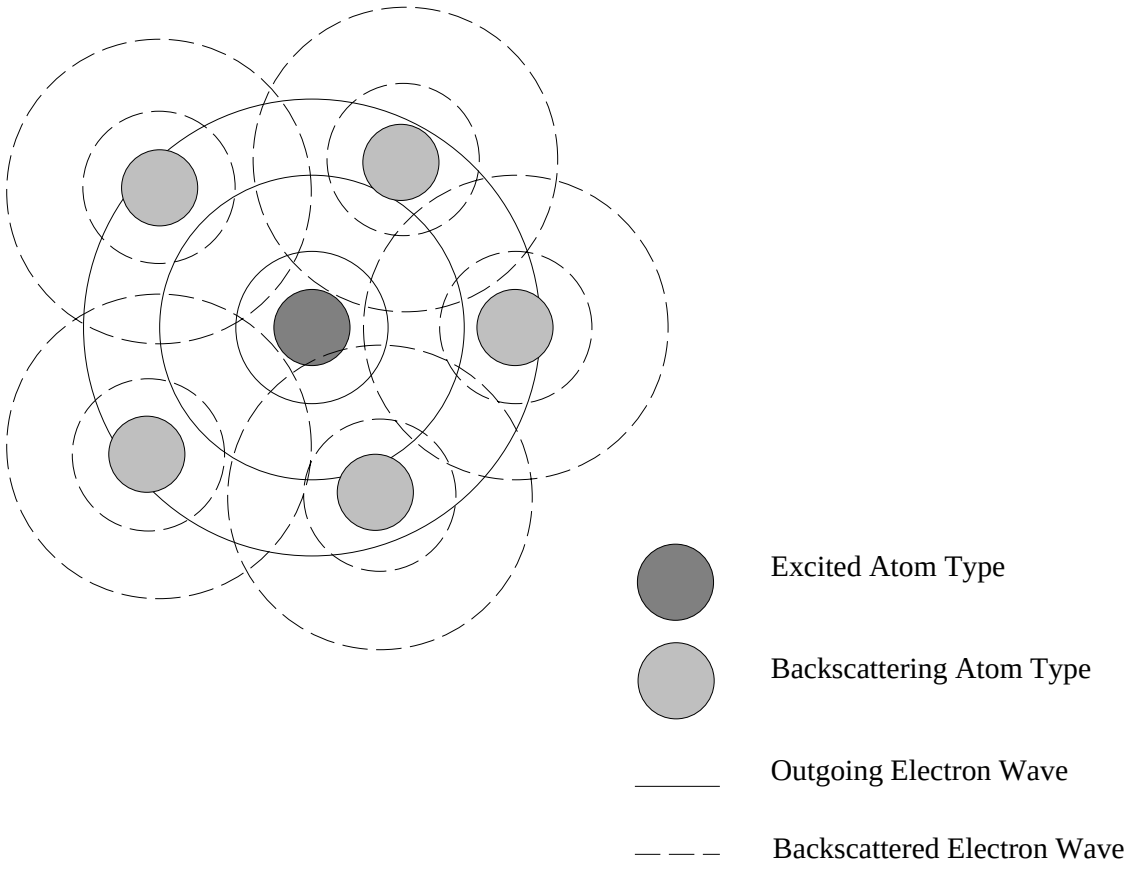

Figure 16: Example of core electron excitation and propagation

other terms having their usual meanings i.e. e being the charge on the electron, h being Plank's constant, c the speed of light in free space and ω the angular frequency of the X-ray photon.

For energies well above the absorption edge, the density of final states can be approximated by that of a free electron. Such an electron having a momentum given by $\mathbf{k}$ where $k = 2\pi/\lambda$ and λ is the electron's wavelength. The energy associated with such an electron is given by $\hbar^2 k^2/2m$ which can be equated with the energy of the incident, exciting X-ray photon by the following relationship:

$$E_{electron} = E_{photon} - E_{edge} + E_0 \tag{66}$$

where E_0 is termed the threshold energy, and is a correction constant to allow for the absorption edge occurring not at the Fermi energy but at the energy of the lowest unoccupied state i.e. E_{edge}.

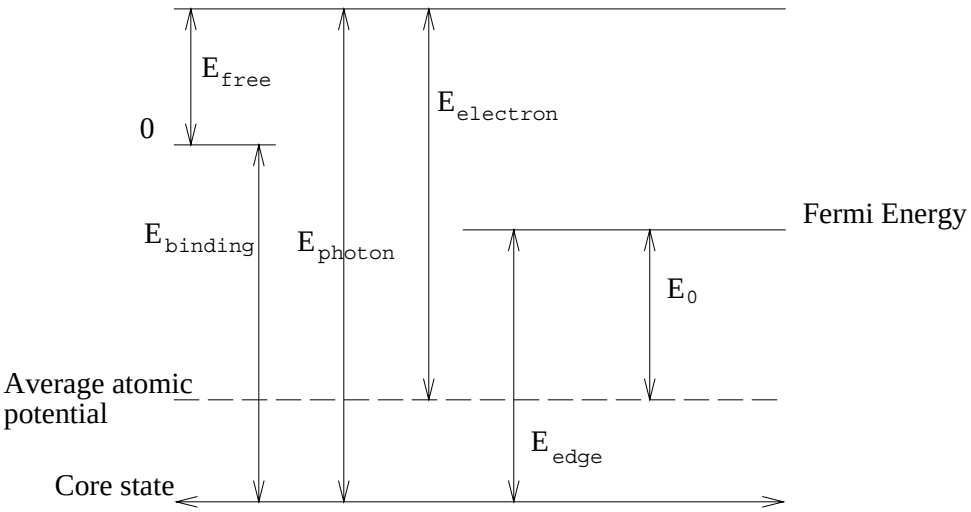

Figure 17: Summary of energies used in the description of EXAFS

Consideration of equation (65) shows that the only term which can vary to give rise to the EXAFS oscillations is the matrix element ψ_f. EXAFS is therefore considered a final state interference effect.

The excited electron is assumed to have been freed into the continuum of states, propagating away from the central atom as a spherical wave. The scattering of this electron from the surrounding atomic potentials, induces a phase shift in the backscattered portion of the wave, but these backscattered waves are still coherent with the outgoing wave and hence interfere. The freed photoelectron leaves a core hole in its wake, i.e. the excited atom is left in an unstable state eventually leading to relaxation of its electron system, this relaxation destroys the coherence of the propagating photoelectron with the backscattered waves and hence is a damping factor on the EXAFS signal.

Relating this phenomenon to the presence of the surrounding atoms allows the representation of the total absorption coefficient μ as the sum of two constituent parts. The absorption which would be evident if no backscattering atoms were present μ_0, and the modulatory function χ, arising from the interference effects on the final state wave function ψ_f i.e.

$$\mu(k) = \mu_0(k)[1 + \chi(k)] \tag{67}$$

From this defining equation, EXAFS becomes the problem of determining the function $\chi(k)$.

Obtaining an analytical form for the function $\chi(k)$ is a very complex process, beginning with the expansion of the electron wave functions into series of angular momentum eigenfunctions. This theory is too complex to be covered here, but many of the aforementioned texts present these detailed derivations.

When evaluating the theory of EXAFS, several different approximations can be made to render the task of data analysis computationally viable. For example, assuming an amorphous sample allows the spatial complexity of the problem to be greatly reduced, due to the lack of any orientational preference of the system being studied.

Other approximations which are commonly made are the plane wave approximation, where the propagating electron wave is considered distant enough from the source atom, that it may be modelled as a plane wave incident upon the backscattering potential. The small atom approximation [62], which is an improvement on the plane wave theory, applicable in the case of the excited atom being relatively small on the scale of the curvature of the backscattered wave. The fast curved wave theory [63], which is a simplification of the full curved wave theory as presented by Lee and Pendry [56], making use of the amorphous system approximation previously mentioned.

For a discussion of the factors affecting the EXAFS phenomenon, a consideration of the Plane Wave (PW) theory is quite satisfactory, since all the major corrections are easily identified and explained. The plane wave theory is represented using the equation:

$$\chi(k) = A(k)\sum_j \frac{N_j}{kR_j^2}\,|f_j(k,\pi)|\sin(2kR_j + 2\delta + \psi_j)e^{\frac{-2R_j}{\lambda}}e^{-2\sigma_j^2k^2} \qquad (68)$$

$A(k)$ is a term to account for inelastic scattering processes such as the electron *shake-up* effect, where other electrons in the excited atom potential are perturbed, the end result being a relaxation of the excited $\mathcal{Z}+\infty$ potential of the atom, where $\mathcal{Z}$ is the atomic number. The reason that the potential is perceived as $\mathcal{Z}+\infty$, is because the shielding of the outer electrons from the nuclear potential of the excited atom has been reduced by the emission of the photoelectron. Also there is the accompanying possibility of the liberation of a secondary electron to the continuum of states, i.e. electron *shake-off*, to cater for the excess of potential energy in the system due to the core electron hole relaxation. Both these processes damp the EXAFS signal and hence the necessity for the introduction of the amplitude reduction term $A(k)$.

N_j is the number of backscattering atoms of type j at a distance R_j, $|f_j(k,\pi)|$ is the measure of their associated backscattering potential. δ_j is the phase shift induced

in the photoelectron wave on passage through the excited atom potential, experienced once on passage away from the central atom and once on return, hence the factor of 2. ψ_j is the phase shift induced on passage through the potential of atom type j, during the backscattering of the wave. λ is a measure of the mean free path of the electron within the sample as well as including a contribution from the finite lifetime of the core hole. $e^{-2\sigma_j^2 k^2}$ is the Debye-Waller term to account for structural disorder within the system under investigation.

The origins of λ are worth considering. Breaking it down into the two contributing factors of core hole life time and electron mean free path, show it to arise from the uncertainty principle. The core hole having a finite lifetime, can be shown to have an associated finite energy width due to the energy/time uncertainty relation. This width is essentially that of the absorption edge and is denoted Γ_c, it can be introduced into the theory as a damping factor $e^{\frac{-2\Gamma_c R_j}{k}}$; the $2R_j$ term (rather than R_j) is because the length of the scattering path is twice the atom separation - neglecting multiple scattering paths. Similarly, the propagating electron has a finite lifetime for interference effects due to the relaxation of the core hole destroying the coherence relationship between the outgoing and return waves; this lifetime introduces a term denoted Γ_e, in a similar fashion to the core hole energy width term. Converting to mean free paths i.e.:

$$\lambda_c = \frac{k}{\Gamma_c} \tag{69}$$

$$\lambda_e = \frac{k}{\Gamma_e} \tag{70}$$

generates the mean free path correction term used in the PW equation (68):

$$e^{\frac{-2R_j}{\lambda}} = e^{\frac{-2R_j}{\lambda_c}} . e^{\frac{-2R_j}{\lambda_e}} \tag{71}$$

The other damping term in the PW equation (68), i.e. the Debye-Waller term

$exp(2\sigma_j^2 k^2)$, accounts for the extent of short range structural disorder present in the backscattering system. This disorder having two sources, one static and one thermal, generally modelled as:

$$\sigma^2 = \sigma^2_{stat} + \sigma^2_{vib} \tag{72}$$

where σ_{stat} is a measure of the structural disorder present in the absence of thermal motion, whose contribution is denoted as σ_{vib}. Assuming the disorder to fall in a gaussian distribution, the term is included as an exponential function given by $e^{-2\sigma_j^2 k^2}$ where σ_j^2 is the mean square variation in the interatomic distances of atoms of type j. The vibrational component of the Debye-Waller term is not an independent measure for the motion of the individual atom type j, this is due to a degree of correlation between the vibrations of the core atom with those of the surrounding atoms. Also there is in general, a smearing effect of the EXAFS Debye-Waller term due to uncertainty in the positions of the core and backscattering atoms during the propagation of the electron waves and hence the values obtained from EXAFS experiments cannot be directly compared with disorder effects measured from diffraction experiments, which measure absolute magnitudes.

4.1.1 Phaseshifts

The calculation of the phaseshifts δ and ψ, affecting the ejected photoelectron, is the foundation for the chemical specificity of the technique. Differing atoms types have characteristic atomic potentials and hence induce type-specific phaseshifts in the EXAFS signal. These phaseshifts are often an area requiring particular care in the data analysis process since they can have marked effects on the final results, for interatomic distances as well as atom types. Differentiation between atom types, which are close in the periodic table can be difficult due to their similar coulombic

potentials and hence scattering properties of the electron wave.

Methods for determining reliable phaseshifts are improving, and theoretical calculations now produce reasonable results. Problems do however still exist and if possible the use of *standards* to calibrate the parameters used in the analysis is advised. These calibrants, should be systems of similar chemical nature to the specimen being studied, but well characterised in terms of structural properties, i.e. have well known interatomic distances and coordination numbers. EXAFS spectra taken from these standards may then be used to refine the parameters of the theoretically calculated phaseshifts.

The degree of transferability of phaseshifts from calibrant to unknown has however been a contentious topic for many years. This mainly being due to the effects that differing local atomic environment can have on the interatomic potentials. It is becoming more widely accepted that, in general these phaseshifts can be transferred but they must always be considered as one of the central points in the evaluation of the final data. For complex systems, calibrants may not be available, and reliance on the theoretical models is necessary; this is unfortunate but information of acceptable quality can be obtained.

Chapter 5

Instrumentation

5.1 The Synchrotron Radiation Source

The performance of X-ray experiments was greatly improved with the advent of synchrotron radiation sources (such as the SRS, at the Daresbury Lab. UK). Advantages offered over laboratory based X-ray generators are numerous, notably:

- High beam intensity
- Wavelength selectivity from a broad spectral range
- High degree of beam collimation
- Better than 95% polarization in the plane of the accelerator
- Fixed time structure induced by the r.f. cavities

A reasonable overview of synchrotron radiation is presented by Catlow and Greaves [64]. Figure 18 shows a schematic of a synchrotron radiation source.

The principle behind a SRS is that when charged particles moving at relativistic speeds undergo an acceleration e.g. when forced to follow a curved trajectory, they

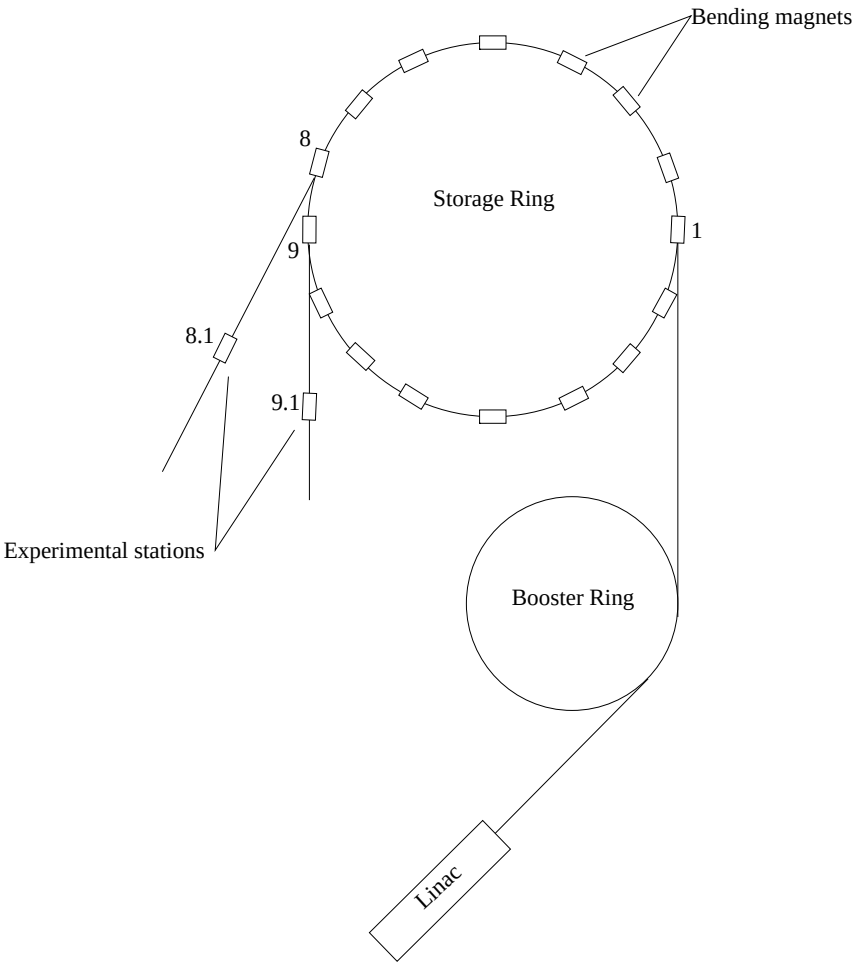

Figure 18: The SRS

emit electromagnetic radiation with a wide range of wavelengths (from far infrared to X-ray), i.e. they can be considered as sources of *white* radiation. This electromagnetic radiation is emitted tangentially to the path followed by the charged particle, within a very tightly collimated angular range in the acceleration plane. The beam of EM radiation is also highly polarized in this plane.

The characteristic shape of the spectrum of *white* radiation is shown in Figure 19. This diagram also shows the shift in the position of the maximum intensity wavelength on the inclusion of a superconducting high field magnet. The shift in energy is due

to the charged particles moving through a path with a smaller radius of curvature, i.e. they experience a greater acceleration.

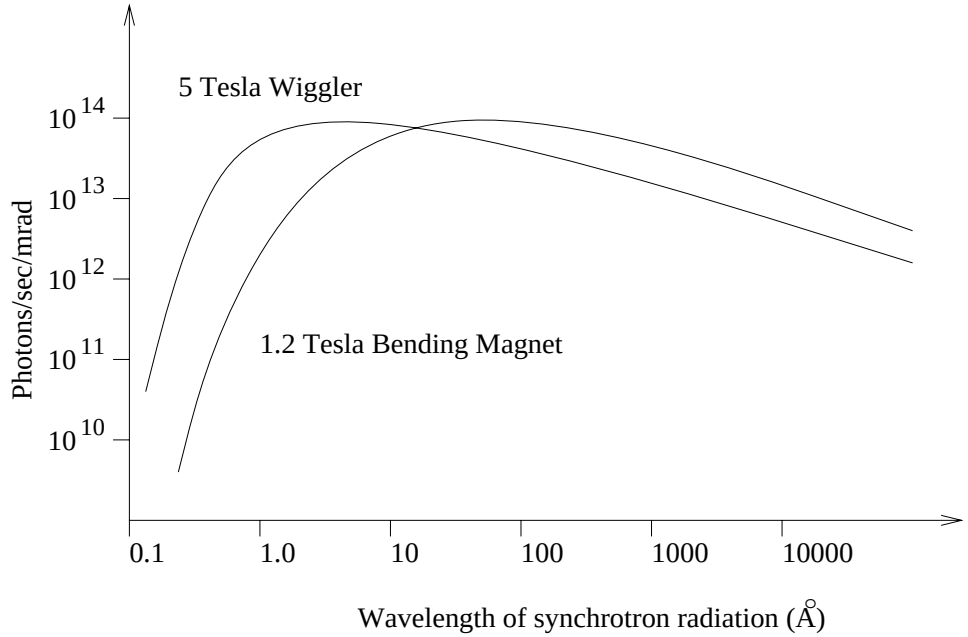

Figure 19: Effect of a wiggler on radiation spectrum

At the Engineering and Physical Sciences Research Council's (EPSRC) Daresbury Laboratory, the SRS facility consists of a Linac, (linear accelerator) which accelerates electrons produced at a hot cathode up to an energy of about 12 MeV, these electrons are then injected into a booster ring and are further accelerated to 600 MeV. From the booster they are finally placed into the storage ring itself, this ring having a circumference of 96m. Once in the storage ring, the final stage of acceleration up to the working energy of 2 GeV is performed. On the main storage ring there are sixteen 1.2 Tesla dipole bending magnets, these bending magnets are connected by straight sections along which are placed quadrupole focussing magnets and the r.f. cavities which provide the energy to keep the electrons moving. The typical beam currents used are usually around 200 mA, but values up to 300 mA are attainable.

The r.f. cavities are all connected to a klystron, which maintains the synchronisity of the electrons which travel round the ring in bunches by applying the r.f. pulse which accelerates the electrons. The bunching is actually a necessary side effect of acceleration by r.f. cavities.

The entire system, linac to storage ring is kept under ultra-high vacuum, (10^{-12} – 10^{-13} bar), which prevents loss of electrons due to scattering out of their orbits. The Daresbury SRS also has two superconducting magnets termed wigglers, which introduce a sinusoidal motion to the electron paths when passing through these sections of the ring. This induced oscillation has the effect of shifting the energy peak of the white beam to smaller wavelengths, as demonstrated earlier in Figure 19. Only one of these wigglers is relevant to this work, that on beamline 9, which is a 3 pole, 5 Tesla magnet.

Each of the bending magnets on the storage ring at the Daresbury Laboratory is identified by a number, the evacuated pipes which carry the synchrotron radiation to the experimental stations each come off the storage ring tangentially at one of the bending magnets, and the stations themselves are known by a number such as 8.1 or 9.1 etc.. The first number being the bending magnet identifier and the second the position of the station along the evacuated tangential beam pipe, several stations being assigned to each pipe. The beamline associated with the wiggler and its *hard* X-ray radiation is beamline 9.

To make use of the full potential of synchrotron radiation, the experimental stations are fitted with monochromating crystals to select the particular wavelength desired from the *white* radiation supplied. These monochromators work on the simple principle of Bragg's law i.e.

$$n\lambda = 2d\sin\theta \tag{73}$$

Where n is the harmonic number, λ the wavelength, d the separation of the crystal planes and θ the angle of incidence upon the crystal. Channel cut crystal monochromators are often used on the experimental stations, see Figure 20. These are single crystals with a channel cut for the beam to travel down, orienting this channel can thus select the wavelength transmitted. In the case of station 9.1 at the Daresbury Laboratory, the monochromator is a silicon channel cut (two bounce) monochromator e.g. Figure 20, aligned along the 111 crystal axis and water cooled to provide stability of the selected wavelength against any heating effects induced by the incident X-ray beam. If very precise energy/wavelength resolution is required, a double crystal monochromator can be used, this consists of two channel cut monochromators oriented so that the beam will undergo 4 *bounces* before leaving the monochromator. A slight disadvantage of a twin crystal system is that the beam is attenuated with each *bounce* of the beam, thus requiring longer counting times if good statistics are desired.

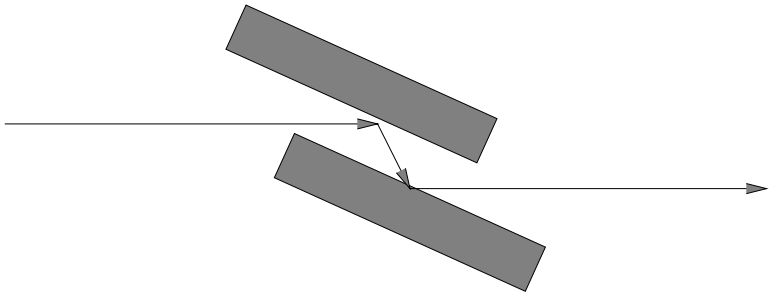

Figure 20: Channel cut 2 bounce monochromator

Examination of equation (73) shows that for any crystal orientation not only the primary wavelength would be transmitted, but higher order harmonics as well. This problem can be overcome by cutting the channel in the monochromator crystal slightly off parallel on one side, having the effect of attenuating the higher order harmonics far more strongly than the primary wavelength. A similar suppression

of the harmonics can be achieved with the double crystal arrangement if one of the crystals is set slightly off the angle required for maximum beam transmission.

This suppression of harmonics often termed *harmonic rejection*, is particularly important when performing EXAFS experiments since the presence of higher energy harmonics within the beam illuminating the sample would cause the generation of excitation effects contaminant to the EXAFS signal. To account for this the monochromator system is generally offset during these experiments to give harmonic rejection ratios (HRR) of typically between 50% and 70%, i.e. the transmission is set to, for example 70% of peak value as measured by the monitor ion chamber. The choice of HRR is dependent upon the widths of the transmission peak profiles of the respective harmonics, typically higher harmonics having narrower profiles. Hence, by offsetting the monochromator crystals slightly there is a greater reduction in the higher harmonic intensity than in the fundamental.

A schematic diagram of an experimental station used for X-ray diffraction work at the Daresbury Laboratory is shown in Figure 21. Whilst a typical EXAFS station is shown in Figure 22, although the presence of a focussing mirror in the station optics is not generally needed for most EXAFS stations. This mirror provides a greater photon flux to fall upon the sample.

5.2 Outline of a $\theta/2\theta$ Diffraction Experiment

Figure 23 shows a typical geometry used in a diffraction experiment at a synchrotron source. The white beam of X-rays is monochromatised to a chosen wavelength and passes through a pair of beam profile definition slits, which determine the beam footprint to be incident upon the sample. Between the sample and the definition slits is a piece of kapton foil which scatters a small percentage of the incident beam to a

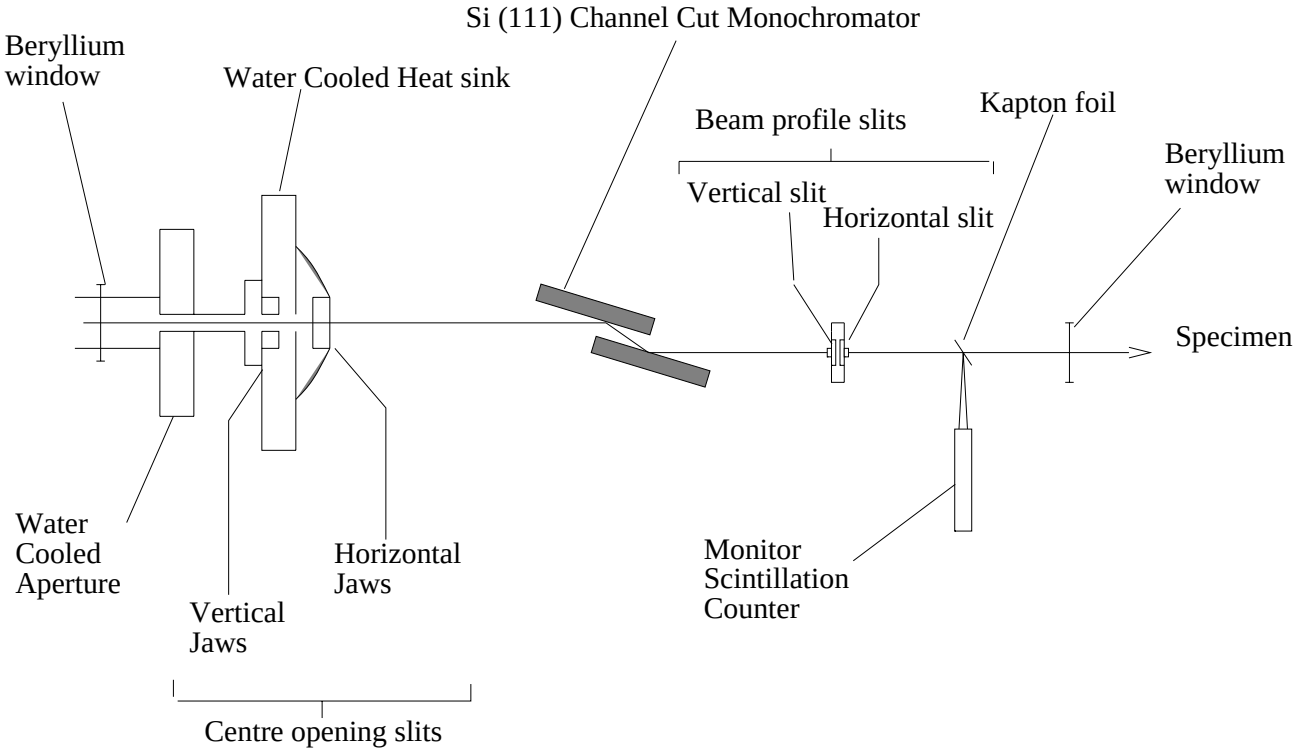

Figure 21: Station 9.1 at the SRS, Daresbury

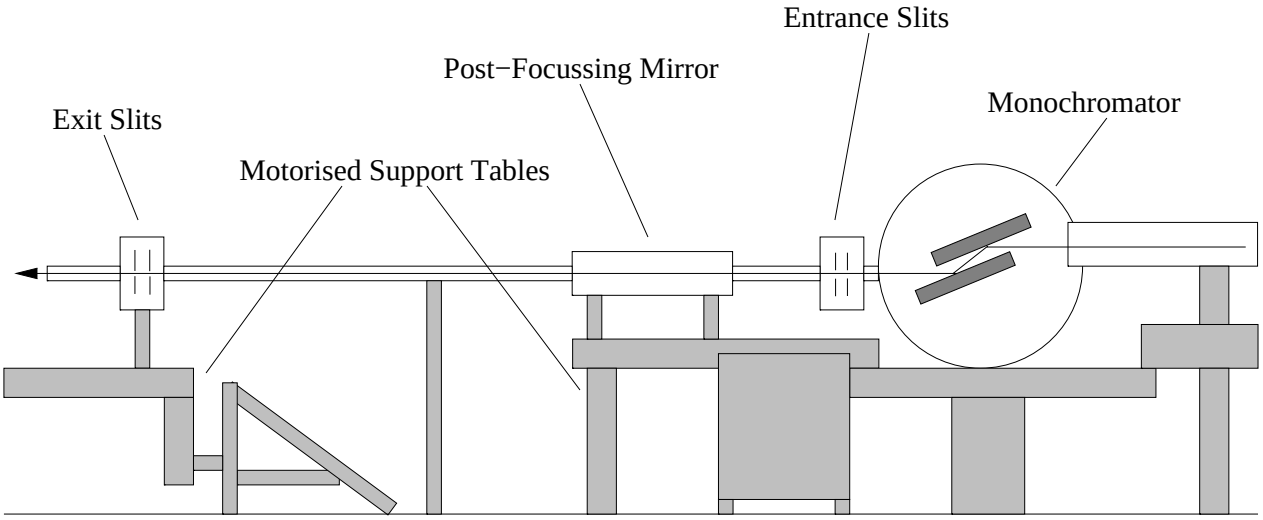

Figure 22: Station 8.1 at the SRS, Daresbury

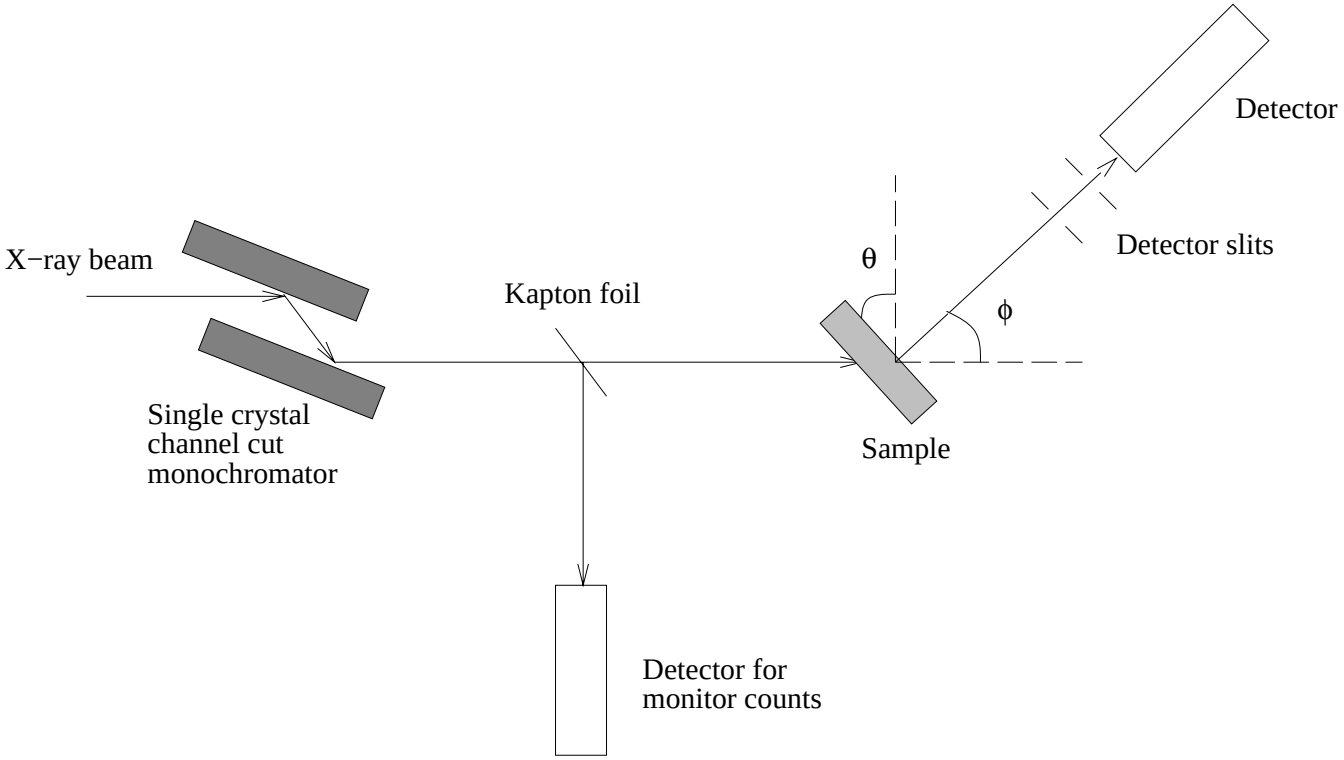

Figure 23: Schematic of a diffraction experiment

monitor scintillation counter, a necessary task if the final data is to be normalised. The beam is incident upon the sample which is mounted on a motorised stage, allowing rotation, and the main scintillation counter which collects the diffraction signal is itself mounted on a rotational arm, with axis centered upon the sample's centre of rotation. When performing a $\theta/2\theta$ experiment the scattering angle ϕ is fixed so as to always be twice the angle of sample orientation θ, a geometry which much simplifies the corrections which later have to be applied to the data.

When performing the experiment, a sample of suitable thickness usually $\mu t < 1$ where μ is the linear attenuation coefficient and t the thickness, is placed in the X-ray beam. The choice of thickness is quite important since if this is excessive, multiple scattering corrections become important, these are generally difficult to perform well and best avoided if at all possible, and the associated problem of absorption, the reduction in detected count rate caused by excessive attenuation of the beam due to photoelectric absorption in the sample. If the thickness is too small the scattering cross section presented by the sample will be insufficient to give acceptable count rates. i.e. the same problem at the other extreme. The scan then proceeds at a known wavelength, with typical angular ranges being 1° to 65° for θ in steps of 100mdeg and, 2° to 130° in steps of 200mdeg for $\phi = 2\theta$. These scan ranges are suitable for experiments upon amorphous systems where accurate position of Bragg features is not important. For each angular step of the scan, the detector is set to count for either a fixed period of time at each point or until a certain number of detected photons have been collected. Either of these methods allow simple normalisation of the final data.

5.3 Outline of an EXAFS experiment

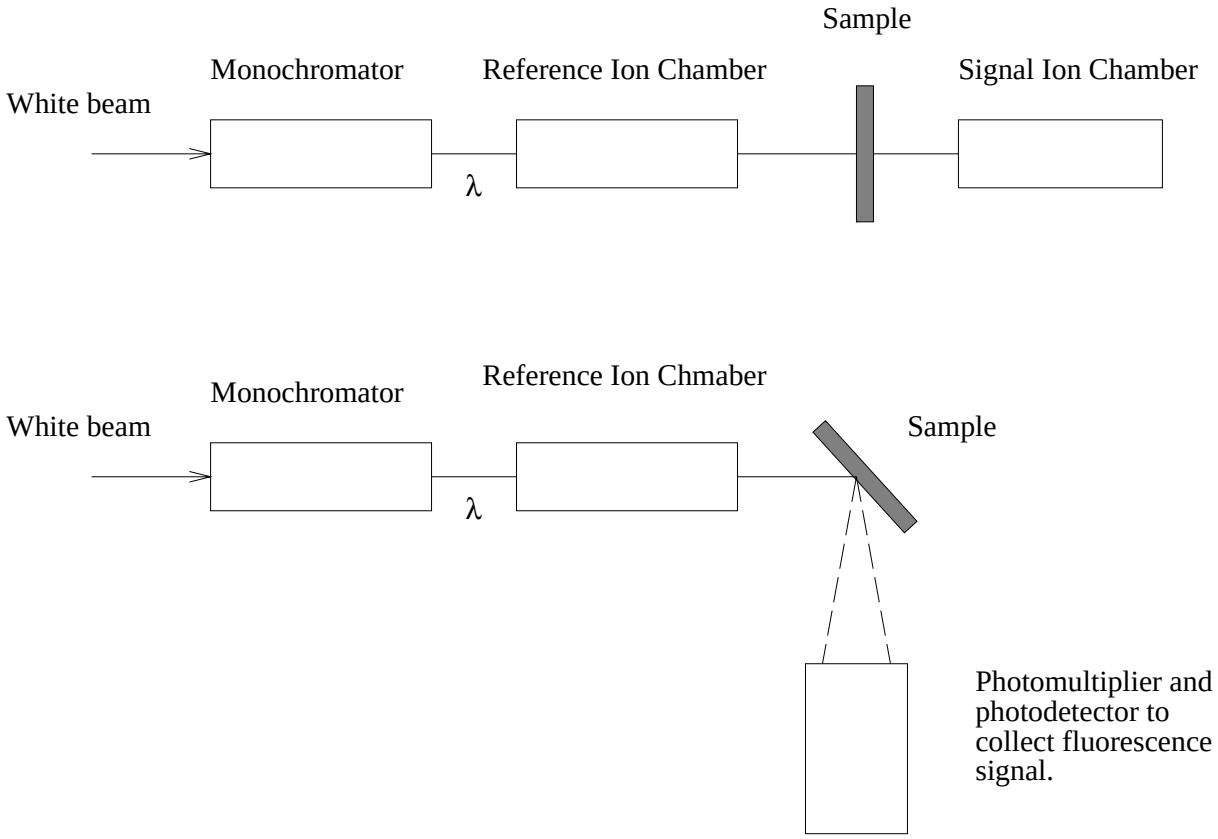

Figure 24: Schematic of a transmission and a fluorescence EXAFS experiment

Figure 24 show the two principle geometries used for the performance of EXAFS experiments, these being:

- Transmission
- Fluorescence

Photoelectric absorption of an X-ray beam passing through a sample, can be described using the equation:

$$I = I_0 e^{-\mu x} \tag{74}$$

where I is the intensity of the X-ray beam after passing through the sample, I_0 the intensity prior to any absorption, $\mu(E)$ is the absorption coefficient of the sample and x the thickness of the sample. This is usually rewritten as:

$$\mu x = \ln\left(\frac{I_0}{I}\right) \tag{75}$$

Simple examination of Figure 24 shows that in the transmission geometry, the two ion chambers Ion_{ref} and Ion_{sig} provide a direct measurement of the 'before sample' and 'after sample' beam intensity.

An associated phenomenon with photoelectric absorption is X-ray fluorescence, a process which can be related to the total absorption coefficient μ_T at a particular energy E. For thick samples, the relationship between fluorescence intensity, I_f and the incident beam intensity, I_0 is:

$$\frac{I_f}{I_0} \approx \frac{\mu(E)\sin\theta}{\mu_T(E)/\sin\theta + \mu_T(E_f)/\sin\phi} \tag{76}$$

where θ is the entrance angle for the X-rays into the sample, ϕ the exit angle of the fluorescence x-rays of energy E_f. Equation (76) is integrated over all ϕ subtended by the detector. This equation is only approximate, but for dilute samples $\mu_T(E)$ is more or less a constant and the overall correction to obtain $\mu(E)$ is small.

Samples are prepared for EXAFS experiments in a number of fashions, often being powdered and mixed with boron nitride or polyethylene, then pressed into a pellet. The aim is to produce samples which have an edge step of height 1, i.e. in the difference between the pre-edge absorption and the post-edge absorption. Care must be taken that the sample is of uniform thickness and that there are no 'pin-holes' evident, these are problems that can produce unphysical effects in the final data.

Samples for fluorescence experiments must be dilute in the excited atom type if problems with effects such as self absorption of the fluorescence photons are to be

avoided. Typical dilutions range from a few thousand parts per million down to a few hundred. This technique demonstrates the sensitivity of EXAFS spectroscopy, a major advantage over most other structural probes.

Another technique often used for EXAFS spectroscopy is detection of Auger electron emission and is a process which is related to the absorption of X-rays. This technique requires the sample to be in an evacuated environment since the emitted Auger electrons are highly susceptible to capture by surrounding atoms, attenuating the EXAFS signal.

Chapter 6

Data Correction Procedures and Analysis

6.1 X-ray Diffraction

Before analysis of X-ray diffraction data can be performed, a series of corrections must be made to the raw intensity data obtained from experiment. The corrections and processing steps which need to be performed arise from:

1. Detector dead time,
2. X-ray beam polarization,
3. Data normalization to constant incident flux,
4. Background scattering from sample environment,
5. Scattering volume variation,
6. Compton scattering contribution,

7. Sample absorption,

8. Isolation of the interatomic scattering signal from the underlying self scattering of the sample's constituent atoms,

9. Binning the data from a function of angle to a function of the scattering vector $\mathbf{k}$.

It is simplest to consider samples which have flat parallel sides, either by virtue of the sample itself or the containment cell, and the performance of the diffraction experiments using the $\theta/2\theta$ experimental geometry. These two criteria allow the presentation of the corrections in the simplest possible fashion.

The aim of these initial data corrections is to obtain the interference function $i(\mathbf{k})$ as presented in equation (34).

6.1.1 Dead time corrections

This correction is necessary since, as the flux of incident photons on the detector increases, the arrival of each photon is increasingly less likely to be resolved into an individual event by the detector electronics. The dead time is defined as the time period between two resolvable events and is obviously a detector-dependent quantity which can be accounted for using the relation:

$$I_t = \frac{I_{obs}}{1 - \tau I_{obs}} \tag{77}$$

where τ is the dead time, I_{obs} is the measured intensity in counts per second (cps) and I_t the corrected intensity. It should be noted that there is always the possibility that two events will coincide at the detector causing *pulse pile up*, but this effect can usually be ignored. Typically, if $\tau = 10^{-6}$s, the error induced by ignoring the dead time correction would be of the order of 1% on a count rate of 10000 cps.

6.1.2 Polarization factors

These account for the fact that the intensity of the diffracted beam is dependent upon the polarization of the X-ray beam incident upon the sample. The origin of these factors can be seen in the Thompson theory of scattering from a free electron, equation 9. The form that this correction takes is:

$$I_p \propto \frac{I_t}{(P_\perp + P_{||} \cos^2 \phi)} \tag{78}$$

where I_p is the polarization corrected intensity, $P_\perp$ and $P_{||}$ are the percentage of perpendicular and parallel polarized X-rays (perpendicular and parallel to the plane of scattering) in the beam respectively, ϕ is the angle of the diffracted beam. These parameters are source dependent; for the 9.1 powder diffractometer at the SRS (Daresbury Laboratory, UK) for example, approximate values are 90% $P_\perp$ polarized X-rays and a 10% $P_{||}$ polarization content. The polarization of the incident beam will also depend on the number of reflections within the monochromator system; each of which would increase the value of $P_{||}$. The form of this correction to be applied to the data is shown in Figure 25.

6.1.3 Normalization

This step in the data processing is to account for time dependent variations in the incident flux of X-rays during the period of the measurement and to allow for the varying collection time for each detector angle. (The latter variation being required in order to ensure a near uniform statistical quality for the entirely diffuse scattering from an amorphous sample). It is performed by dividing the data set by the monitor count obtained from the fixed detector placed before the sample, see Figure 23. At this point, it may be convenient to scale the resulting data by multiplying by a constant

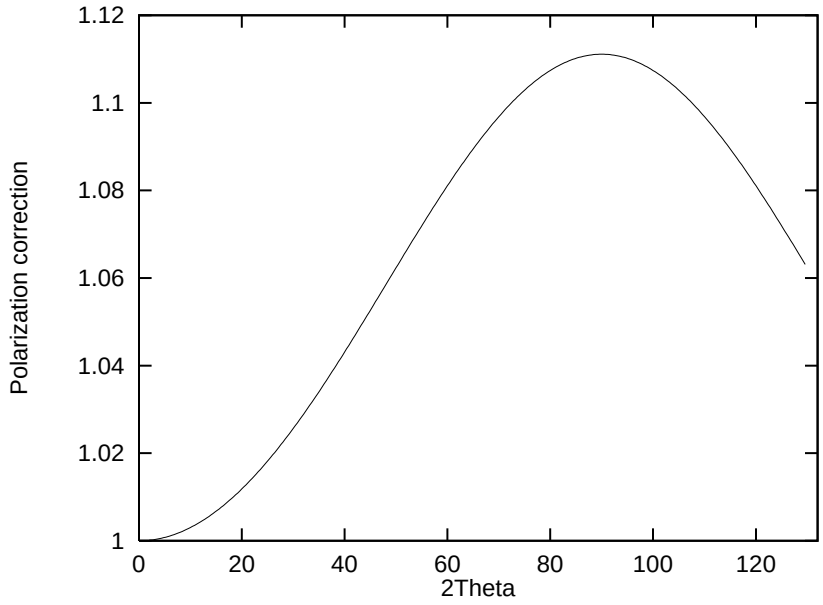

Figure 25: Form of the multiplicative polarization correction for station 9.1, SRS, Daresbury

corresponding to a constant flux of photons per second.

$$I_N = A\frac{I_p}{I_m} \tag{79}$$

I_N is the normalized intensity, I_m the monitor intensity, A is the nominal constant counts per second to which the normalisation is scaled. It should be noted that it is necessary to correct the monitor count for any system dead time effects, since this detector will experience similar problems to the main detector if a high flux of X-rays is present.

Figure 26 shows a diffraction data set, simply corrected for detector dead time and normalized to constant incident flux.

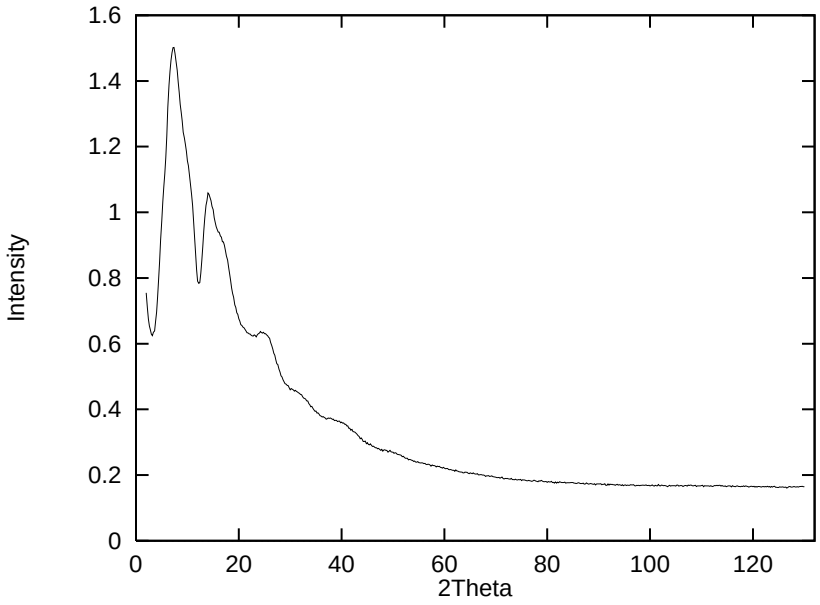

Figure 26: Diffraction data set, detector deadtime corrected and constant flux normalized

6.1.4 Background corrections

It is necessary to take into account the contribution to scattering from the sample holder, and the surrounding air and instruments. This is done by performing scans over the same angular range as the sample scan, with an empty sample container, and then in the absence of the container. These two background scans i.e. the container scan and the air scan can then be used to correct the sample data for background effects. It should be noted that the exact, or full correction must account for the absorption of the container scattering within the sample, the scattering of photons by the sample into the container, the scattering of photons from the container into the sample etc.; this second order correction is usually too small (and often too complex) for practical application. The two background scans should be corrected for dead time and beam polarization, then normalized to constant flux in the same fashion as the sample data. Then, both the sample scan and the container scan should be corrected

for air scatter, a simple process achieved by subtracting the air scan from both the sample data set and the container data set. This is necessary since if the sample is highly absorbing, only applying the container background correction would result in insufficient air scatter being removed from the low angle region of the sample data set. Before subtraction of the container scattering from the sample scan, a multiplicative constant has to be applied to the background intensity to account for sample cell effects such as attenuation of the beam on passage through the cell caused by the presence of the sample, and air scatter which replaces the scatter from the sample in its absence, i.e. the background must be corrected for all changes introduced to the scattering system on removal of the sample, therefore:

$$I_{bc} = (I_N - I_{air}) - B(I_b - I_{air}) \tag{80}$$

where I_{bc} is the background corrected intensity, B the multiplicative constant for sample absorption and I_b is the corrected intensity of the container background scan and I_{air} is the air scan taken in the absence of both sample and cell. The value of B is chosen so that any features in the background intensity scan e.g. steps or spikes which appear in the pre-background corrected sample scans due to cell effects, are removed on background subtraction. Errors in performing this correction should be minimised by ensuring low absorption and low cell scattering, if this is the case, the constant B can be set to a value of, or close to 1.

Other phenomena which may have to be accounted for when correcting for background, are fluorescence and Resonant Raman Scattering [65, 66], both of which can occur when the incident X-ray energy is close to an atomic absorption edge for one of the sample's constituent elements. These effects occur due to the creation of a core hole in the inner electron shells of the photon absorbing atom. When the incident X-ray excites an electron from one of these shells into a continuum state, this

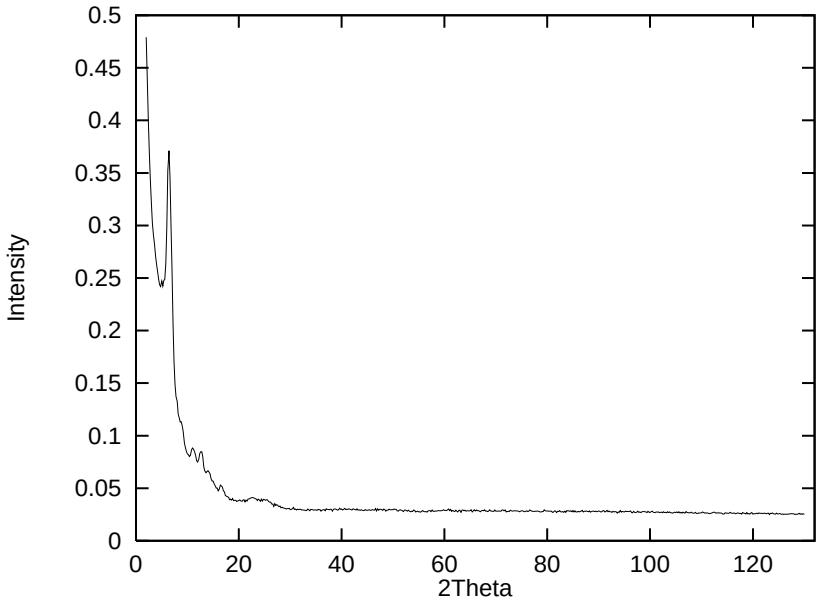

Figure 27: Diffraction background scan taken from a tape-windowed sample cell.

core hole is consequently relaxed by an electron in a higher energy state falling to fill the hole with the emission of a photon of energy less than that of the initially incident X-ray photon. Close to an absorption edge, these fluorescent background radiations can become large, dominating the scattered intensity signal, it is therefore advisable to choose X-ray wavelengths some distance from any elemental absorption edge associated with the sample.

Another problem which occurs when close to an absorption edge is the variation in the atomic scattering form factor, due to the frequency dependent dispersion corrections, a phenomenon used to more positive effect in the performance of Anomalous X-ray Scattering experiments [67].

An example background taken for a simple tape widowed, sample cell, is shown in Figure 27 and the results of subtracting this from the data shown in Figure 26 are presented in Figure 28.

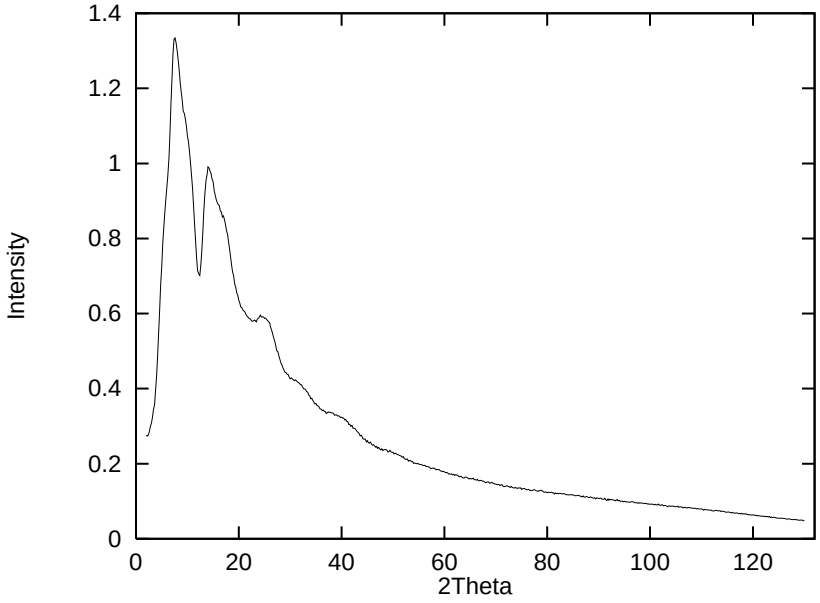

Figure 28: Background corrected diffraction data set

6.1.5 Scattering volume correction

It is necessary to account for the variations in the volume of sample illuminated by the incident X-ray beam as the sample is rotated during an experimental scan. Assuming a flat parallel sided sample for simplicity, the intensity corrected for sample rotation can be calculated using the relation:

$$I_c = \frac{I_{bc} \cos\theta}{t} \tag{81}$$

I_c being the corrected intensity, θ the sample orientation angle and t the thickness of the sample. This correction may not be necessary if the sample container's symmetry is such that there is no change in scattering volume with scattering angle e.g. a cylinder oriented with its axis on the diffractometer axis of rotation. The form of the multiplicative volume variation correction is shown in Figurevolcor.

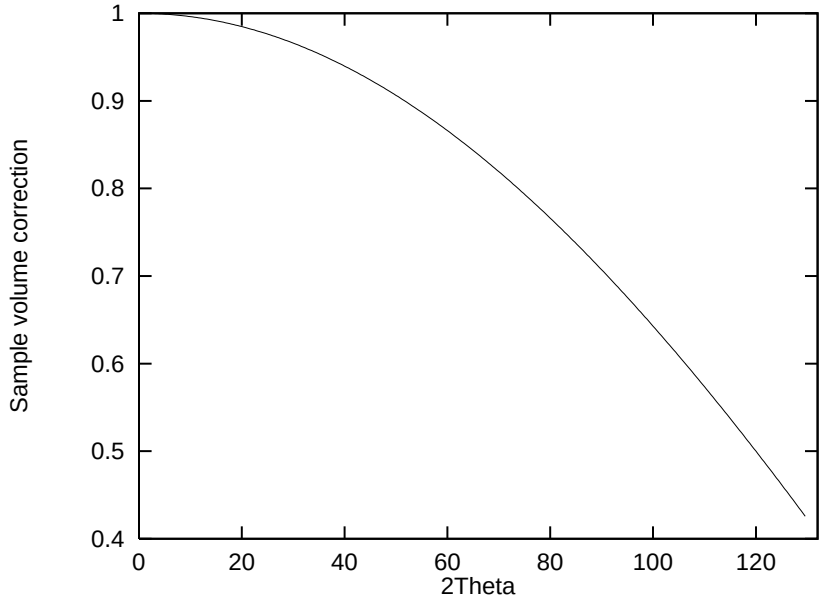

Figure 29: Form of the multiplicative sample volume variation correction

6.1.6 Compton scattering

Following the sample and instrumentation corrections, the wavelength dependent corrections have to be applied, these being the Compton scattering and absorption corrections. The application of these corrections to the data is best performed in conjunction with the final scaling to an absolute measure since there are several constants involved which can be tricky to determine accurately. This scaling will be discussed after the Compton absorption corrections have been introduced.

Compton scattering is that resulting from inelastic interactions between the X-ray photons and the electrons in the sample. It is most significant when scattering occurs from samples containing elements with low atomic numbers. This incoherent contribution to the scattering intensity can be accounted for either theoretically or experimentally [68, 69]. The theoretical approach is based upon calculating a model spectrum for the incoherent scattering from the sample and subtracting this model

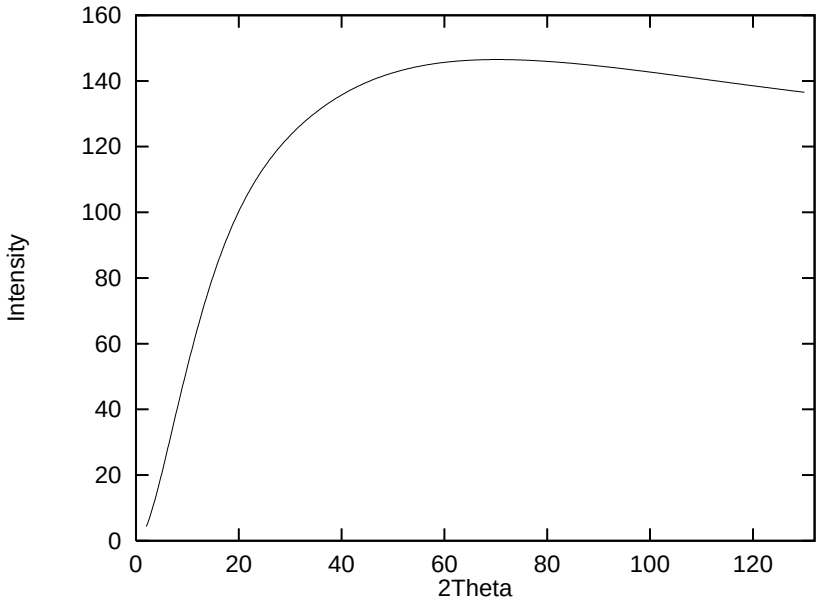

Figure 30: A typical Compton profile.

from the instrumentation and sample corrected intensity. This approach will be discussed here, but it should be noted that the experimental technique produces a better correction if its performance is possible [69]. A typical Compton scattering profile is shown in Figure 30.

Before the incoherent scattering contribution can be evaluated, it is necessary to calculate the atomic form factors for the various atom types in the system [70]. This can be done using the following parameterised, empirical equations:

$$f(\sin(\phi/2),\lambda) = \sum_{i=1}^{4} a_i \exp(-b_i(\sin(\phi/2)/\lambda)^2) + c \tag{82}$$

where the values of the fit constants a_i,b_i and c can be found in [71]. The Compton contribution can then be approximated using:

$$I_{inc} = \sum_i \left[Z_i - \frac{f_i^2(\sin(\phi/2)/\lambda)}{Z_i} \right] \times [1 - M_i(\exp\{-K_i s\} - \exp\{-L_i s\})] \tag{83}$$

where $s = \sin(\phi/2)/\lambda$, Z_i is the atomic number of atom i in the scattering unit and M_i,K_i and L_i are the tabulated fit constants for atom i [72, 73] which fit the

theoretical Compton scattering profile. The incoherent contribution i.e. Compton scattering component to the scattering intensity, is subtracted from the corrected intensity, i.e. polarization, background corrected etc. to yield the coherent scattering intensity function:

$$I_{coh} = I_c - I_{inc} \tag{84}$$

This correction is often performed with a multiplicative constant applied to I_{inc} to account for the fact that the theoretically calculated Compton profile is only an approximation to the actual inelastic processes involved in the sample. It is assumed that the general shape of the correction is correct but slight variation in overall amplitude may be needed i.e.:

$$I_{coh} = I_c - CI_{inc} \tag{85}$$

The Compton scattering will undergo some measure of absorption within the sample and therefore should be absorption corrected, however, this is in no way a simple task theoretically, and is one of the main reasons that experimental determination of the Compton scattering contribution is more reliable.

6.1.7 Absorption correction

It is necessary to account for the attenuation of the X-ray beam as it passes through the sample. The amount of absorption is determined by the path length of the X-rays through the sample and the sample's absorption coefficient. The correction is applied in the form of a multiplicative constant which takes the form:

$$R(\theta,\phi) = \frac{1}{\mu t}\left\{\frac{\cos(\phi-\theta)\cos\theta}{\cos(\phi-\theta)-\cos\theta}\right\}\left[\exp\left\{\frac{-\mu t}{\cos(\phi-\theta)}\right\} - \exp\left\{\frac{-\mu t}{\cos\theta}\right\}\right] \tag{86}$$

for a flat parallel sided sample, where μ is the linear absorption coefficient for the sample, t is the sample thickness, ϕ is the scattering angle and θ the angle of the

sample to the beam. The correction can now be represented as:

$$I_{ab} = R(\theta, \phi) I_{coh} \equiv R(\theta, \phi)(I_c - C I_{inc}) \tag{87}$$

The derivation of the required correction is much simplified if the $\theta/2\theta$ geometry is used [49]. In this case, equation (86) is not applicable since if $\phi = 2\theta$, $R(\theta, \phi)$ becomes zero. However, a simpler constant can be defined to account for the reduction in intensity caused by absorption, giving a correction of the form:

$$I_{ab} = I_{coh} \exp\{\mu t / \cos\theta\} \equiv (I_c - C I_{inc}) \exp\{\mu t / \cos\theta\} \tag{88}$$

The values for μ and μ/ρ can be obtained in tabulated form in various sources, e.g. [54] for most elements, and over a range of wavelengths. The absorption coefficient for a compound or alloy sample is found using the relation:

$$\mu = \frac{1}{V} \sum_i n_i (\mu_a)_i \tag{89}$$

where μ is the absorption coefficient, n_i is the number of atoms of type i in the volume V and, μ_a is the atomic cross section for absorption of the element i, defined by:

$$(\mu_a)_i = (\mu/\rho)_i (A/N) \tag{90}$$

where $(\mu/\rho)_i$ is the mass absorption coefficient for element i, A is the atomic mass number for element i and N is the Avogadro number. If there is any doubt, an experimentally measured value for the sample's absorption should be obtained.

Applying this correction to both the coherent and incoherent contributions to the scattering in the form shown above is, again, only an approximation since the Compton scattering has a distribution to longer wavelengths than the elastically scattered photons, giving it slightly different absorption properties. Also, the incoherent scattering is generated within the sample itself and so the actual pathlength seen by the inelastically scattered photons is difficult to determine accurately. The form of a typical multiplicative absorption correction is shown in Figure 31.

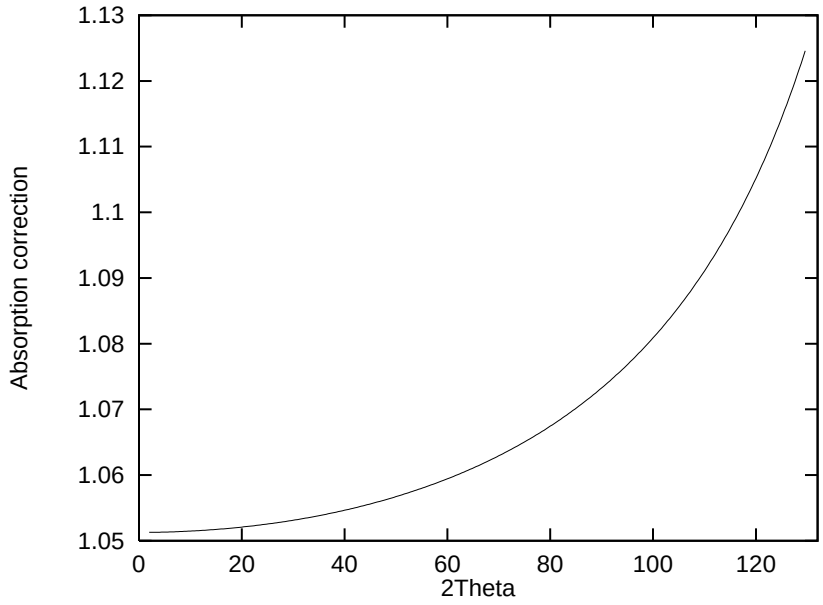

Figure 31: Form of the multiplicative absorption correction

6.1.8 Atomic Self Scattering

The calculation of the self or independent scattering contribution, i.e. the scattering from electron distributions of individual atoms within the sample, again requires some knowledge of the chemical composition of the sample.

This contribution $S_s(\phi)$, (for example see Figure 32) can be calculated from the sum of the squares of the atomic scattering factors of each atom (calculated previously for the evaluation of the Compton scattering contribution) in the unit of composition i.e.:

$$S_s(\phi, \lambda) = \sum_i f_i^2(\sin(\phi/2)/\lambda) \tag{91}$$

Once this has been calculated, the structure factor for the sample can be obtained by scaling the corrected experimental intensity so that it oscillates about the self scattering function. The two should be coincident at high scattering vectors and fairly even oscillations of the intensity about $S_s(\phi)$ are expected at lower scattering

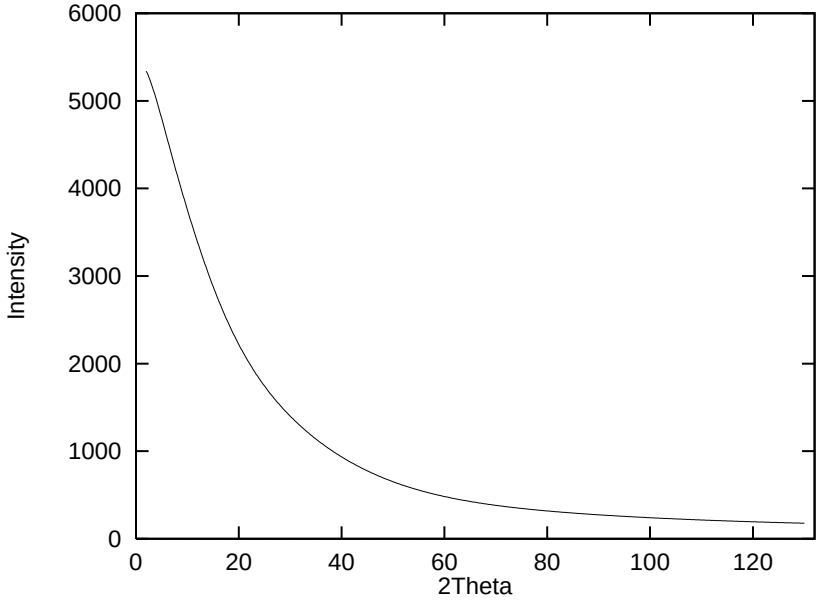

Figure 32: An example independent scattering profile

vectors. This scaling of the data, so that it oscillates evenly about the independent scattering, effectively normalizes the scattering to that from one unit of composition. The process leads to a simplification of equation (34) in that N, the number of scattering units, is now equal to unity. Once this scaling has been performed the self scattering contribution to the intensity function can be subtracted and the function normalized completely i.e.:

$$i(\phi,\lambda) = \frac{(I_{ab})_{scaled} - S_s(\phi,\lambda)}{f_e^2} \tag{92}$$

where $(I_{ab})_{scaled}$ is:

$$(I_{ab})_{scaled} = D(I_{coh}\exp\{\mu t/\cos\theta\}) \equiv D((I_c - CI_{inc})\exp\{\mu t/\cos\theta\}) \tag{93}$$

C and D being the scaling constants for the incoherent and coherent scattering contributions respectively. An example interference function $i(\phi,\lambda)$ is shown in Figure 33.

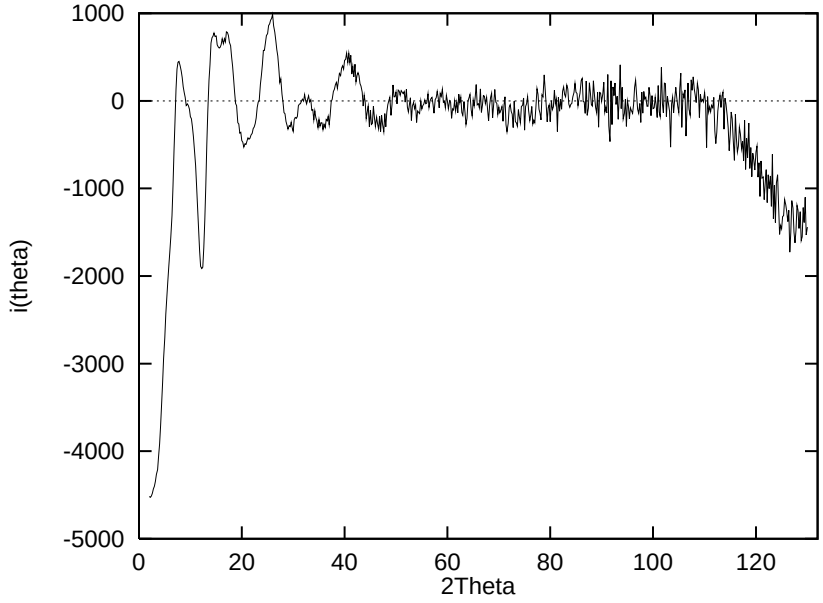

Figure 33: An example of an interference function $i(\phi, \lambda)$

As mentioned earlier, applying the absorption correction to the Compton scattering in this manner, is not ideal. Superior fitting results can be obtained by allowing the magnitude of the absorption correction to the Compton profile to differ from that applied to the data, such as:

$$(I_{ab})_{scaled} = D((I_c \exp\{\mu t/\cos\theta\}) - C(I_{inc} \exp\{\mu^* t/\cos\theta\})) \tag{94}$$

where μ^* is a parameter estimated for the absorption experienced by the incoherent component of the scattering.

The difference function in equation 92 is divided by f_e^2, Figure 34, i.e. the square of the average electron scattering factor as introduced in equation (26), this is termed a sharpening factor, introduced as $g(k)$ in equation (34). The main criteria for their choice is that they decrease with increasing $\mathbf{k}$.

These last steps in the data correction process i.e. the Compton scattering correction, the absorption correction and the scaling to the scattering form factors, are

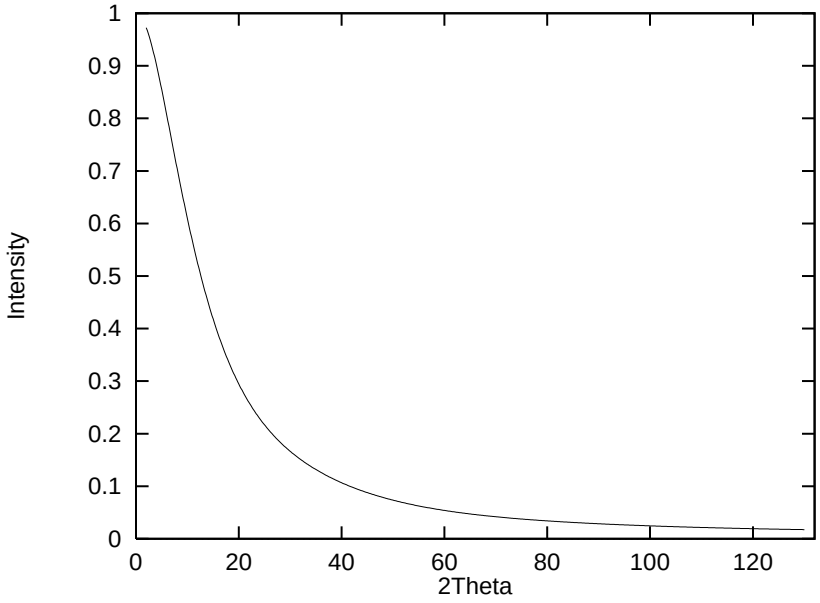

Figure 34: A typical sharpening function f_e^2

not straightforward corrections. Good results can usually be obtained by iterating, within constraints, the magnitudes of each correction applied to the data until a good fit to the independent scattering curve is obtained i.e. iterating using the values of the constants C and D and the magnitude of the product μt in the absorption correction term. The result of applying the Compton, Absorption and scaling corrections to an experimental data set are shown in Figure 35.

Another method for scaling experimental X-ray intensities to an absolute scale has been presented by Krogh-Moe [74] and Norman [75], their technique being useful if oscillations in the structure factor persist out to higher values of $\mathbf{k}$ than are experimentally accessible. The method which they present is based on the evaluation of a scaling constant calculated from the value of the electron distribution function at $\mathbf{r}$=0. Again, care must be taken to correct both the coherent and incoherent scattering contributions for absorption within the sample. The method can be summarized by the following equation where α is the scaling constant to be determined, i.e. the

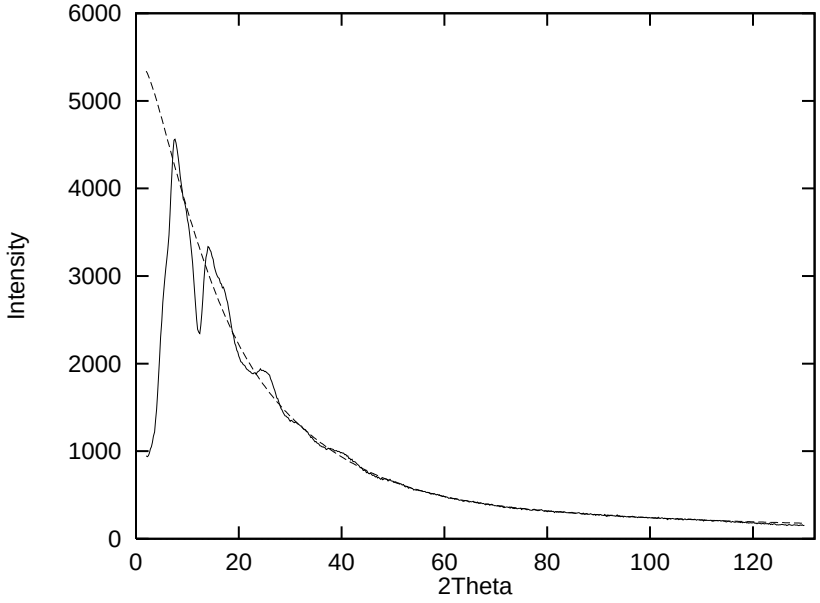

Figure 35: Corrected diffraction data set scaled to oscillate about its self scattering profile

factor by which the experimental intensity curve must be multiplied if it is to oscillate about the sum of the atomic self scattering and Compton contribution:

$$-2\pi^2\rho_0^2\frac{V}{N} = \alpha\int_0^\infty k^2 I_e(k)dk - \int_0^\infty \left(\sum_{uc} f_i^2(k) + I_{inc}(k)\right)k^2 dk \qquad (95)$$

Where ρ_0 is the electron density of the sample, $\frac{V}{N}$ is the reciprocal of the scattering unit density, I_e is the absorption corrected experimental intensity prior to any corrections for the Compton component I_{inc}.

6.1.9 Binning of Data to k-space

This is the last step in the preprocessing of the X-ray diffraction data, performed by transforming the data from a function of angle to being a function of the scattering vector **k** as defined in equation (15). This step is best performed after the Compton scattering correction so as to avoid binning the Compton events to higher values of k

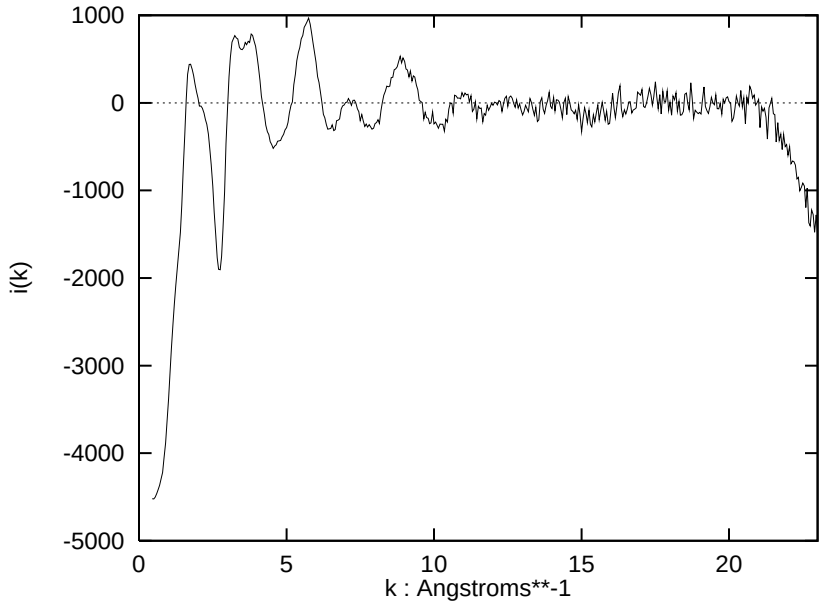

Figure 36: A k-binned interference function i(k)

than they should be associated with, since incoherent scattering shifts the scattered photons to longer wavelengths. The data should be binned so as to be evenly spaced in k, i.e. weighted contributions of the angular distribution, averaged and assigned to each evenly spaced k-value. This has the effect of improving the statistical accuracy of the data at high k, due to the larger number of angular points contributing to each k-space bin. Once this has been done, the data may be Fourier transformed to one of the various radial distribution functions for final analysis, (the extraction of interatomic distances and coordination numbers) and interpretation. An illustration of an isolated interference function binned to a function of **k** is shown in figure 36.

6.1.10 Extraction of structural information

Once all the data correction stages have been performed and an interference function i(**k**) been isolated, it is then possible to proceed with the steps necessary for extraction

of structural information relating to the sample, i.e. inter-atomic correlation lengths and coordination numbers. This is usually performed via Fourier inversion of the interference function, to obtain a $t(r)$ i.e. an electron density (in the case of X-rays) distribution function, essentially $t(r)$ is defined by equation 63 i.e.

$$t(r) = 2\pi^2 r\rho_e \sum_{uc} Z_j + \int_0^{k_m} ki(k)W(k)\sin krdk \tag{96}$$

which is equivalent to:

$$t(r) = \sum_{uc}\sum_{i} \frac{N_{ij}}{r_{ij}} P_{ij}(r) \tag{97}$$

all the above terms being as earlier defined. The choice of window function $W(k)$ applied to the data, is somewhat dependent upon the data quality of the interference function. In this work the window function applied to the data is [55] :

$$W(k) = \begin{cases} 1 - 3\left(k/k_{max}\right)^2 & |k| < k_{max}/3 \\ 3/2\left(1 - 2\left|k/k_{max}\right| + \left(k/k_{max}\right)^2\right) & k_{max}/3 < |k| < k_{max} \\ 0 & |k| > k_{max} \end{cases}$$

It is important to note that the window function applied to the the data in equation 96 is the same as that used when calculating P_{ij} in equation 97. P_{ij} being defined by equation 60 i.e.:

$$P_{ij}(r) = \int_0^{\infty} \frac{f_j f_i}{g^2(k)} W(k)\sin kr_{ij}\sin krdk \tag{98}$$

Similarly, the sharpening function $g^2(k)$ must be the same function as used when calculating the initial $i(\mathbf{k})$, in this work the scattering form factor for a single electron f_e^2.

The simplest use of equations 96 and 97 is demonstrated in [5]. Once a $t(r)$ has been obtained, the positions and areas of the peaks are determined by fitting a series of gaussian curves to the data, this performed using a standard χ^2 test. The fitting being performed by iterating the heights, widths and position of each gaussian curve,

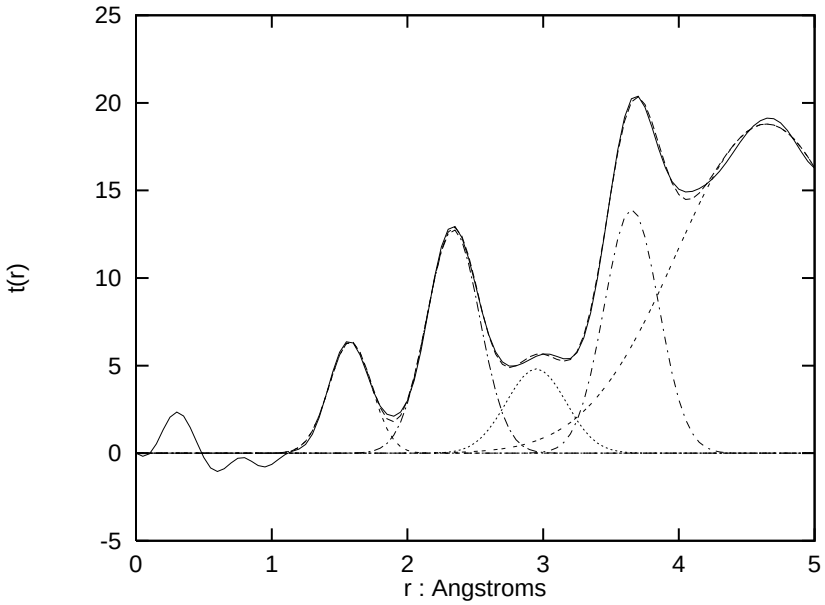

Figure 37: Example of $t(r)$ fitted with gaussian profiles

Figure 37. Once the inter-atomic correlation distances have been determined by the positions of the fitted gaussians, the areas of the gaussian curves can be compared with the areas of the pair functions P_{ij}, this comparison of areas allowing the approximate determination of coordination numbers N_{ij}.

This process must be considered very approximate, since determination of the areas of the various P_{ij} calculated at their various r_{ij} suffers greatly from uncertainty as to the extent that the magnitude of the pair function area is contained in the Fourier *wings* to the transformed function, equation 98 essentially being a Fourier transform. The application of the window function $W(k)$ does little to help with this problem, although is suppresses a significant proportion of the transform *ripple*. Another factor that can have serious impact upon area i.e. coordination number determination is the lack of independence of the peak features in $t(r)$, since the fitting process cannot exclusively determine the weighting parameters to be assigned to each gaussian at its given distance r_{ij}. Where these problems arise, only other information determined

from by other means can help clarify whether the evaluated numbers are physically acceptable.

All these points, both for peak positions determined from the gaussians as well as their associated peak areas, must be viewed in the light of the composite nature of $t(r)$, i.e. that all atom pair correlations are presented, weighted by their respective scattering strengths f_i. Thus, without resort to methods such as anomalous X-ray scattering where the variation in the scattering factors f_i near an atomic absorption edge can be used to advantage, partial contributions to $t(r)$ from specific atom type pairings, cannot be determined.

6.2 EXAFS

The initial treatment of EXAFS data are the steps involved in isolating and normalizing the oscillatory signal evident in the absorption spectrum on the high energy side of an absorption edge. The experimental spectra are usually taken over energies ranging from one or two hundred eV below an absorption edge to several hundreds of eV above, sample permitting, (i.e. limited by the presence of further absorption edges in the energy range a few hundred eVs beyond a given edge).

The overall analysis procedure can be broken down into six main steps [59], these being:

1. Energy scale calibration,

2. Removal of glitches within the data set,

3. Pre-edge background removal,

4. Post-edge background fitting and removal,

5. Normalization,

6. Extraction of structural information.

6.2.1 Energy scale calibration

This step is necessary to account for misalignment of the monochromator, it is generally performed by using a calibrant sample, i.e. a sample containing the element of interest but in a known chemical environment. Once a scan of the calibrant has been performed, the scans taken from the "unknown" sample, can be aligned so that some feature of the near edge spectrum coincides with a known feature in the calibrant's spectrum. Typically, a metal foil may be used as the calibrant but slight errors here tend not to have too great an effect on the EXAFS spectrum since the energies of interest tend to begin approximately 50eV above the actual edge. In the final fitting of the data to extract structural information, there is generally a constant that may be varied to account for uncertainties in the edge position.

6.2.2 Glitch removal

Imperfections in the monochromator crystal often cause the appearance of relatively large sharp structure on the EXAFS signal. These sharp features may cause problems in the later data analysis stages. It is therefore often desirable to remove these sharp features from the spectrum, replacing them with points interpolated from the EXAFS function on either side of the affected region.

6.2.3 Pre-edge background removal

This step is to remove the contribution to the absorption spectrum from lower energy absorption edges and Compton scattering etc.. It may be performed by various techniques, e.g. the fitting of the "Victoreen" expression to the pre-edge region of the data and extrapolating over the total energy range, this expression being:

$$C_1\lambda^3 - C_2\lambda^4 \tag{99}$$

where C_1 and C_2 are constants determined during the fitting process and λ is the X-ray wavelength.

However, it is usually sufficient simply to fit a linear function of the form $Y = mX + C$ to the pre-edge data, and extrapolate this over the complete energy range. This pre-edge background is then subtracted from the raw spectrum to remove the lower energy contributions.

6.2.4 Post-edge fitting, background removal and normalization

This is potentially the most difficult step in the preliminary EXAFS analysis. It equates to determining a background absorption for the edge, termed μ_0. The equation governing this step is:

$$\chi(E) = \frac{\mu(E) - \mu_0(E)}{\mu_0(E)} \tag{100}$$

The evaluation of the background absorption allows the isolation of the EXAFS signal, and as such is a highly critical point in the data analysis. Failure to produce a satisfactory background leads to the presence of non-physical trends in the spectrum to be analysed. Recently the problem of double electron excitation effects on the

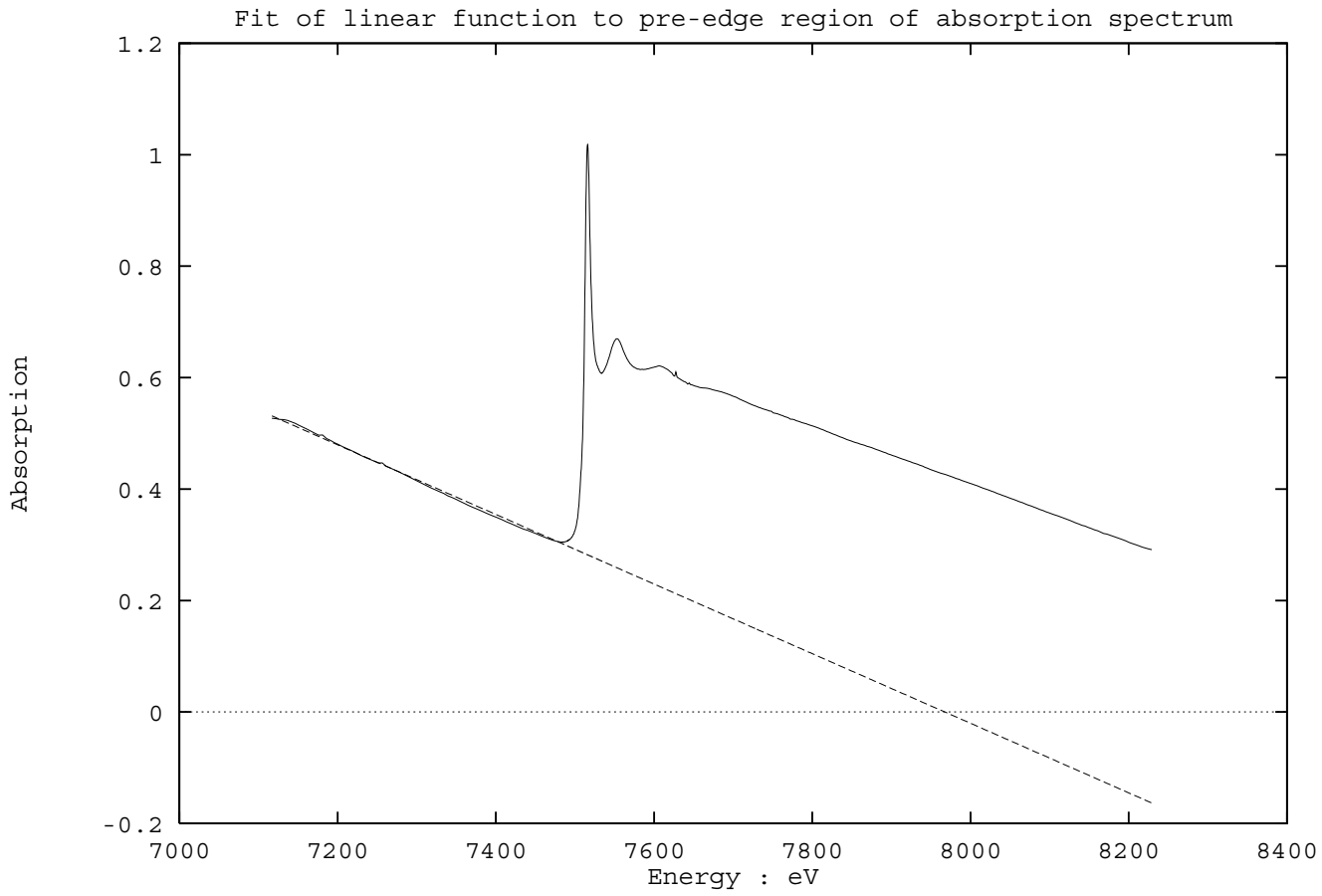

Figure 38: Fitting of a linear function to the EXAFS spectrum pre-edge

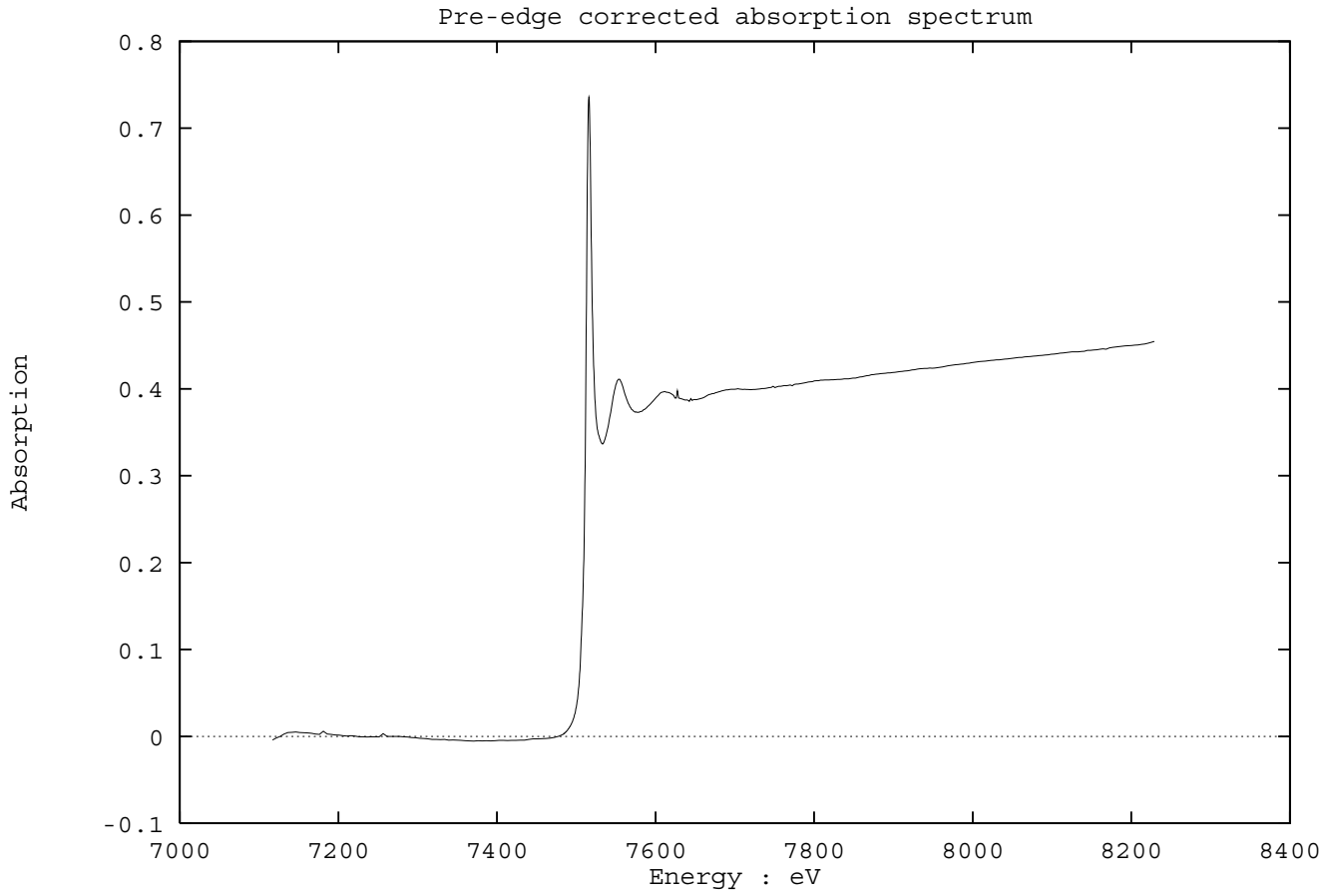

Figure 39: Pre-edge corrected EXAFS spectra

background absorption profile have been considered [76, 77, 78]. This phenomenon results in discontinuities in the absorption background, a serious problem when the post-edge region is fitted by a smooth polynomial or spline function. Failure to account for these effects usually results in low frequency contaminants to the spectra; requiring removal via some kind of filtering procedure. This problem is particularly serious for elements such as the Lanthanides, which have large numbers of electrons increasing the probability that an electron energy state transition is available for excitation.

Many methods have been proposed to perform this task, ranging from the use of low order polynomials to fit the post-edge region, ignoring the EXAFS oscillations, the fitting of a series of cubic splines to the post-edge region, or the use of smoothing routines to produce an estimate of the background absorption. No technique is ideal, and often several attempts are required before a suitable function is obtained, e.g. Figure 40. Once this is achieved it is a simple process to background correct the data and normalize, i.e. by application of equation (100).

6.2.5 Extraction of structural information

In this work, this final stage of EXAFS analysis has been performed using EXCURV90 [79]. A program written to analyse EXAFS data in terms of the fast curved wave theory developed by Gurman et al. [63], or the small atom approximation [62]. Both these techniques being developed to determine the function $\chi(k)$ as defined by equation 100. A discussion of this final data analysis procedure , which is essentially a curve fitting process, minimising experimental parameters to isolate physical information, can be found in [80].

EXCURV90 [79], makes use of statistical significance tests developed by Joyner et

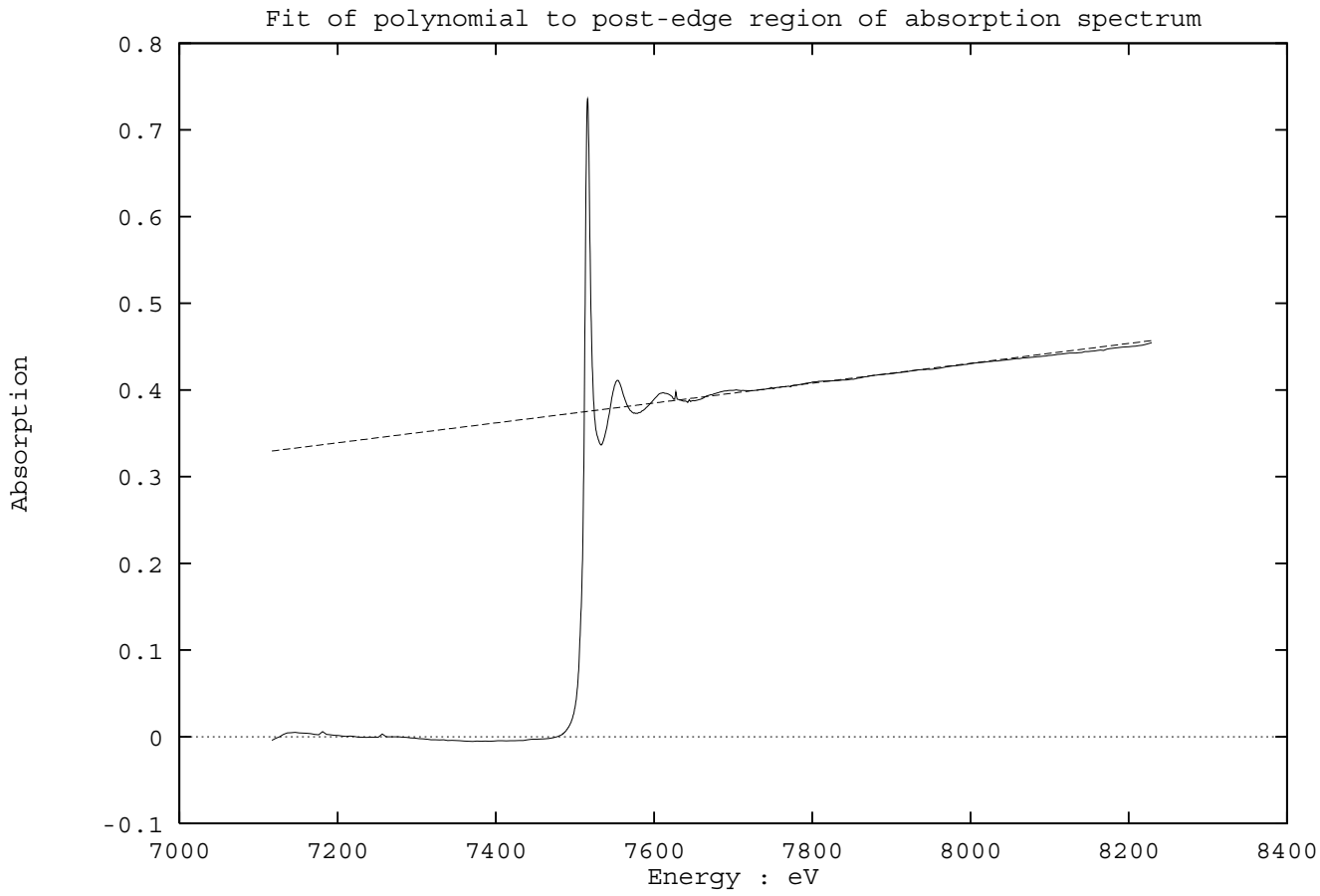

Figure 40: The fitting of a polynomial post-edge background model

al. [81] to evaluate fit parameters. These parameters are illustrated in the plane wave approximation by $A(k)$, λ, R_i, N_i, and σ^2 i.e. the terms described earlier (chapter 4) as the *amplitude reduction factor*, the *mean free path* of the freed electron, the *distance* from the X-ray absorbing atom to the atom i, the *coordination number* associated with the shell of atom i and finally the *structural* and *thermal disorder* parameter. As an aid to determining fit parameters, correlation maps can be calculated between related parameters (Figure 41), for example between N_I and σ or between R_i and an energy offset parameter (phaseshift) E_0.

The atom type specificity of the technique, arising from the atom type dependence of the phaseshift induced in the propagating electron wave, allows the isolation of a pair distribution function (p.d.f) rather than the more general $t(r)$ extracted from conventional X-ray diffraction techniques. These phaseshifts are calculated theoretically within EXCURV90 [79] and are in general, a reliable measure of the atom types present, provided that the sample constituent elements are sufficiently separated in the periodic table, to have significantly different atomic potentials.

Various data weighting schemes are possible in the final analysis stages, typically the data is said to be k,k^2 or k^3 weighted; a process that increases the significance of the data at higher energies above the edge where the signal is weakest. This procedure suppresses the $\frac{1}{k}$ dependence of the EXAFS signal and also suppresses the near edge structure in the low energy region of the signal, where most of the contributions to the signal arise from complex multiple scattering phenomena within the sample. Often it proves useful when fitting an EXAFS spectrum to work through the weighting schemes from low to high, improving the data refinement at each stage, this process allowing emphasis to be applied systematically to the various regions of the spectrum.

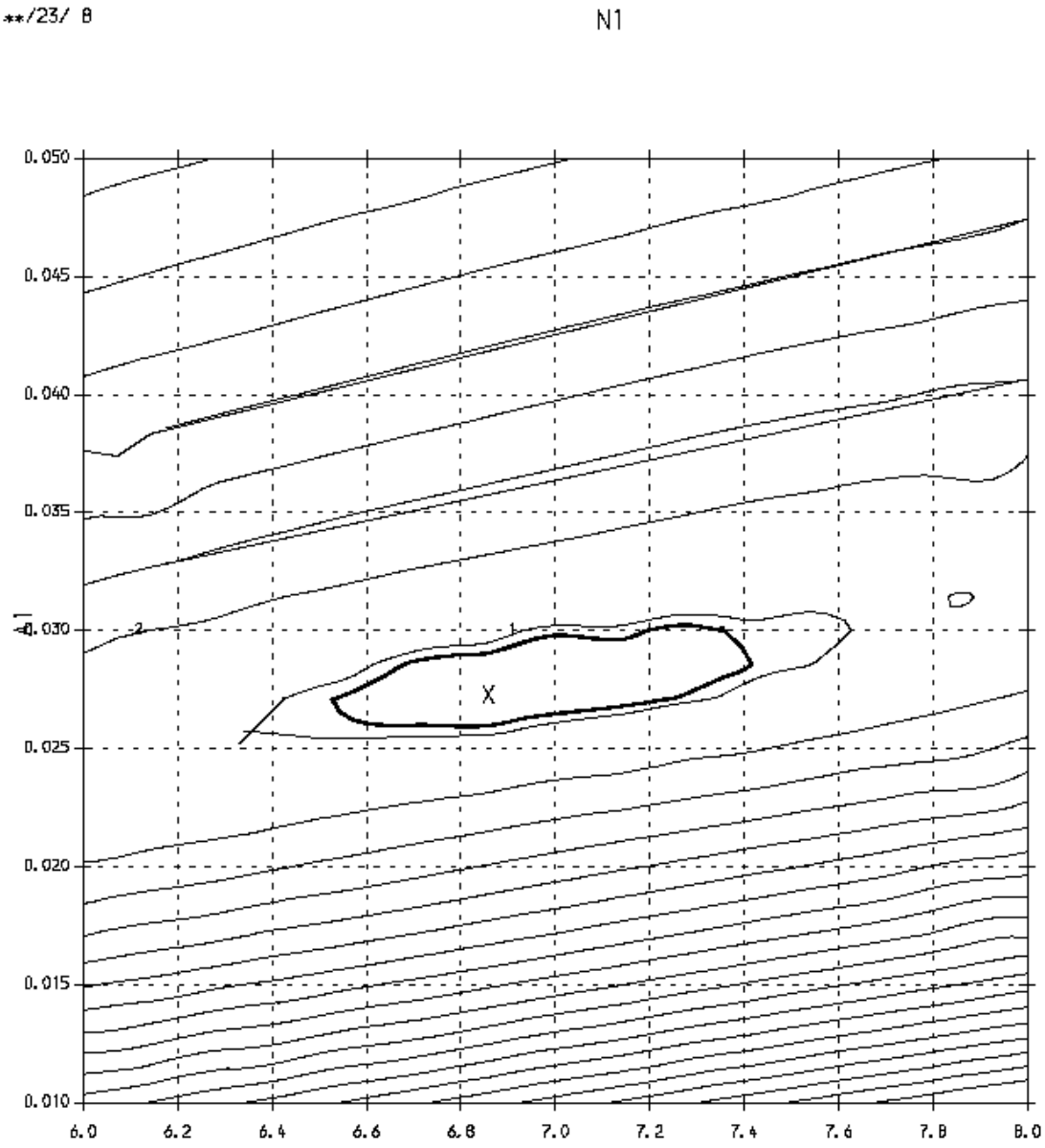

Figure 41: Example correlation map, showing the relationship between N and A ($A = 2\sigma^2$); the five percent statistical certainty is shown by the bold contour

Chapter 7

Samples

The samples which have been studied in this work fall into two categories:

- Rare earth doped silicate glass optical fibre preforms, supplied by *Pirelli Cables Ltd.* [1] and
- Rare earth doped phosphate glasses, supplied by Saunders [2]

7.1 Fibre preform samples

The fibre preform samples supplied by *Pirelli Cables Ltd.* contain very small amounts of rare earth dopants in a silica matrix, in some cases containing GeO_2 or Al_2O_3 co-dopants. The fibre preforms were prepared using the Modified Chemical Vapour Deposition technique (MCVD) and solution doped with rare earth chlorides. The initially supplied samples consisted of small pieces of preform which were sliced from

[1] Dr. E.Tarbox, Pirelli Cables Ltd. P.O.Box 6, Leigh Road, Eastleigh, Hants, SO5 5YE

[2] Professor G.Saunders, School of Physics, The University of Bath, Claverton Down, Bath, BA2 7AY

the bulk preform using a diamond saw. These systems proved to be extremely challenging to study since not only were the rare earths present in very low concentrations typically < 4 weight percent, but the sample volume was also extremely small for the diffraction and EXAFS techniques. The aim was to obtain if possible, spatially resolved structural information on the distribution of rare earth across the core region of the preform, and how this concentration distribution modified the atomic sites occupied. The core region of a fibre preform has a typical dimension of approximately 1mm in diameter, see Figure 42.

To facilitate diffraction and EXAFS studies of these glass systems, various cross-sectional slices were taken of the raw cylindrical fibre preforms. Those used for EXAFS being transverse slices, ground and polished to 100 microns thickness, as well as thicker slices probed in the fluorescence geometry. The X-ray beam dimensions chosen for the EXAFS experiments were small circular spots collimated using a pinhole mechanism to a range of sizes, these being 100 microns, 500 microns and 1mm diameter. A motorised stage for both the samples and collimating pinholes was available on station 8.1 at the SRS, Daresbury, allowing for the samples to be positioned to better than 100 microns accuracy so as to obtain spatially resolved data on the small sample volumes probed.

The diffraction samples were longitudinal slices through the preform, ground and polished to 200 microns thickness and mounted so as to be probed by a tall narrow X-ray beam of dimensions 100 microns by 3mm. These longitudinal slices were mounted upon aluminium plates as in Figure 42, which were then mounted upon a custom designed manipulation stage, Figure 43, which in turn was mounted upon the $\theta/2\theta$ diffractometer, station 9.1 at the SRS, Daresbury. This manipulation stage was designed so as to be able to position the preform samples in the X-ray beam

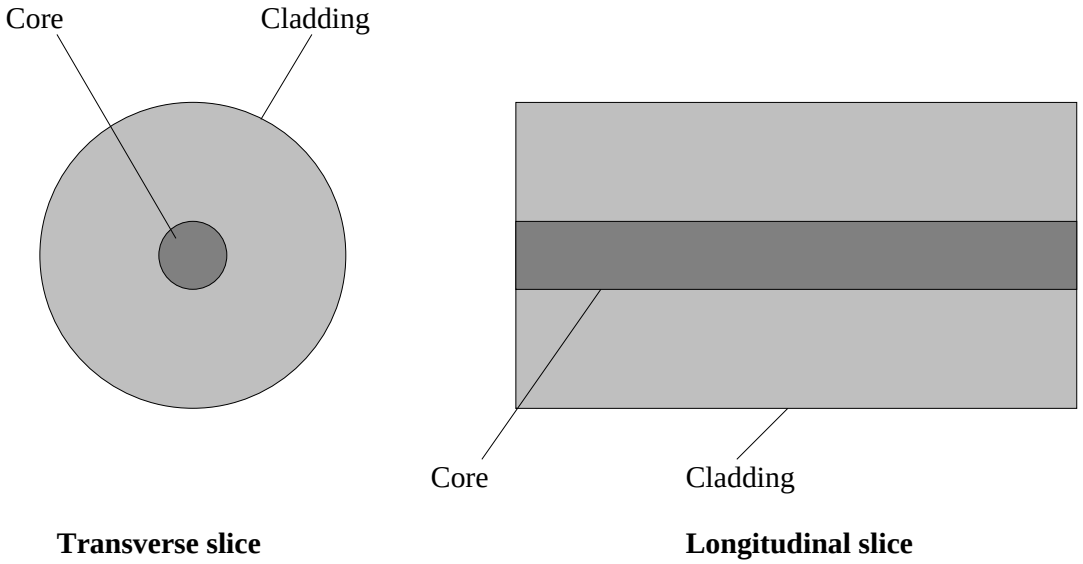

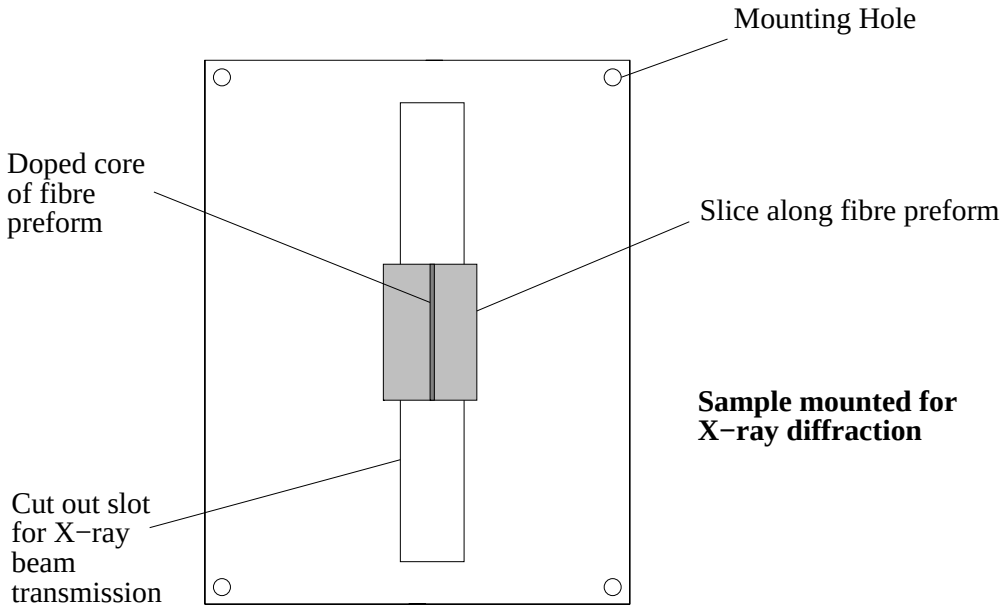

Figure 42: Figure illustrating an optical fibre preform and a longitudinal slice sample, mounted for X-ray diffraction.

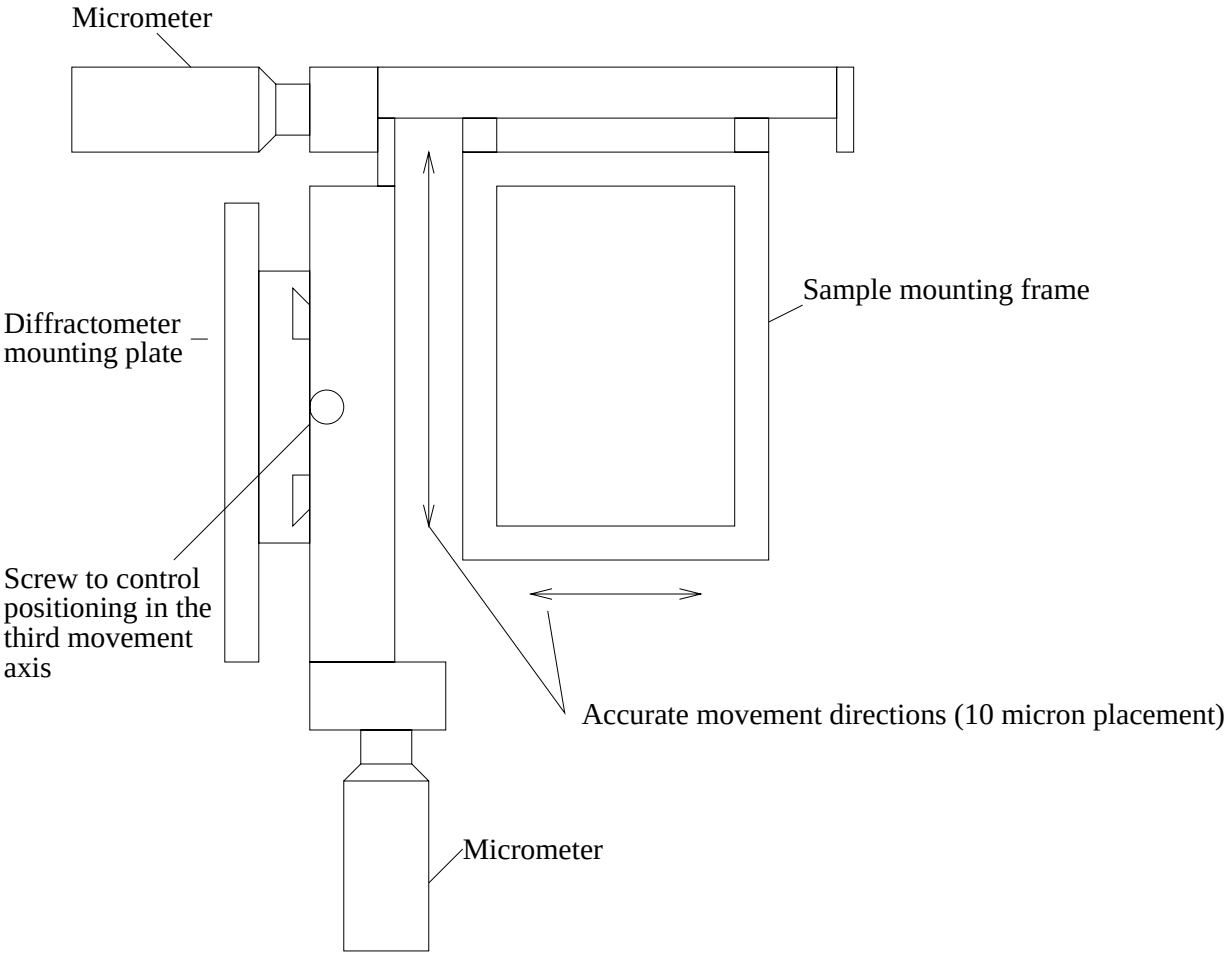

Figure 43: Custom designed XYZ positioning stage designed for use with the $\theta/2\theta$ diffractometer, station 9.1, SRS, Daresbury

with a spatial accuracy of better than 100 microns. This was achieved by the use of two micrometers, allowing the stage to be accurately positioned with respect to the incident X-ray beam.

The grinding and polishing of the samples was performed on a rotary polishing bed, using 3 micron calcined aluminium oxide powder for the initial lapping process, then 0.5 micron cerium oxide powder for the final polishing stages. These powders abraded the sample when introduced to the polishing bed via inclusion in the water lubricant. The samples were fixed to the polishing plates by use of a light candle wax, which required removal before their mounting for the X-ray experiments. This wax was removed by soaking the samples in 60/80 petroleum ether, since the wax was found to be resistant to most solvents, and the samples were too fragile for vigorous cleaning.

A table summarizing the supplied samples is given below (table 2), it should be noted that it was not possible to perform experiments on all these samples due to the many difficulties which had to be overcome, but this table is useful in that it provides an illustrative cross section of compositions typical in the manufacture of rare earth doped silicate glass for novel optical fibre devices:

Sample	Dopant	Weight %	Co-dopant 1	Weight %	Co-dopant 2	Weight %
ND165	Nd_2O_3	4	Al_2O_3	unknown	-	
ND245	Nd_2O_3	2	Al_2O_3	unknown	-	
PD47	Nd_2O_3	4	-		GeO_2	10
ND204	Er_2O_3	1	-		GeO_2	15
PD236	Er_2O_3	0.3	Al_2O_3	1	GeO_2	18
PD265	Er_2O_3	0.2	-		GeO_2	18
PD275	Er_2O_3	0.3	Al_2O_3	1	GeO_2	18

Table 2: Rare earth doped fibre preform samples

As can be seen, the weight percentage of the rare earth dopant is very small. These

concentrations being too low to have any significant effect upon interference spectra from a diffraction experiment. EXAFS was thought to be the structural probe of choice since in fluorescence mode, the technique is sensitive to atom types present in as little as a few parts per million. The diffraction experiments were performed mainly to obtain information upon the bulk silica lattice and the effects of the co-dopant atom species which are present in much larger quantities than the rare earths.

7.2 Phosphate glass samples

The production of phosphate glasses containing dopants is a very difficult task, for these samples doped with rare earth oxides, a brief outline of the method would be:

Dry starting constituent compounds, P_2O_5 and rare earth oxide, were mixed in alumina crucibles, this mixture was then heated in a furnace to temperatures of approximately $1500°C$. Once a melt had formed, it was poured into preheated steel moulds ($500°C$) and allowed to cool [21].

Various ratios of starting compounds were tried, in an attempt to produce samples doped with a range of rare earth concentrations. It has however been found by subsequent electron probe analysis that all samples tend to fall into the metaphosphate glass composition range i.e. $R(PO_3)_3$, where R is the rare earth atom type. This occurs due to the volatility of P_2O_5 which is lost during heating to form the melt, owing to the fact that the glasses consistently form in the metaphosphate regime, it is thought that this must be a stable structural state, for phosphate glasses incorporating rare earth atoms.

Phosphate glasses tend to suffer water contamination if care is not taken to keep them dry. The samples studied here, were kept in plastic containers stored in a desiccator. It has been found that rare earth doped phosphates are unusually resistant

to water contamination, and the water content of these samples has been found to be negligible [21].

Greaves et al. [26], propose that the increased chemical resistance of doped phosphate glasses can be explained using the modified random network theory; the inclusion of the dopant metal cations, shortens the phosphate chains and pins the structure thus increasing resistance to chemical attack.

Preparation of these samples for diffraction and EXAFS experiments was particularly simple. Small pieces of glass were crushed between two steel plates to produce coarse powder samples which were further ground using an agate mortar and pestle. These powdered glasses were then dusted onto sticky tape and placed in the X-ray beam. Once the samples had been powdered, they were kept dry as before, since the increased surface area to volume ratio of the powder would render them more susceptible to water contamination. When exposed to the X-ray beam, it was not thought necessary to use evacuated chambers since beam heating would dry the exposed region of the mounted sample.

The rare earth doped phosphate glass samples supplied can be summarised in the following table 3:

Sample	Dopant	Mole %	Glass density kg m^{-3}	Technique(s)
Pr	Pr_6O_{11}	21.6	3094	EXAFS Diffraction
Nd	Nd_2O_3	19.6	3233	EXAFS
Eu	Eu_2O_3	25.2	3438	EXAFS Diffraction
Gd	Gd_2O_3	22.6	3362	EXAFS
Tb	Tb_2O_3	26.3	3578	EXAFS Diffraction
Ho	Ho_2O_3	20.8	3327	EXAFS

Table 3: Rare earth doped phosphate glasses supplied

Chapter 8

Results: doped fibre preforms

8.1 Introduction

The samples studied here were manufactured using Modified Chemical Vapour Deposition (MCVD) [31], Figure 6, and solution doped with erbium ions [46]. The germanium codopant was introduced as a vapour in the initial core deposition process its main function being to raise the refractive index of the core region of the fibre preform.

This manufacturing technique leads to cylindrical symmetry of the deposited system, although radial variations in dopant atom concentration are evident; poorly formed preforms may display non-cylindrical symmetry in the core region.

In the erbium doped samples, the rare earth dopant is present in concentrations less than 1 weight percent, making EXAFS experiments extremely difficult to perform, a problem which is compounded by the small sample volumes available for structural study. Attempts at obtaining EXAFS spectra at the *Er* L_{III}-edge (8364eV) have been made, pushing current synchrotron facilities to their utmost limits, and reliable

data has proved difficult. Fluorescence spectra have been obtained from the entire core of a neodymium doped sample [82], a system with possible temperature sensor applications, but this preform core has a rare earth concentration of approximately 4 weight percent and spatially resolved studies of structure as a function of radial position were not made.

EXAFS experiments at the *Ge* K-edge (11105eV) were easier to perform, the codopant being present in quantities ranging between 15 and 18 weight percent. The spectra were measured in a conventional transmission mode. The need for high spatial resolution makes it necessary to use a small incident beam sizes this results in low photon flux at the sample.

To complement the EXAFS experiments, X-ray diffraction experiments were also performed upon some longitudinal slices of fibre preform, these having been prepared to a thickness of 200 microns and mounted upon plates suitable for the XYZ manipulation stage illustrated in figure 43. Diffraction measurements were taken at positions corresponding nominally to the centre of the core, mid-way between centre and edge and at the edge of the core. These positions were determined from absorption profiles measured at the *Ge* absorption edge.

8.2 Results and Discussion

The results of the absorption profile mapping discussed earlier, are as shown in Figures 44,45,46,47. These graphically demonstrate the correlation between the concentration profiles of the two dopant atom species erbium and germanium, the plots have been normalised such that the maximum absorption measured during a scan at a particular absorption edge is assigned a value of unity. The correlation between the concentration profiles is perhaps most clearly seen in the dip in the absorption profile at the

central core region of Sample ND204, Figure 44,45. The reduction in germanium concentration is expected in some cases due to evaporative loss of GeO_2. This loss occurs on sintering the deposited doped soot within the silica tube to form the glass that will ultimately be the preform/fibre core and also during the collapse phase. The depleted region is also visible in the erbium profile for Sample ND204, indicating that volatilization loss of Er_2O_3 also reduces the erbium concentration. Sample PD265 does not show a dip in the central core region, Figures 46,47, a fact mirrored in the Er profile for this sample. This more uniform profile was achieved by the removal of the dopant loss region by means of an etch process implemented prior to collapsing the silica tube to form the preform. In both samples, the erbium concentration profile closely tracks that of the germanium, Figures 48,49, suggesting a measure of association between the sites occupied by the dopant species. This point is interesting, since the erbium is incorporated into the preform by means of solution doping [46], whereas germanium doping is achieved by the introduction of germanium containing vapour into the MCVD silica tube as the core layers of SiO_2 soot are deposited. This would suggest that as the solution containing erbium ions is absorbed uniformly into the silica soot, it follows the germanium profile closely. A SIMS (Secondary Ion Mass Spectrometry) study of the distribution of dopant atomic species across preform and fibre cores has been performed on Er/Al and $Er/Al/P$ doped silicate glass preforms and fibres [83], the study shows a dip in the phosphorus profile as the preform was mapped, but no corresponding dip in either the erbium or aluminium profiles. This implies that erbium is more closely associated with a germanium codopant than a phosphorus dopant or that Er is bound closely with Al; Al_2O_3 does not volatilise during sintering or collapse phases.

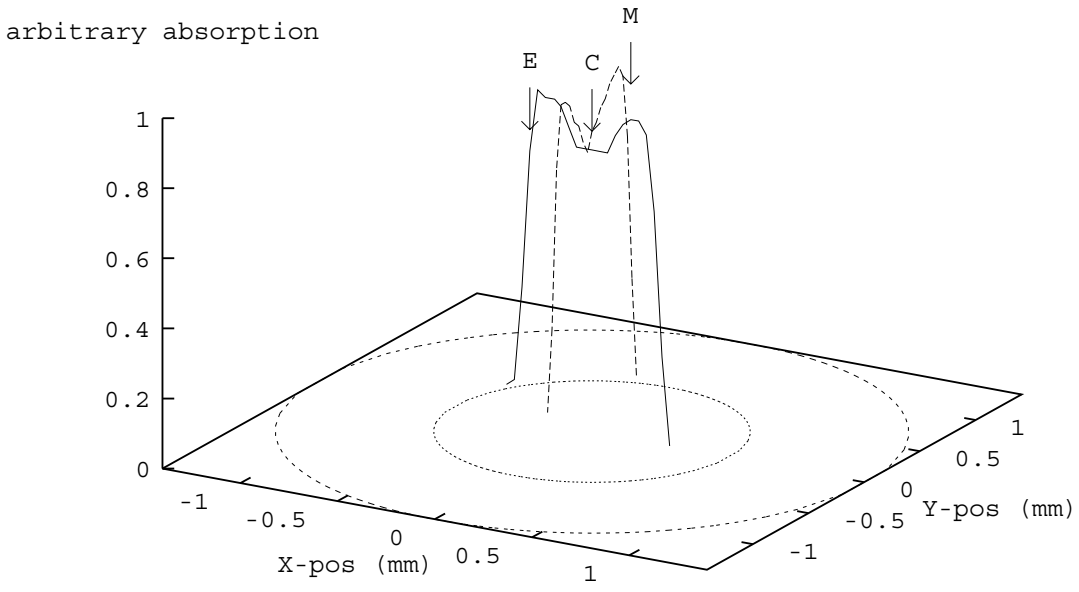

Figure 44: Absorption map of preform core at erbium edge : Sample ND204

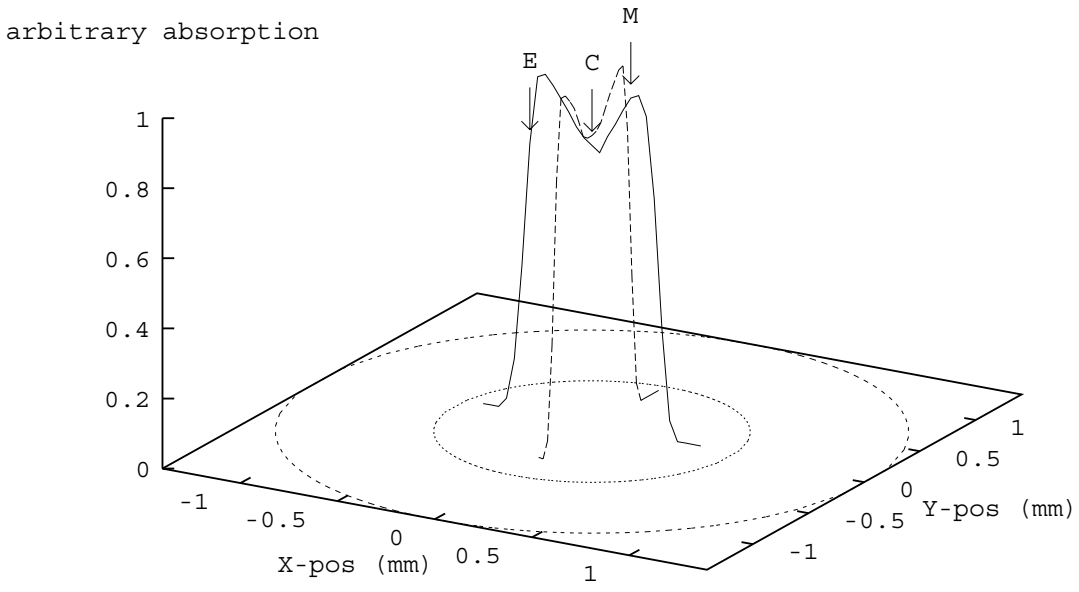

Figure 45: Absorption map of preform core at germanium edge : Sample ND204

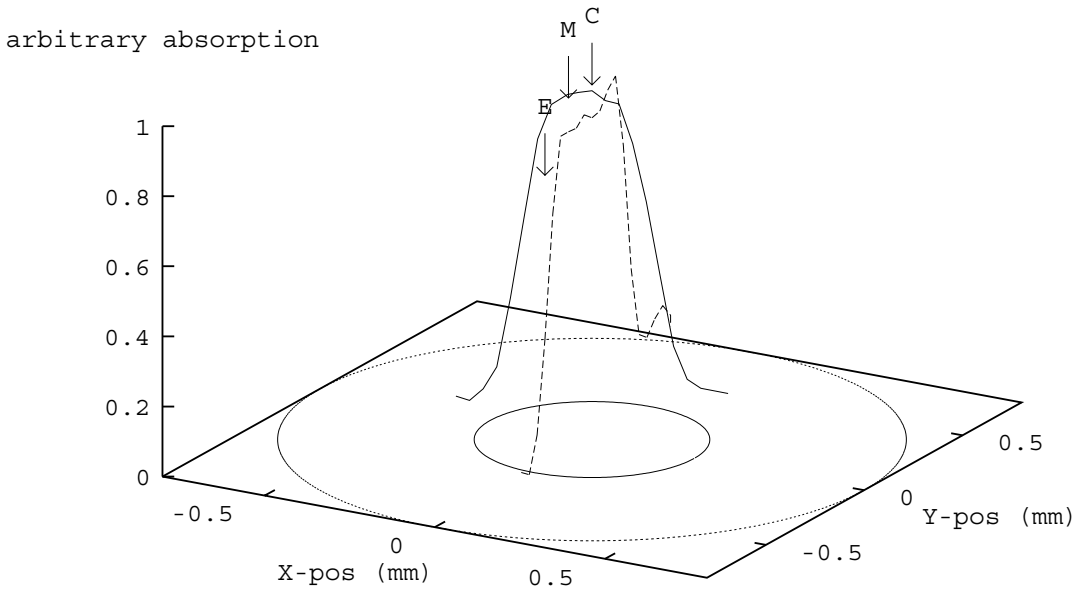

Figure 46: Absorption map of preform core at erbium edge : Sample PD265

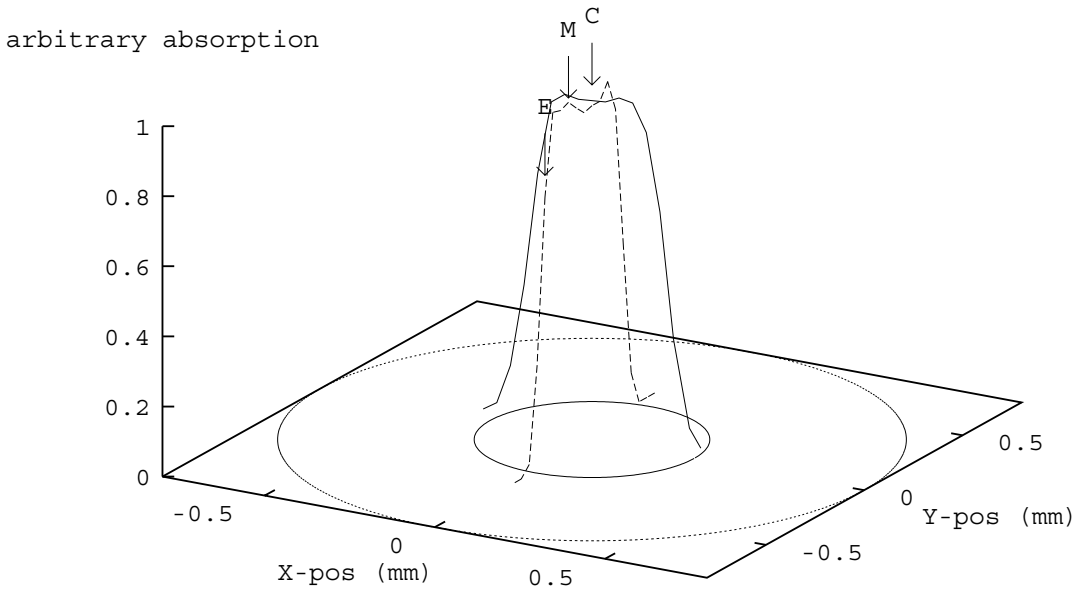

Figure 47: Absorption map of preform core at germanium edge : Sample PD265

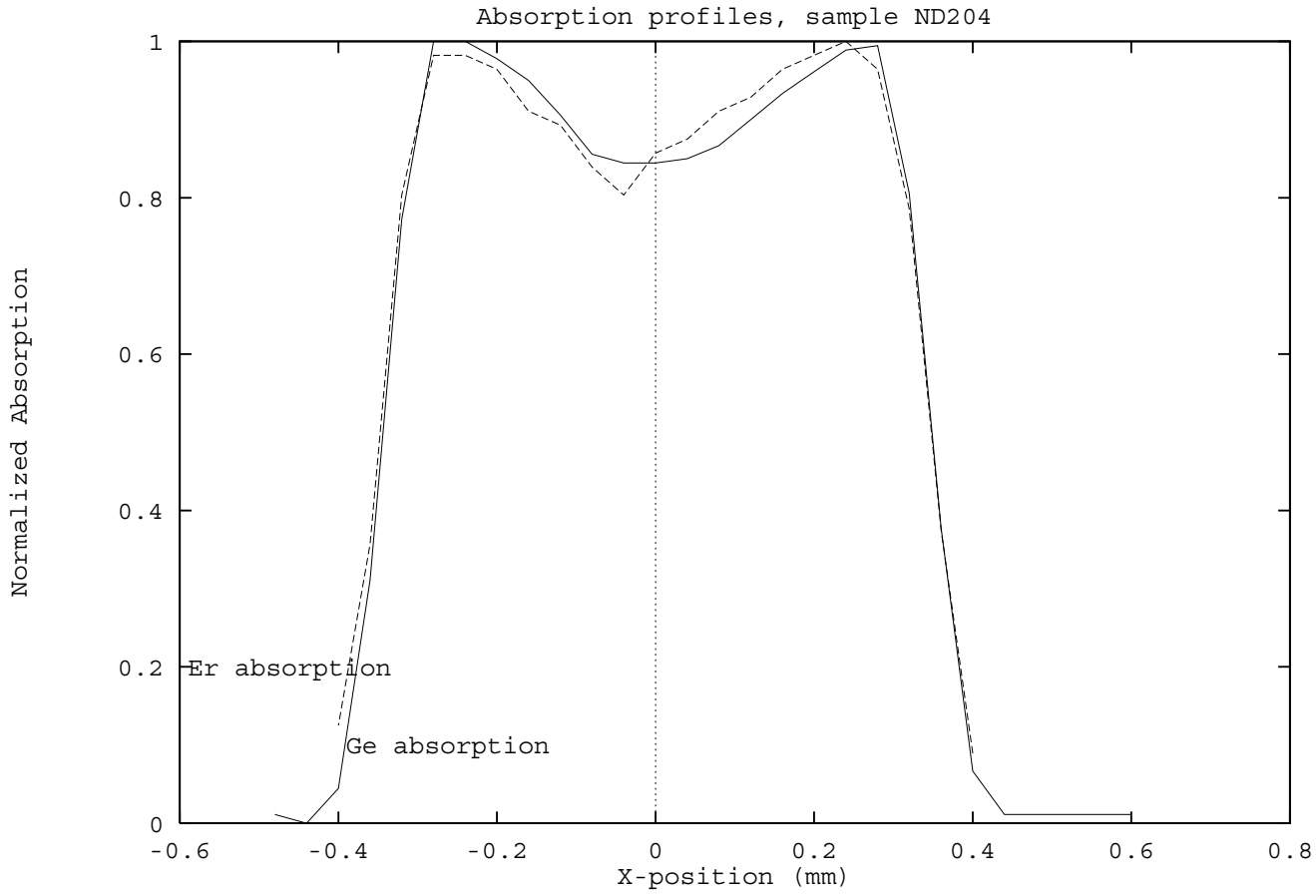

Figure 48: Absorption profile comparisons for Ge and Er scans : Sample ND204

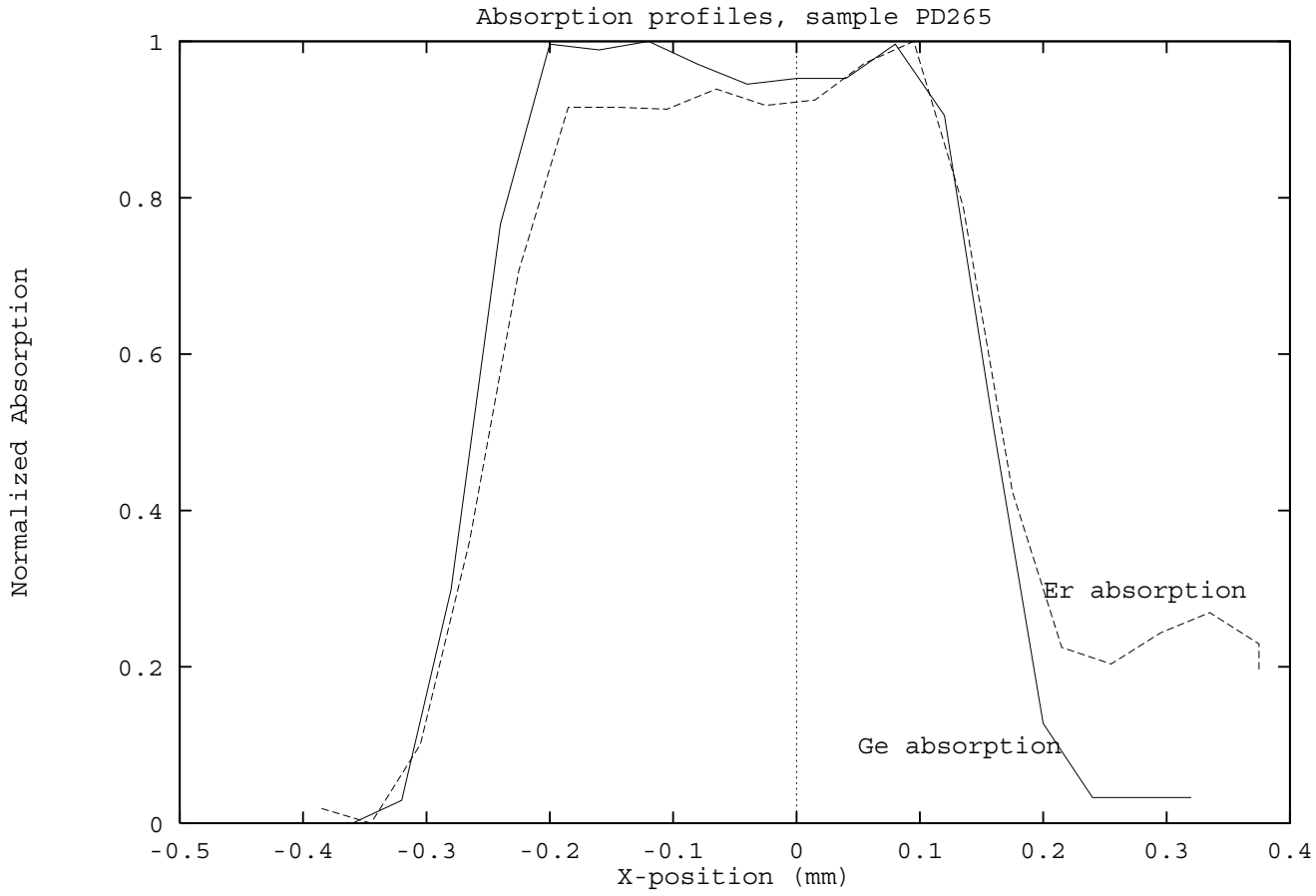

Figure 49: Absorption profile comparisons for Ge and Er scans : Sample PD265

EXAFS spectra were collected at the *Ge* K-edge. Although, as previously mentioned, only a limited k-range was accessible (to $\approx 9\text{Å}^{-1}$, or $\approx 18\text{Å}^{-1}$ using conventional neutron/X-ray diffraction definitions), making data analysis slightly more problematic than usual. Phaseshifts were determined theoretically, and the sample-dependent parameters such as the reduction factor A(k), and the mean free path term λ, were fixed at nominal glass values and held constant between the spectra obtained at different core positions and between the different samples. This ensures consistency between results, and the quoted errors take these uncertainties into account.

The main problem of the limited k-range is the uncertainty introduced when determining the backscattering atomic species. The first atom shell about the excited germanium central atom was, however, certainly oxygen, with fit parameters that suggest a pseudo body centred cubic arrangement of eight oxygen atoms about a central germanium atom. The second atomic shell data proves to be more difficult to interpret, although its presence is statistically significant [81]; the atomic species which can be used to fit the spectra for this shell could either be silicon Table 4 or erbium Table 5. The erbium gives a slightly better fit, but silicon is structurally the more likely major component to the shell, due to its dominance in the overall glass structure. The second shell may however contain some contributions from both atomic species, a hypothesis that unfortunately cannot be tested due to the limited k-range, and therefore low r-space resolution of the data. The magnitude of the Debye-Waller exponent, σ^2, indicates that the second shell contains a large distribution of distances, which would be consistent with this suggestion.

Figures 50,51,52,53 show the spectra, and their respective Fourier transforms, obtained at each core position on the samples ND204 and PD265. The theoretical fits to these spectra and transforms are also shown, as calculated for the parameters

Sample and position	Shell 1(O) Distance Å ± 0.05	Shell 1(O) Coord. No. atoms ± 1	Shell 1 (O) σ^2 Å^2 ± 0.0001	Shell 2 (Si) Distance Å ± 0.05	Shell 2 (Si) Coord. No. atoms ± 2	Shell 2 (Si) σ^2 Å^2 ± 0.0004
ND204 Centre	1.70	8.54	0.008	3.06	9.10	0.023
ND204 Mid	1.71	7.49	0.005	3.05	10.92	0.026
ND204 Edge	1.70	7.44	0.004	3.03	11.90	0.029
PD265 Centre	1.71	9.40	0.010	3.06	6.83	0.023
PD265 Mid	1.71	8.34	0.008	3.06	10.45	0.029
PD265 Edge	1.72	7.86	0.006	3.06	6.43	0.017

Table 4: EXAFS fit parameters *Ge* K edge, *Si* second shell.

Sample and position	Shell 1(O) Distance Å ± 0.05	Shell 1(O) Coord. No. atoms ± 1	Shell 1 (O) σ^2 Å^2 ± 0.0001	Shell 2 (Er) Distance Å ± 0.05	Shell 2 (Er) Coord. No. atoms ± 2	Shell 2 (Er) σ^2 Å^2 ± 0.0004
ND204 Centre	1.70	8.54	0.005	3.00	15.99	0.029
ND204 Mid	1.71	7.66	0.005	3.00	13.66	0.029
ND204 Edge	1.70	6.93	0.003	2.98	21.86	0.040
PD265 Centre	1.71	9.33	0.010	3.00	14.32	0.032
PD265 Mid	1.71	8.34	0.008	2.99	19.60	0.040
PD265 Edge	1.72	8.01	0.006	3.00	9.97	0.023

Table 5: EXAFS fit parameters *Ge* K edge, *Er* second shell.

in Table 1.

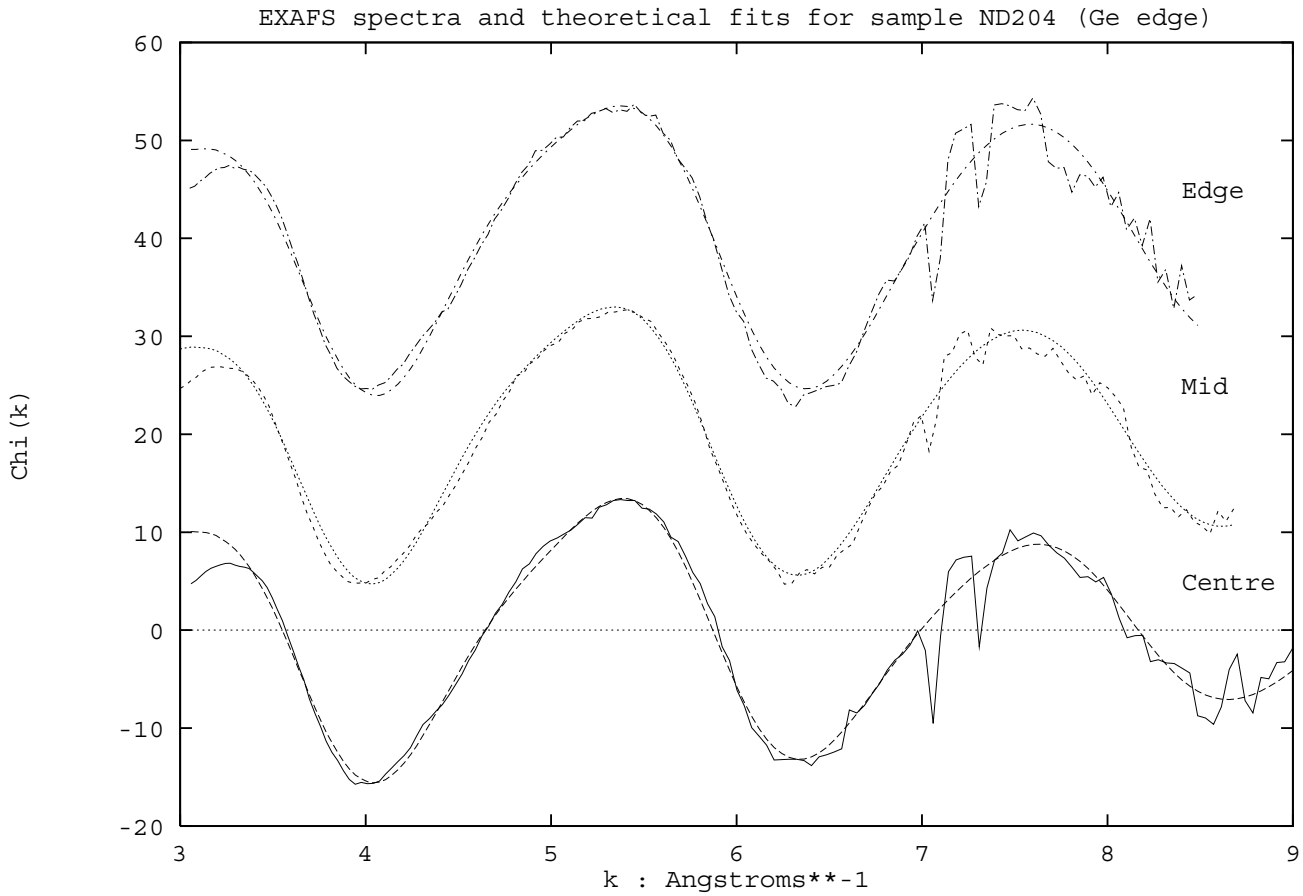

Figure 50: EXAFS spectra at *Ge* K edge : Sample ND204

EXAFS spectra were attempted at the *Er* L_{III} edge but, as anticipated, the signal proved to be too weak for viable analysis due to the extremely low concentrations of erbium present in the samples. EXAFS measurements in a fluorescence geometry would be far more favourable in this compositional range, but the small solid angle subtended by the fluorescence detector made this approach unfeasible. The local environment of erbium atoms in a bulk silicate glass matrix have been probed by EXAFS [84], results showing that the rare earth takes up a local atomic arrangement

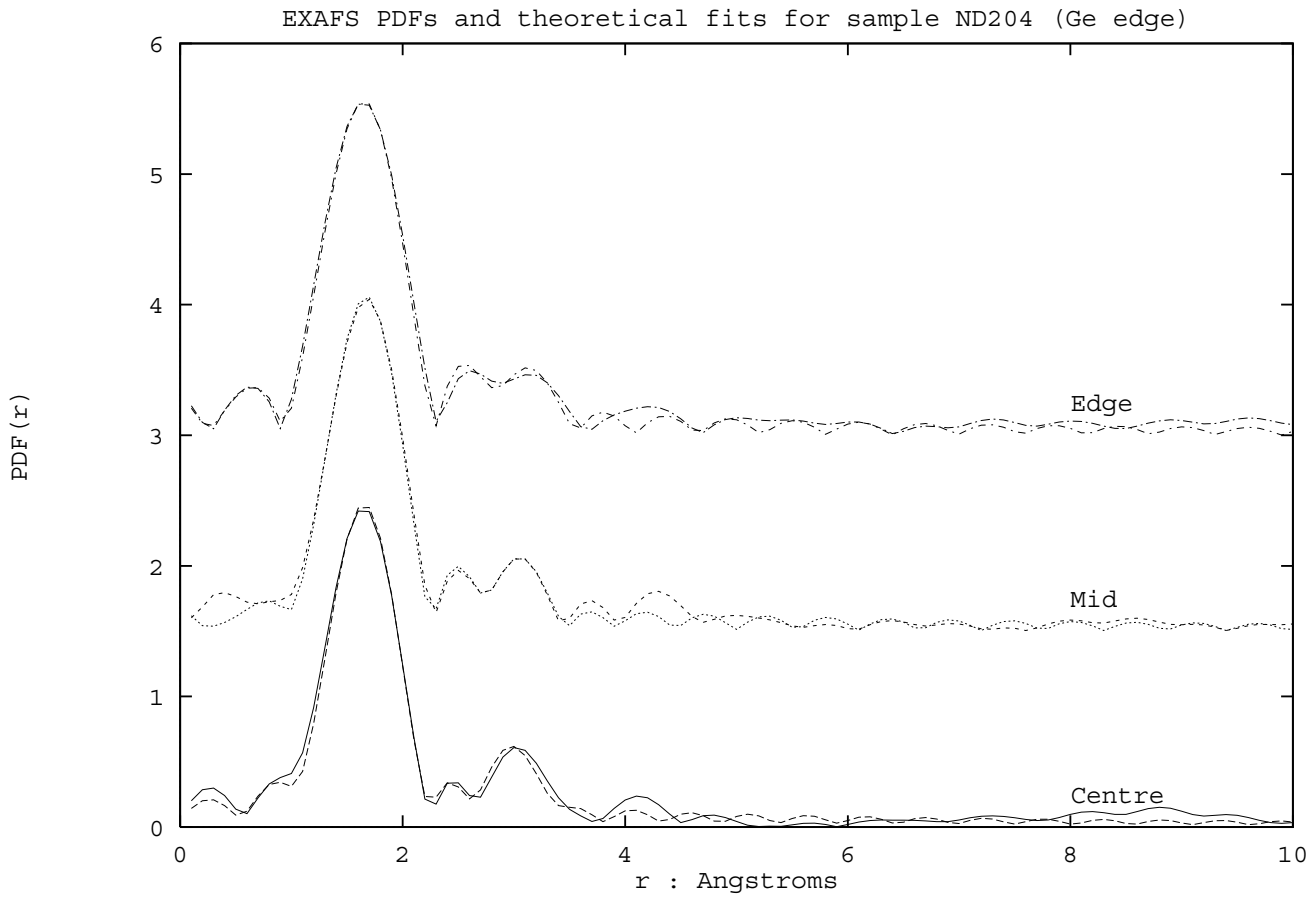

Figure 51: Fourier transform of EXAFS spectra : Sample ND204

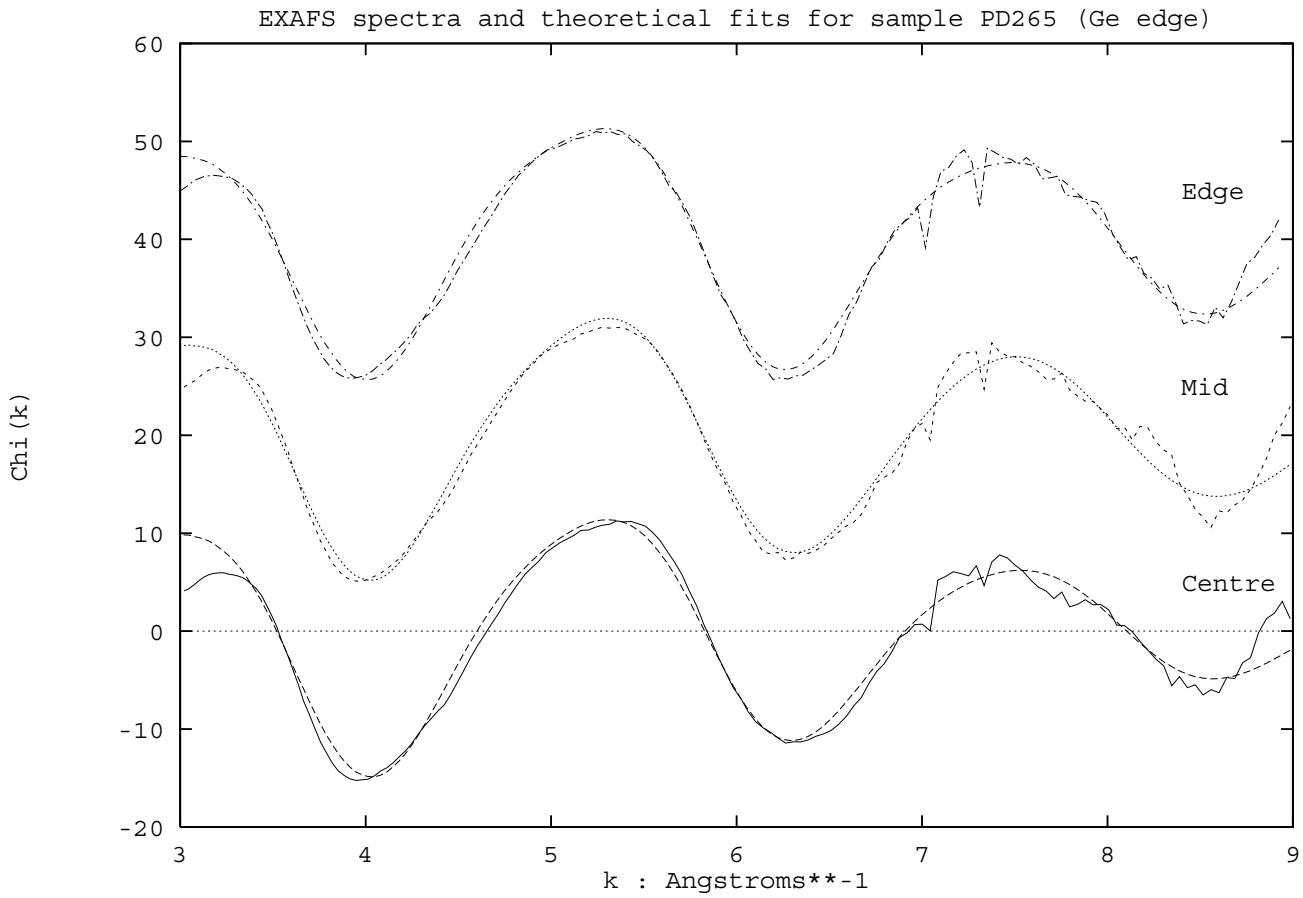

Figure 52: EXAFS spectra at *Ge* K edge : Sample PD265

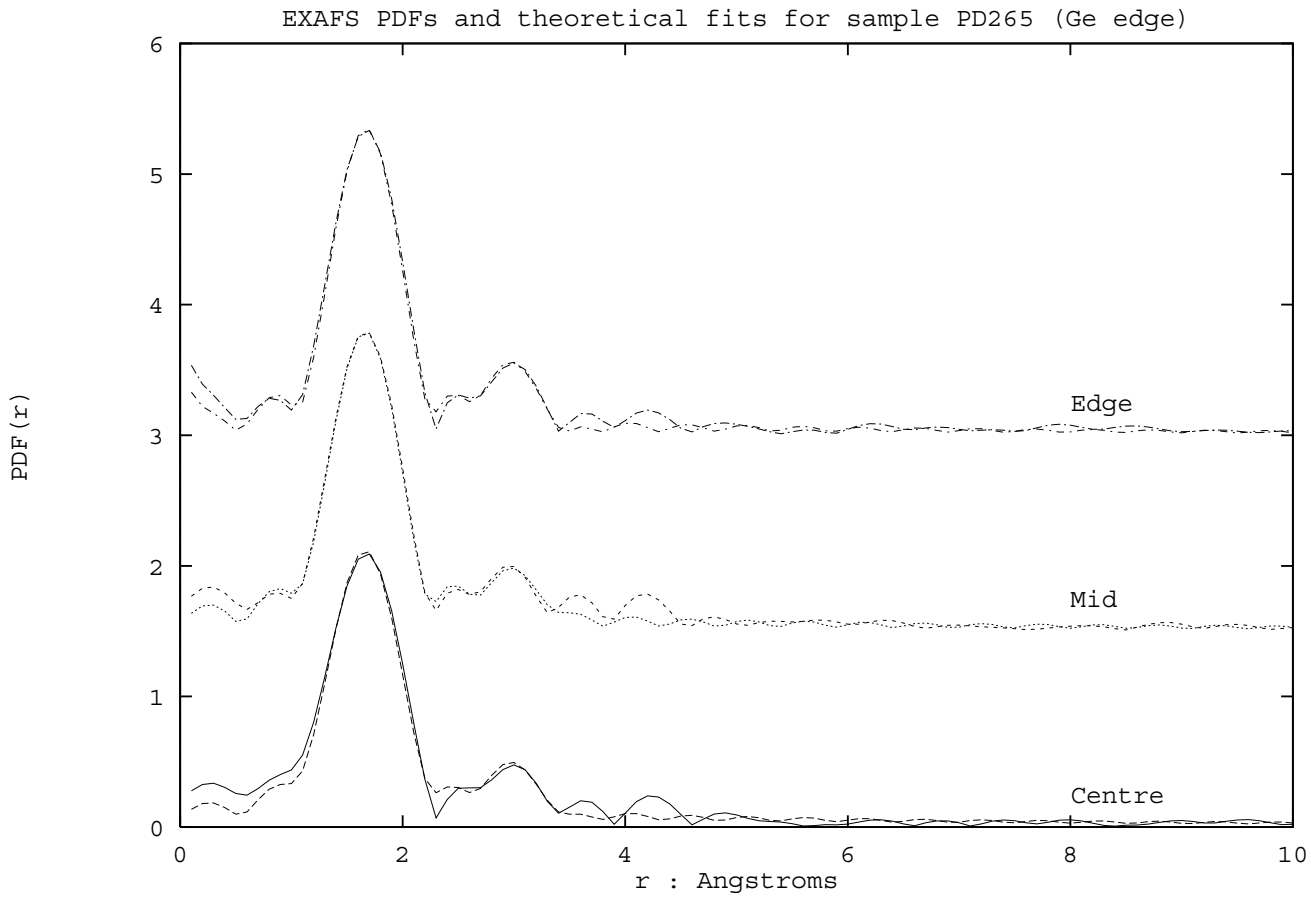

Figure 53: Fourier transform of EXAFS spectra : Sample PD265

similar to the environment that would be prevalent in Er_2O_3 i.e. six oxygen atoms surrounding each Er ion at a distance of 2.28Å. In Er_2O_3 itself, there are six oxygens to each erbium, three at 2.229Åand three at 2.317Å[84]. The spectra obtained from the core region of Sample ND204, in a preliminary test at the erbium absorption edge, show an atomic correlation at the characteristic distance for an oxygen shell. Unfortunately it was not possible to normalise the data to obtain useful coordination numbers.

Recently a 'crystal chemistry' approach has been used [85] in an attempt to cast light on the local environment of rare earth ions embedded in glass structure. Although useful as a first step, this kind of approach still faces the problems associated with crystallite models for amorphous systems if a 'true' description is to be obtained.

An important structural feature that as yet still needs direct confirmation, is the presence or absence of 'clustered' or 'paired' rare earth ions within the glass network. Evidence for such pairing of erbium ions has been obtained indirectly by excited state relaxation time measurements, performed by Delevaque et al. [86]. They determined that if at high powers in erbium doped optical amplifiers, a residual absorption cannot be saturated, the process can only be accounted for by relaxation of the excited states through a short range coupling (<5 Å) between two erbium ions. As yet direct measurements of such correlations, for example by EXAFS, have not been obtained.

The diffraction measurements upon the fibre preform cores were performed on the samples PD265 and PD275. The absorption profiles of the core region again being mapped at the germanium edge to allow positioning of the incident X-ray beam upon the sample. The results of these mappings are shown in Figures 54 and 55.

At each of the three positions a diffraction experiment was performed leading to

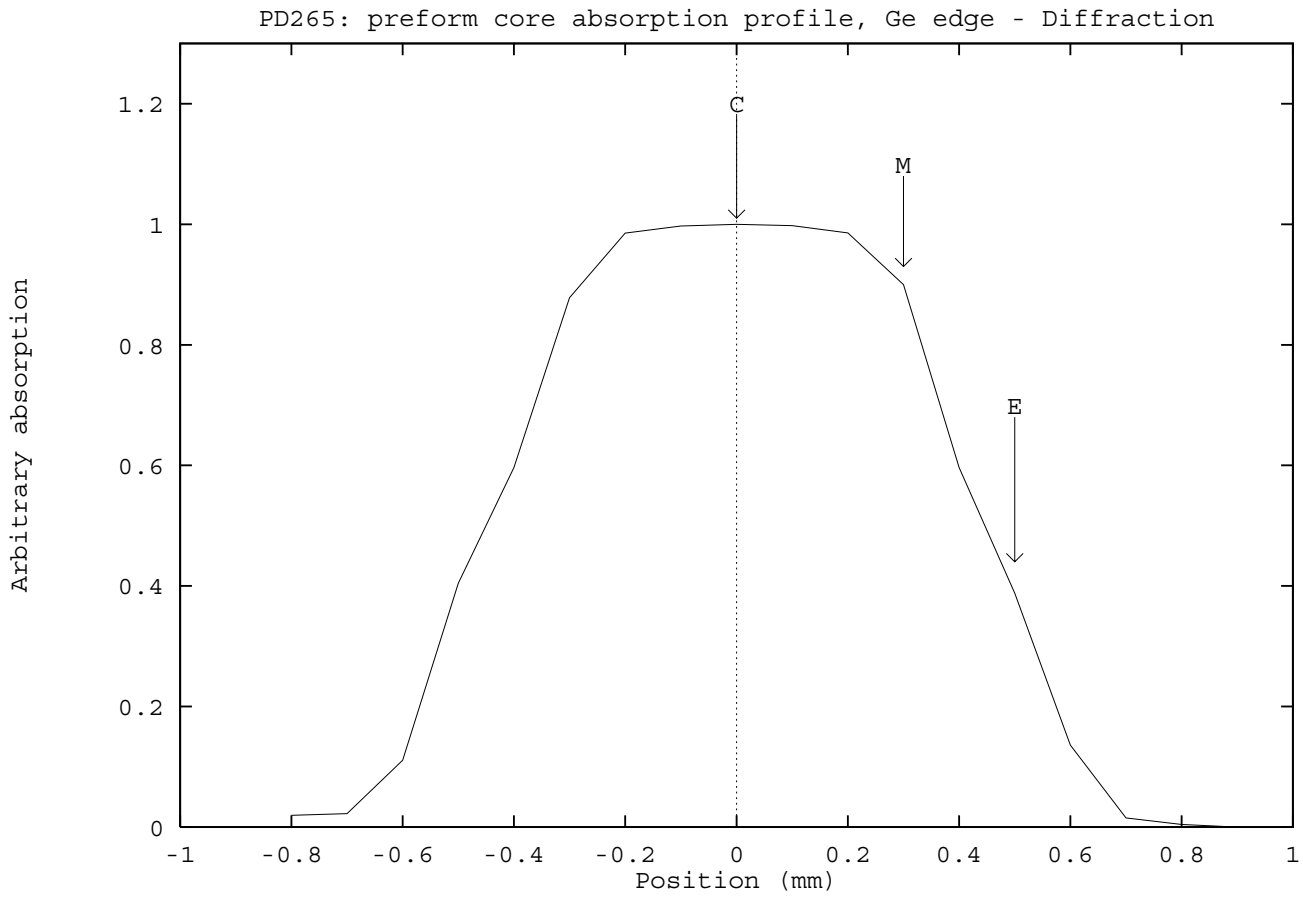

Figure 54: Core region absorption profile sample PD265 : diffraction

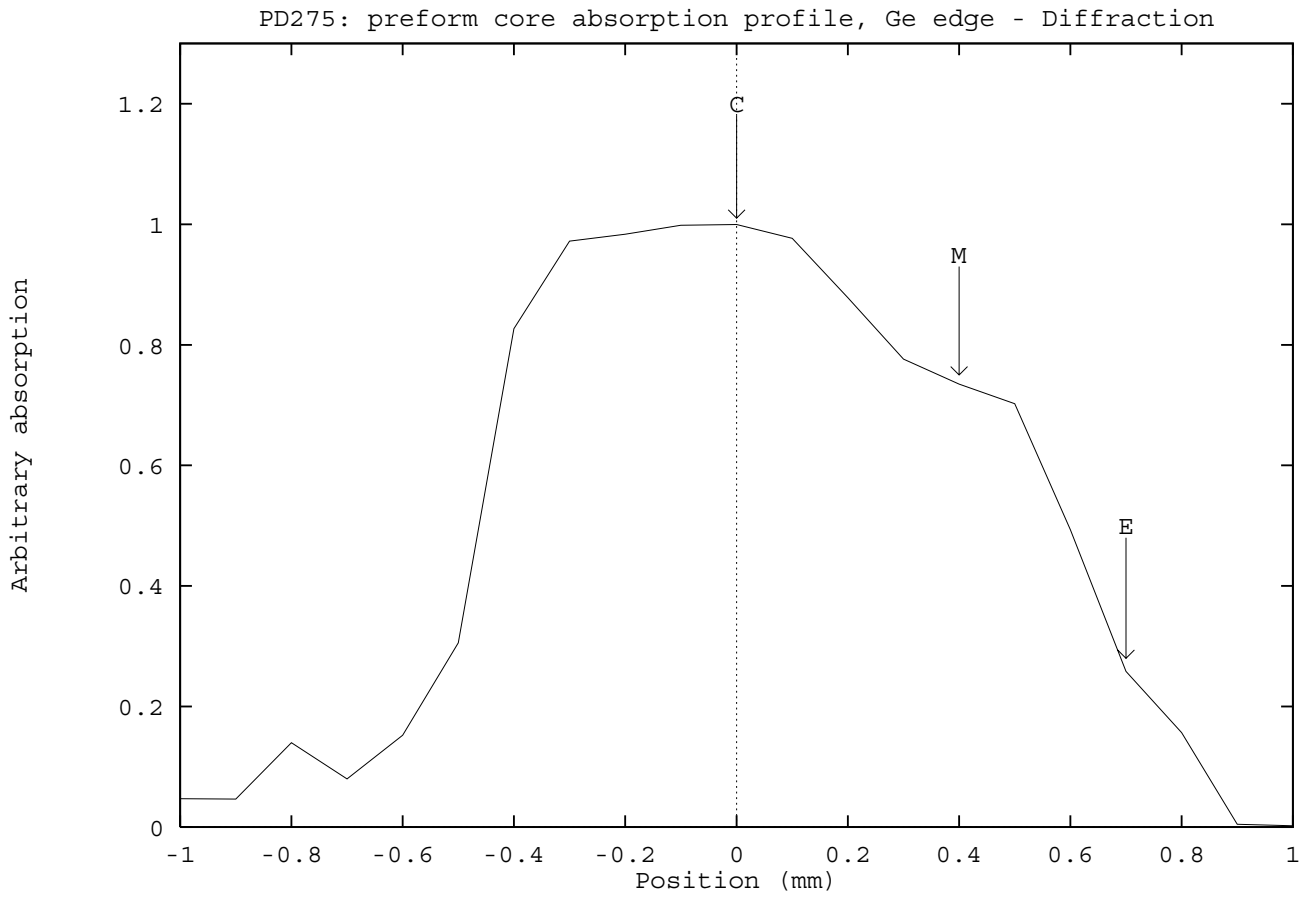

Figure 55: Core region absorption profile sample PD275 : diffraction

the $d(r)$[1] shown in Figures 56 and 57.

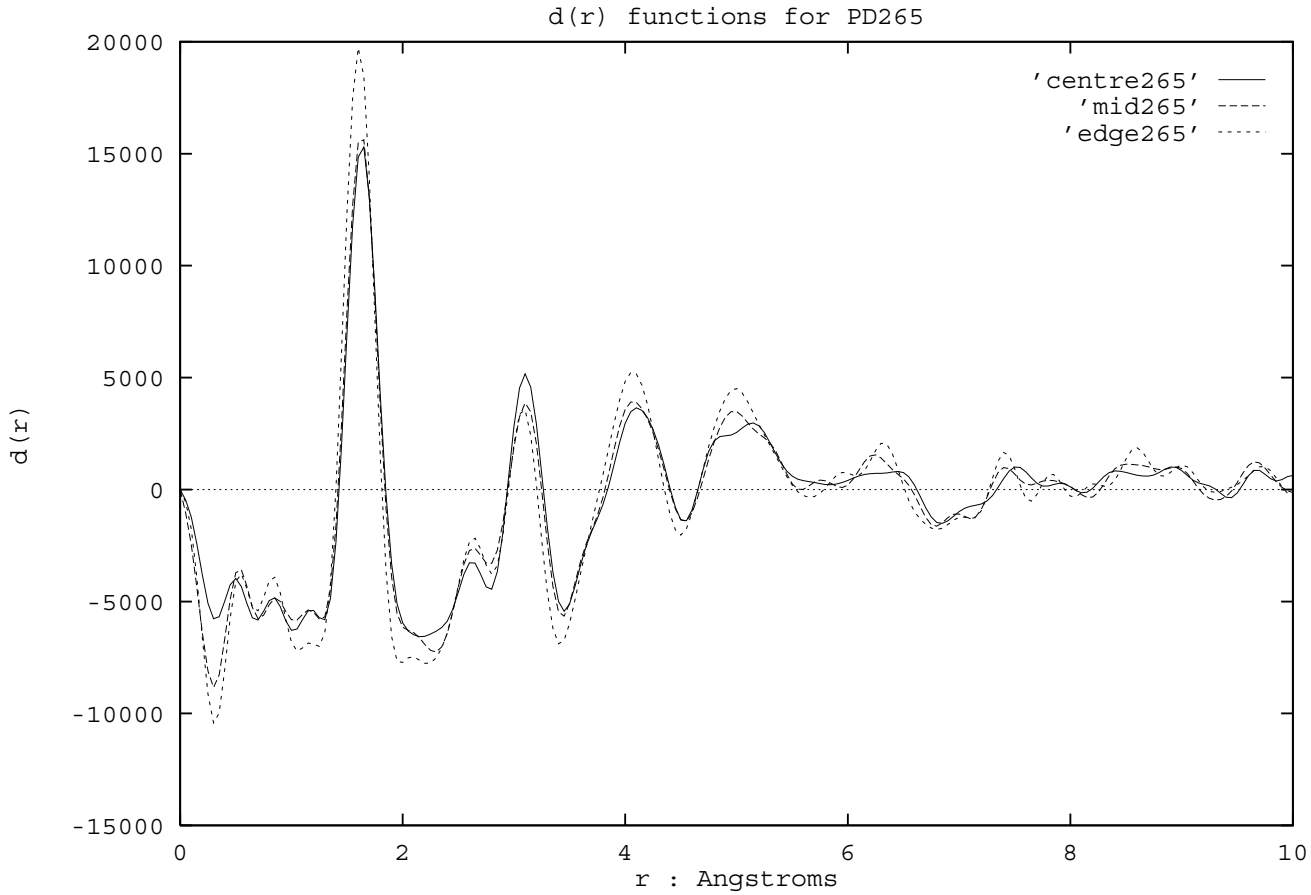

Figure 56: $d(r)$ functions obtained for sample PD265

It can be seen from Figures 56 and 57 that the positions of the peaks are identical between the $d(r)$ taken at the different core positions, these are shown in Table 6. These samples are germanosilicate and germanoaluminosilicate glasses containing nominally 18 wt.% GeO_2 and have diffraction patterns whose features are dominated

[1] $d(r)$ is defined as the simplest Fourier transform of the interference function $i(k)$ i.e. $d(r) = \int_0^{k_m} ki(k)W(k)\sin rk\,dk$ where the terms are as defined in equation 63 i.e. the function contains all the information relating to interatomic correlation distances although lacking the correct scaling of peak areas which requires knowledge as to exact composition of the sample.

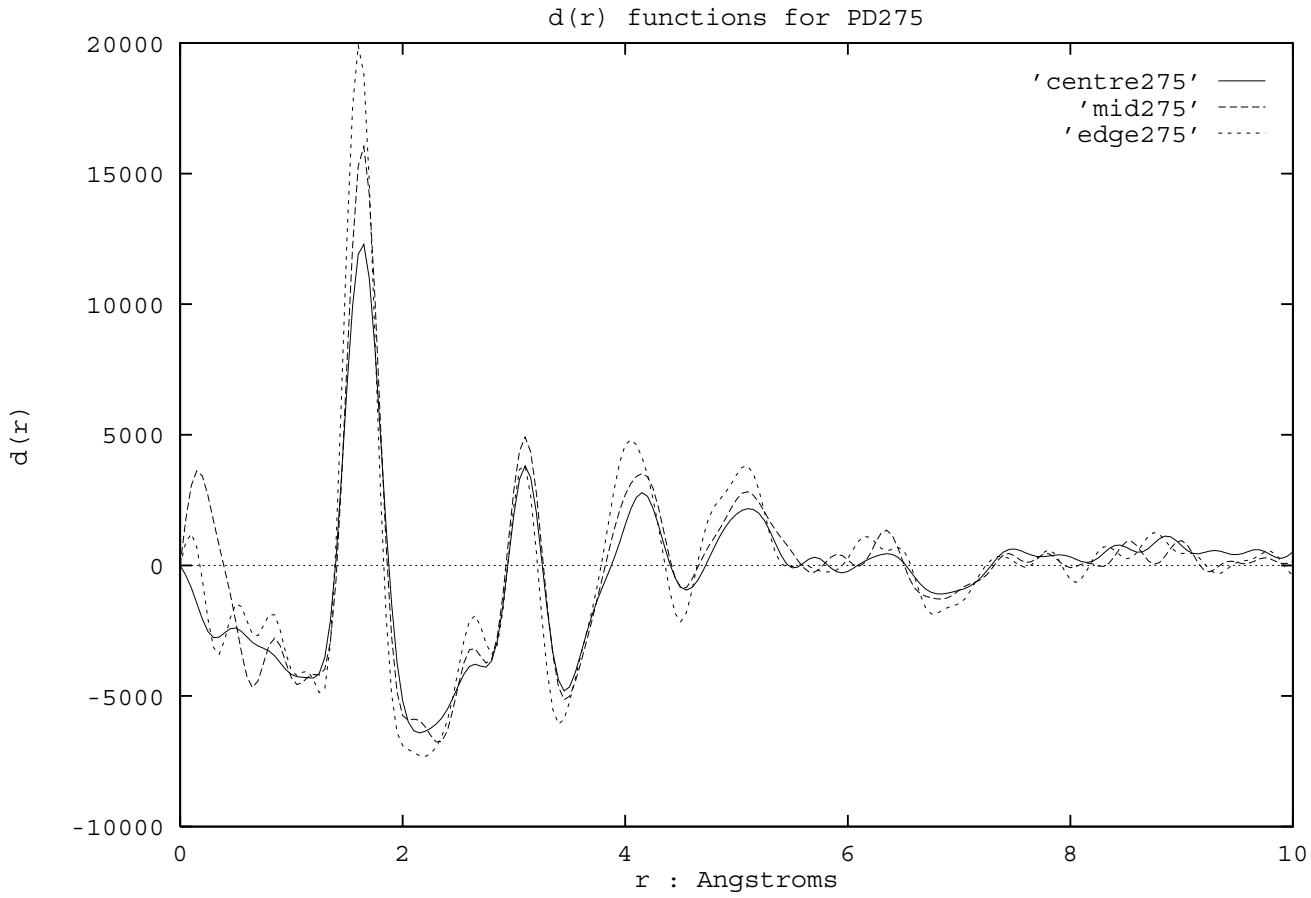

Figure 57: $d(r)$ functions obtained for sample PD275

Sample PD265 Peak positions Å± 0.05	Sample PD275 Peak positions Å± 0.05
1.63	1.61
2.59	2.61
3.12	3.12
4.12	4.16

Table 6: Peak positions for the features in the diffraction $d(r)$ for PD265 and PD275

by the silica component of the material composition. This is reflected in that the positions of the first four peaks correspond very well to the $Si-O$, $O-O$, $Si-Si$ and $Si-2nd\ O$ distances respectively [5]. Due to the unknown nature of the exact composition of the glass in the core region of the fibre, visible in the change in absorption properties reflecting the changing quantities of germanium incorporated into the silica, scaling of the functions so as to give meaningful atomic coordination information is not possible. The trends in the heights of the peaks in the $d(r)$ is consistent with the compositional changes shown in the profile maps but this is the bulk of the information that can be retrieved.

8.3 Conclusions

The mapping of the absorption profiles of the core regions of these samples has demonstrated the close correlation between the concentration of erbium atoms and the germanium present, i.e. the erbium ions introduced via the solution doping technique [46] follow the germanium concentration profile established during the core soot deposition phase of the MCVD process.

The results demonstrate that evaporative losses affecting the germanium dopant similarly affect the erbium incorporated into the preform core. If the assumption that the erbium tracks the germanium profile is valid, measurements of the refractive index profile, which are dependent upon the germanium content of the glass, would also be representative of the erbium concentration.

The germanium atoms have been shown to be incorporated into the silica matrix in a "body centred cubic" fashion with the first shell comprising 8 oxygens and their next nearest neighbours being predominantly silicon. However, there are indications that the erbium atoms may also be correlated to the second shell about the Ge atoms,

although no definitive information is accessible.

The diffraction measurements made upon these samples, show as expected that the structure is dominated by silica, and that no major distortions to the structure are introduced by the inclusion of the germanium codopant.

Chapter 9

Results: metaphosphate glasses

9.1 Diffraction

This chapter covers the results obtained from an X-ray diffraction and EXAFS study of rare earth metaphosphate glasses. The treatment of the diffraction data follows the techniques outlined in the earlier sections, i.e.

- Data corrections e.g. normalization, instrument dead time, background etc.
- Determination of the interference function $i(k)$
- Evaluation of the electron density distribution function $t(r)$
- Fitting of gaussian peaks to the features in $t(r)$
- Comparison of gaussian peaks with evaluated pair functions P_{ij}/r_{ij}

For each of the samples studied by X-ray diffraction, there follow graphs of the corrected experimental data scaled to the independent scattering curve, the obtained interference function, the corresponding $t(r)$ and total gaussian profile fit and the

equivalent $t(r)$ plotted with the composite of gaussian peaks which gives the results. Figures 58,59 show the data plots and fits for praseodymium metaphosphate glass, Figures 60,61 those for europium metaphosphate glass and Figures 62,63 the data and fits obtained for terbium metaphosphate glass.

The tables of results obtained from the fits to $t(r)$ are as follows:

Peak Position Å$\pm$ 0.05	Peak Area $\propto$ electrons^2	Atomic correlations assigned
1.57	2816	P-O
2.43	4762	Pr-O and O-O
2.95	2881	complex
3.77	7770	complex
4.85	24457	complex

Table 7: Diffraction results for praseodymium metaphosphate glass

Peak Position Å$\pm$ 0.05	Peak Area $\propto$ electrons^2	Atomic correlations assigned
1.58	2770	P-O
2.36	5640	Eu-O and O-O
2.96	3072	complex
3.68	6688	complex
4.71	30343	complex

Table 8: Diffraction results for europium metaphosphate glass

Peak Position Å$\pm$ 0.05	Peak Area $\propto$ electrons^2	Atomic correlations assigned
1.58	2483	P-O
2.33	6245	Tb-O and O-O
2.95	2649	complex
3.65	6986	complex
4.65	31258	complex

Table 9: Diffraction results for terbium metaphosphate glass

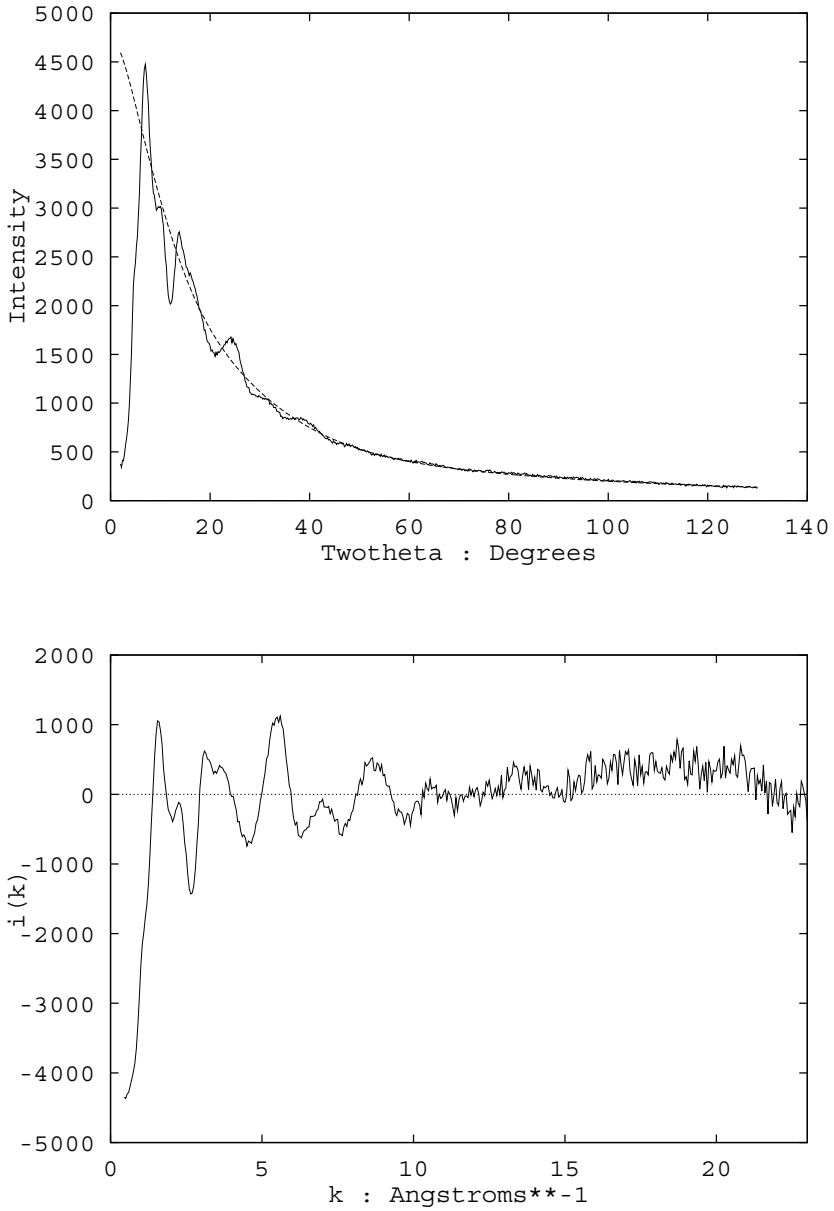

Figure 58: Top: Praseodymium metaphosphate glass diffraction and self scattering, Bottom: Praseodymium metaphosphate glass interference function i(k)

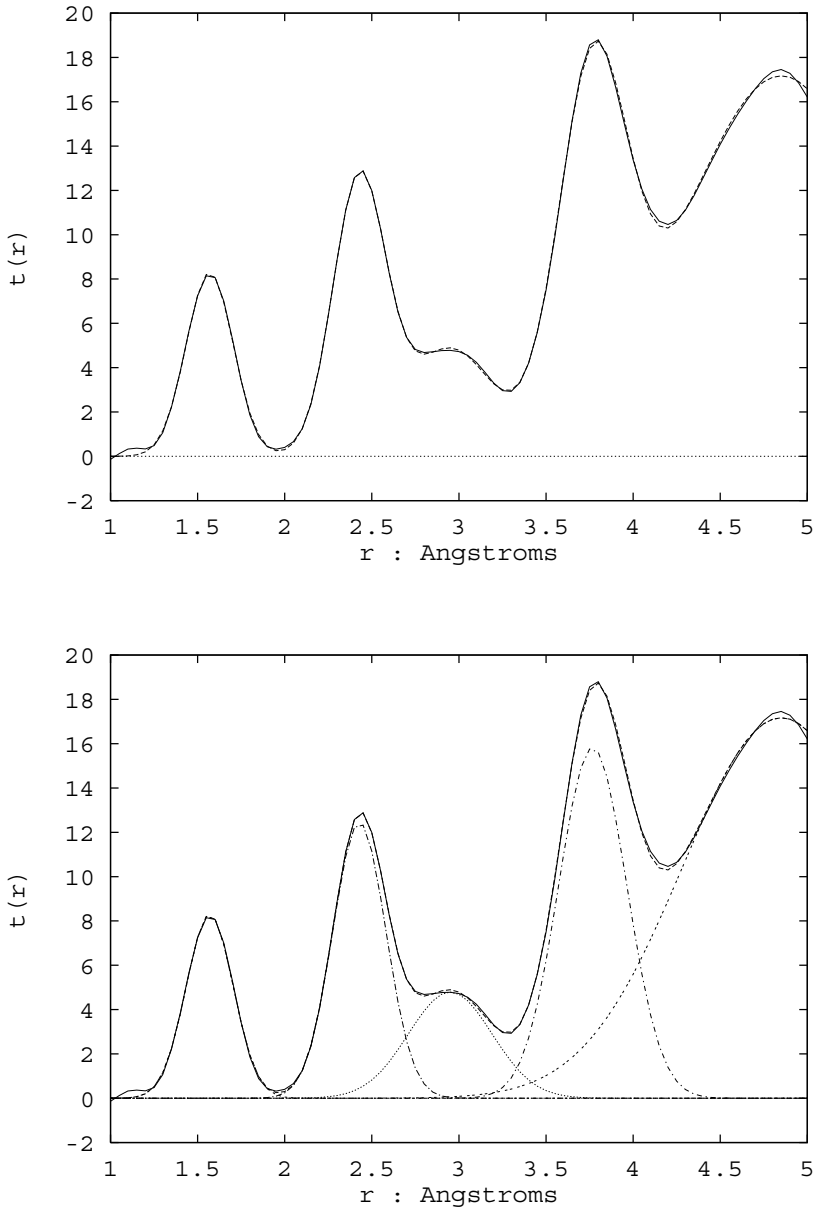

Figure 59: Top: Praseodymium metaphosphate glass t(r) and fit, Bottom: Praseodymium metaphosphate glass t(r) and composite fit

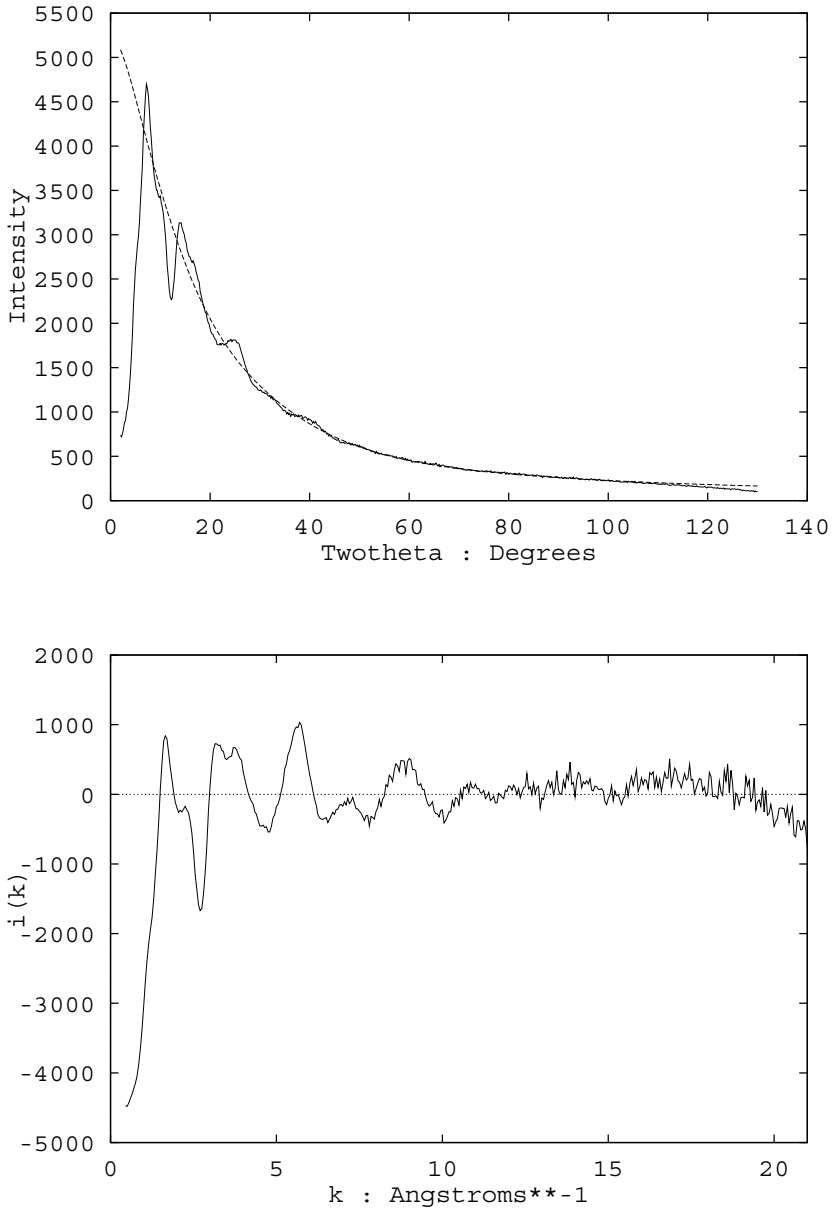

Figure 60: Top: Europium metaphosphate glass diffraction and self scattering, Bottom: Europium metaphosphate glass interference function i(k)

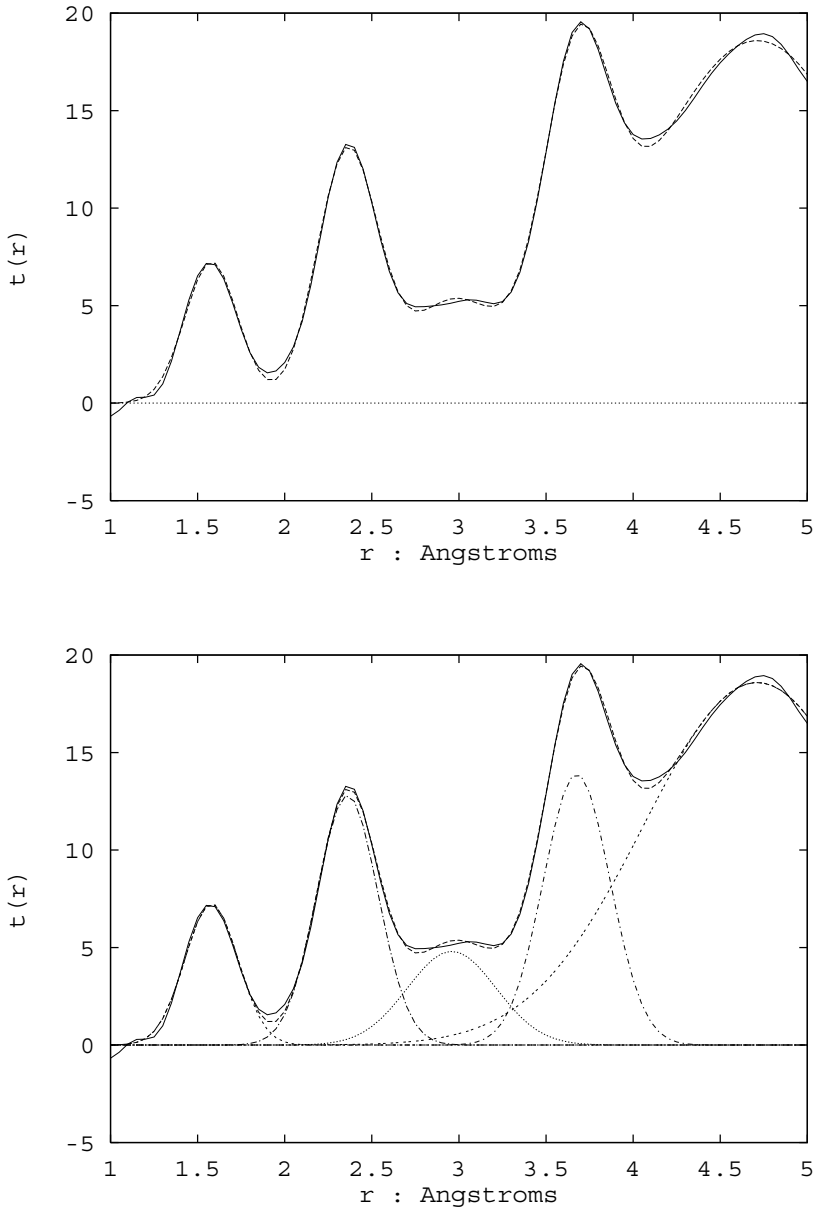

Figure 61: Top: Europium metaphosphate glass t(r) and fit, Bottom: Europium metaphosphate glass t(r) and composite fit

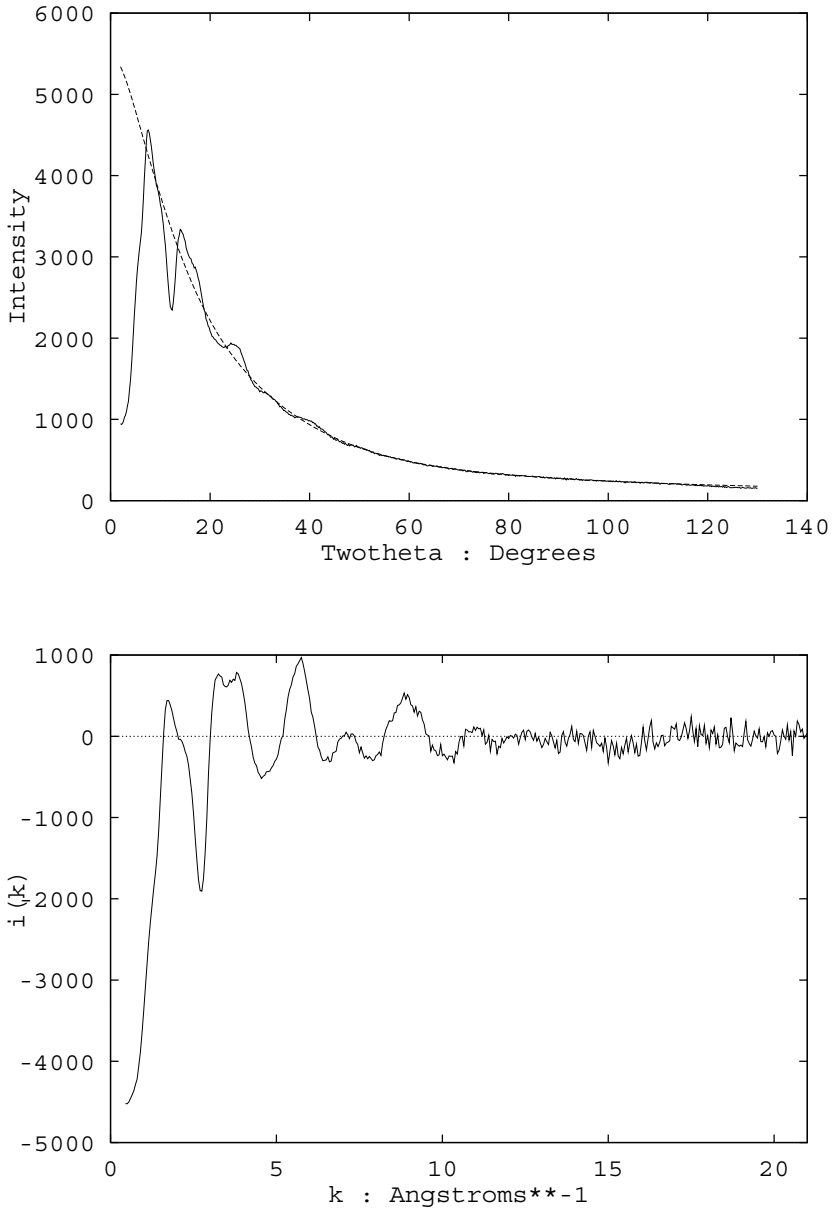

Figure 62: Top: Terbium metaphosphate glass diffraction and self scattering, Bottom: Terbium metaphosphate glass interference function i(k)

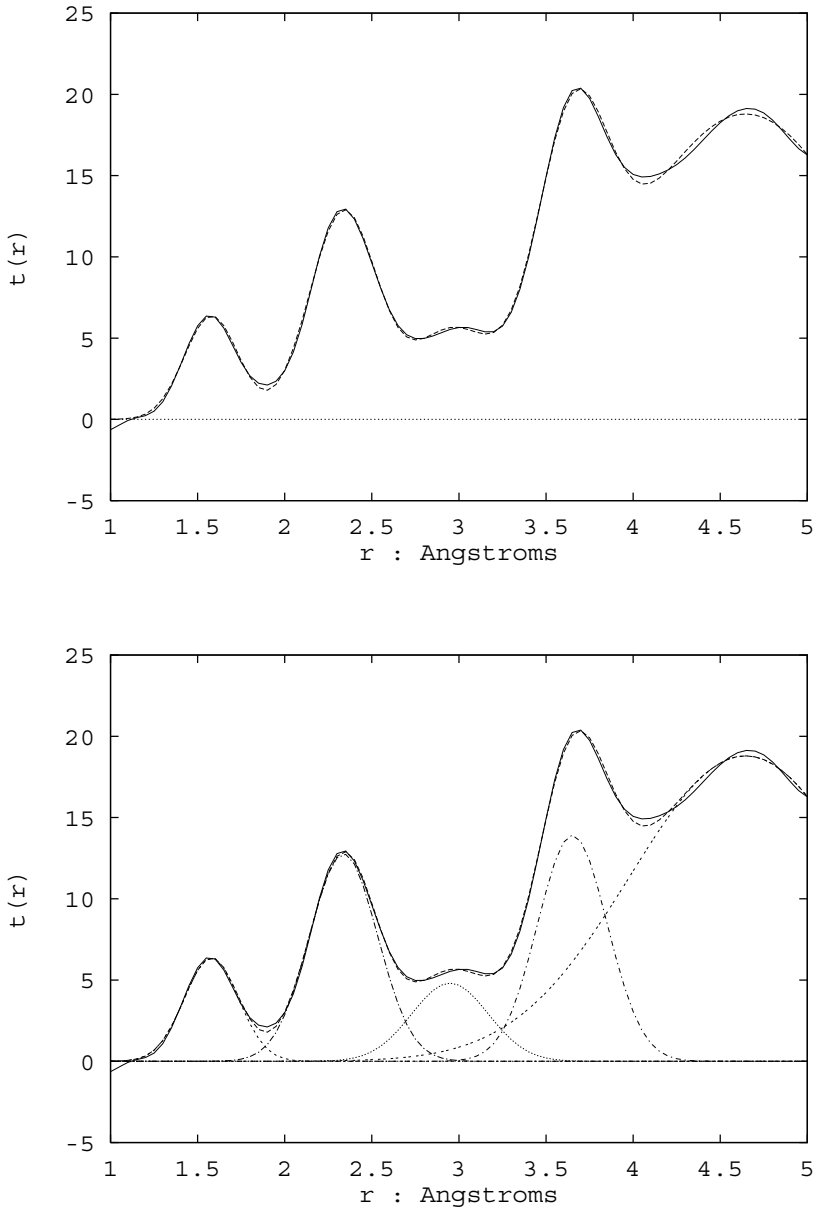

Figure 63: Top: Terbium metaphosphate glass t(r) and fit, Bottom: Terbium metaphosphate glass t(r) and composite fit

The gaussian peaks fitted above are best interpreted in terms of the pair functions P_{ij} evaluated at their respective r_{ij}. These being calculated from the self scattering curves denoted by f_i where i is the atom type. The following table contains information calculated for the P-O, Ln-O (where Ln is a rare earth species) and O-O distances relevant to the first two peaks in the evaluated $t(r)$.

Sample	Pair Function	Peak Position Å$\pm$ 0.05	Peak Area $\propto$ electrons^2
Pr	P-O	1.60	105
	Pr-O	2.35	447
	O-O	2.50	30
Eu	P-O	1.60	104
	Eu-O	2.30	330
	O-O	2.50	30
Tb	P-O	1.60	103
	Tb-O	2.30	340
	O-O	2.50	30

Table 10: P_{ij}/r_{ij} evaluated for comparison with $T(r)$ fit results

It should be noted how dominant the Ln-O contribution is over O-O, this is due to the much larger number of electrons involved in correlations with rare earth atoms. This fact gives a strong indication that the $t(r)$ obtained from the rare earth metaphosphates are dominated by rare earth correlations when features appear at distances that can be assigned to say a mixture of rare earth and non-rare earth correlations such as the second peaks in the $t(r)$.

A cursory inspection of the $t(r)$ data shows that the positions of the first main features (peaks) are consistent with the bulk phosphate glass network. The second peak in the $t(r)$ contains contributions from both the rare earth-oxygen and oxygen-oxygen correlations present in the glass, although as previously mentioned those features are dominated by the correlations involving the rare earth element.

The first peak occurring at $\approx 1.57(8)$Å is characteristic of the $P-O$ correlation expected for any phosphate glass system consisting of linked PO_4 tetrahedra, (see for example [22, 23], where the $P-O$ distance has been determined as 1.55Å and 1.6Å respectively). The second distance is slightly more difficult to assign being a combination of the rare earth-oxygen correlation and the oxygen-oxygen correlation that would be present in the PO_4 base unit. The $O-O$ distance has been allocated to 2.5Å [23] in previous studies of metal doped phosphate glasses, but in this case, due to the similarity between the distance associated with the rare earth oxygen and oxygen-oxygen correlations, individual allocations cannot be made. The average second correlation distance i.e. that involving rare earth-oxygen, displays a trend that is consistent with the Lanthanide contraction; the reduction in size of the rare earth ion as the periodic table is traversed. Several other peaks are visible in the $t(r)$ curves, but a definitive assignment of atomic correlations becomes impossible beyond the second peak.

The areas of the first two peaks have been evaluated from the fit, albeit in a rather crude fashion due to difficulties in accounting for all the model dependent subtleties that effect the final interpretation of results. The calculated pair functions P_{ij}/r_{ij} have been used to obtain an estimate of the coordination numbers associated with the correlations assigned to each of the first two peaks. Great care must be taken with these results due to the large uncertainties introduced in calculating the areas of the various P_{ij} since a significant part of the function may be contained in the wings of the transform function. Associated errors with the values quoted for the $t(r)$ peak areas are also large due to difficulties in assigning definitive weightings to the series of gaussian profiles used to fit the $t(r)$, allowance must be made for this lack of resolution when determining the coordination numbers.

The area of the first peak in the $t(r)$ for all three samples is consistent with a fourfold coordination of oxygen about phosphorus, the correlation strengths being calculated to account for the chosen structural unit in the analysis, notably $Ln(PO_3)_3$ i.e. by application of equation 63. An example calculation of this simplistic kind is given in [5], applied to vitreous silica. A more accurate approach is also demonstrated in this paper but this demands the fitting of a model structure. The coordination numbers indicated by the second peak (using the simplest approximation that the bulk of the correlation is from $Ln - O$ and $O - Ln$) are indicative of of an eight or ninefold coordination of oxygen about the rare earth, this being an upper limit for the coordination due to the above approximation. Coordination numbers of this magnitude are acceptable for rare earth ions due to their predominantly ionic bonding nature.

The peak positions in the $t(r)$ are evaluated to within ± 0.05Å, and are more robust than the coordination numbers.

9.2 EXAFS

The EXAFS data taken on station 7.1 is presented in the following pages. The analysis of this data was performed using EXCURV90 [79], the preprocessing of the data was performed using EXCALIB [87] and EXBACK [88]. The analysis was made in the absence of suitable calibrants for variable parameters within the EXAFS theory, but consistency was maintained using suitable theoretical values throughout the analyses performed. Trends between the data sets can hence be reliably determined as well as reasonable indications on the magnitude of the structural parameters notably bond distances and coordination numbers.

Data was taken on a series of rare earth metaphosphate glasses, the results being

shown graphically in pairs, i.e. the experimentally measured EXAFS functions $\chi(k)$ and fits, as well as the corresponding pair distribution functions (pdfs). The $\chi(k)$ were necessarily filtered to remove a contaminant feature in all rare earth L_{III} edge EXAFS, notably the double electron excitation event which occurs between 5 and 7 $Å^{-1}$ in the measured $\chi(k)$ [76, 77, 78]. Failure to remove this discontinuity (Figure 64 (Top)) leads to difficulty when trying to fit theoretical models to the experimental function. When present, a double electron excitation event is most often associated with a peak in the pdf at an unphysically low interatomic correlation distance (Figure 64 (Bottom)), a fact that can be used to advantage by Fourier filtering techniques which allow removal of spectral frequency components by back transformation of a corrected pdf.

The $\chi(k)$ and pdfs are shown in Figures 65-70, and the best fit structural parameters are given in table 11.

The errors quoted in the tables of best fit structural parameters 11, are of a purely statistical nature, being calculated by the methods of Joyner et al. [81]. The quoted uncertainties need clarification; due to the lack of a suitable calibrant, the variation in coordination number is approximately ± 1 atom in addition to the quoted statistical variation. This is due to an inability to determine accurately the magnitude of non-EXAFS producing absorption effects, modelled in the plane-wave approximation by the parameter $A(k)$. The lack of a calibrant system also leads to an uncertainty in the theoretically calculated phase shifts, that are induced in the propagating electron wave, as well as other electron parameters, this leads to errors in the quoted distances of approximately ± 0.005Å. However the lack of calibrant in these experiments is not as damaging as may first appear since trends can clearly be probed given that non-calibrated parameters are fixed at values suitable for glasses in

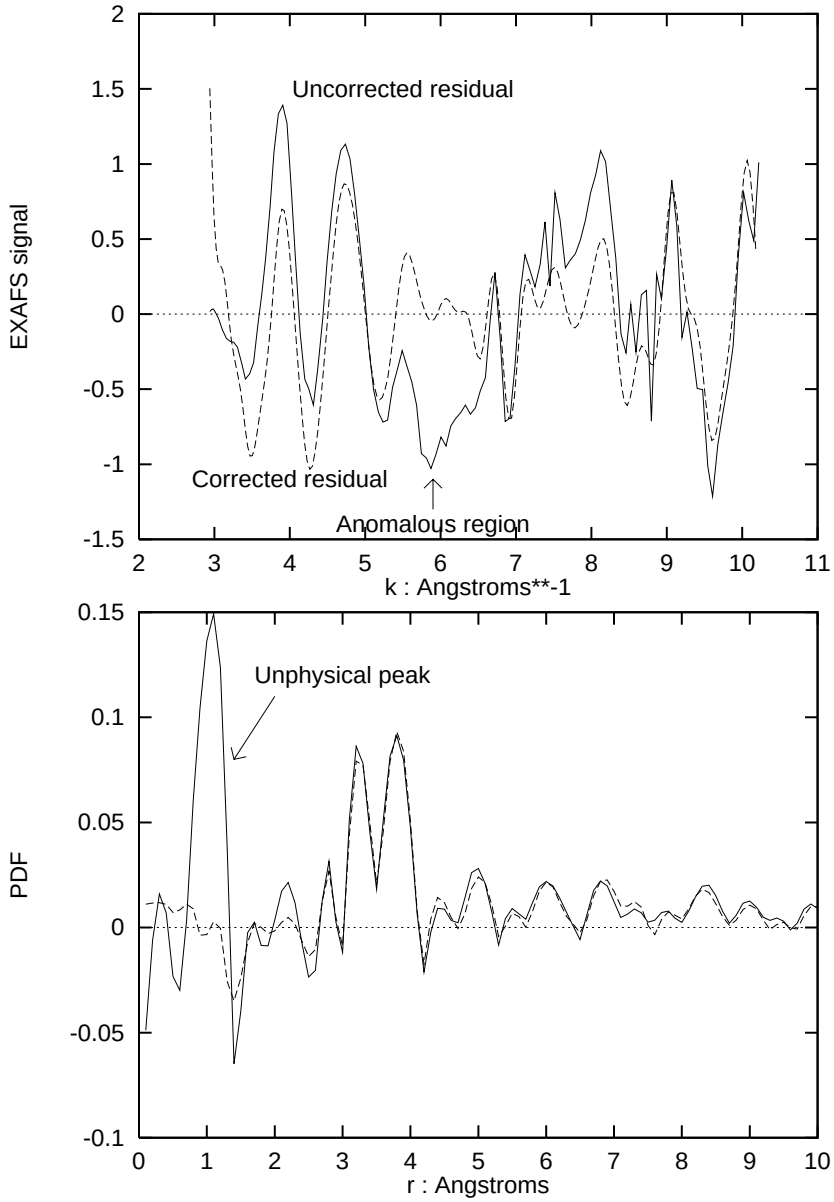

Figure 64: Top: Residual between EXAFS function and first shell fit, uncorrected for anomalous feature at ∼6Å (__) and following filtering to remove contaminant feature (_ _ _) Bottom: Fourier transform of residuals, displaying the unphysical low-r feature in the uncorrected Fourier transform (__) and its absence in the filtered transform (_ _)

Praseodymium metaphosphate glass			
Atom type	Coordination Number Atoms	Shell distance Å	σ^2 Å^2
Oxygen	6.2 ± 0.2	2.38 ± 0.002	0.013 ± 0.0005
Phosphorus	1.2 ± 0.2	2.92 ± 0.004	0.009 ± 0.002
Oxygen	3.5 ± 0.4	4.08 ± 0.004	0.006 ± 0.001
Neodymium metaphosphate glass			
Atom type	Coordination Number Atoms	Shell distance Å	σ^2 Å^2
Oxygen	8.7 ± 1.0	2.36 ± 0.005	0.018 ± 0.0005
Phosphorus	4.6 ± 5.1	2.93 ± 0.043	0.045 ± 0.025
Oxygen	1.85 ± 0.3	3.83 ± 0.004	0.006 ± 0.002
Europium metaphosphate glass			
Atom type	Coordination Number Atoms	Shell distance Å	σ^2 Å^2
Oxygen	6.2 ± 0.2	2.28 ± 0.003	0.012 ± 0.0005
Phosphorus	0.8 ± 0.5	3.62 ± 0.018	0.005 ± 0.007
Oxygen	1.3 ± 0.7	3.99 ± 0.017	0.0005 ± 0.005
Gadolinium metaphosphate glass			
Atom type	Coordination Number Atoms	Shell distance Å	σ^2 Å^2
Oxygen	5.2 ± 0.3	2.27 ± 0.003	0.008 ± 0.0006
Phosphorus	1.8 ± 0.3	2.72 ± 0.007	0.002 ± 0.002
Oxygen	1.3 ± 0.3	3.23 ± 0.009	0.004 ± 0.002
Oxygen	1.0 ± 0.4	3.94 ± 0.007	0.007 ± 0.003
Terbium metaphosphate glass			
Atom type	Coordination Number Atoms	Shell distance Å	σ^2 Å^2
Oxygen	7.0 ± 0.2	2.25 ± 0.002	0.014 ± 0.0004
Phosphorus	4.1 ± 0.8	3.92 ± 0.008	0.015 ± 0.003
Holmium metaphosphate glass			
Atom type	Coordination Number Atoms	Shell distance Å	σ^2 Å^2
Oxygen	5.8 ± 0.1	2.20 ± 0.002	0.010 ± 0.0003
Phosphorus	5.1 ± 0.6	3.88 ± 0.006	0.013 ± 0.002

Table 11: EXAFS fit parameters

general, and the reasonable assumption is made that the physical properties of each glass are similar.

The most striking trend evident in the data is the systematic contraction of the first shell rare earth-oxygen distance from 2.38Å for praseodymium metaphosphate glass to 2.20Å in the holmium metaphosphate glass. This is consistent with the well known property of the Lanthanide elements; the contraction in their ionic size as the period is traversed from lighter to heavier elements, i.e. the lanthanide contraction.

The first shell coordination numbers fall between 6 and 8 for oxygens about a rare earth ion, this hints at an octahedral or cubic arrangement of the oxygens, rare earth oxides characteristically having an octahedral arrangement for oxygens about rare earth ions. The range of results suggesting a possible mixture of the two configurations within the samples.

In some samples there is evidence for the second shell being a rare earth-phosphorus correlation, but the errors are large, along with the distribution in coordination numbers and distances allocated. The second rare earth-oxygen correlation however proved to be more consistent between samples with an associated distance between 3.8Å and 4.1Å, although the variation in coordination number is still large i.e. between 1 and 5 oxygens. This wide variation in results for parameters associated with more distant atomic shells is partly due to the amorphous nature of the material i.e. the lack of any firm short range order beyond the first interatomic correlation. No evidence is found for any rare earth-rare earth correlations, an important fact for future interpretation of the optical and magnetic properties of these glasses.

The values of σ presented in the table correspond to a measure of the static and thermal disorder present in the system i.e. a distribution in the evaluated interatomic distances (manifest in the Fourier transform of the various $\chi(k)$ by the width of the

peak). It is likely that here, as for other glasses, the static disorder term will dominate, but a temperature study would be necessary to obtain further information as to the weightings of the particular contributions.

9.3 Discussion

The combination of complementary techniques has proved particularly useful in the study of these metaphosphate glasses. Both individual experimental methods benefitting from a degree of calibration resulting from the independent evaluation of structural parameters. This complementarity is particularly useful in the light of compositional uncertainties that influence the diffraction data as well as the lack of suitable calibrant systems for EXAFS parameters.

Due to the lack of a suitable calibrant system for the EXAFS results, the evaluated distances between the rare earth atoms and their neighbours tend to be contracted. This is a failing of the theoretical model used within EXCURV90 [79], exacerbated by the inability to calibrate the system dependent constants within the theoretical model. The diffraction data therefore are of great use in checking the evaluated distances, although the trends visible in the EXAFS data are unaffected by the lack of calibrant system.

The results obtained allow the basis for a structural model of rare earth metaphosphate glasses. Firstly the diffraction data have established that it is acceptable to build the bulk phosphate network from PO_4 tetrahedra, this being established by the evaluated first correlation length displayed in the $t(r)$ and the strength of this correlation. The EXAFS results have demonstrated that the rare earth ions are incorporated into the phosphate network in high coordination states, each typically surrounded by between six and eight oxygen atoms. This suggests that the network

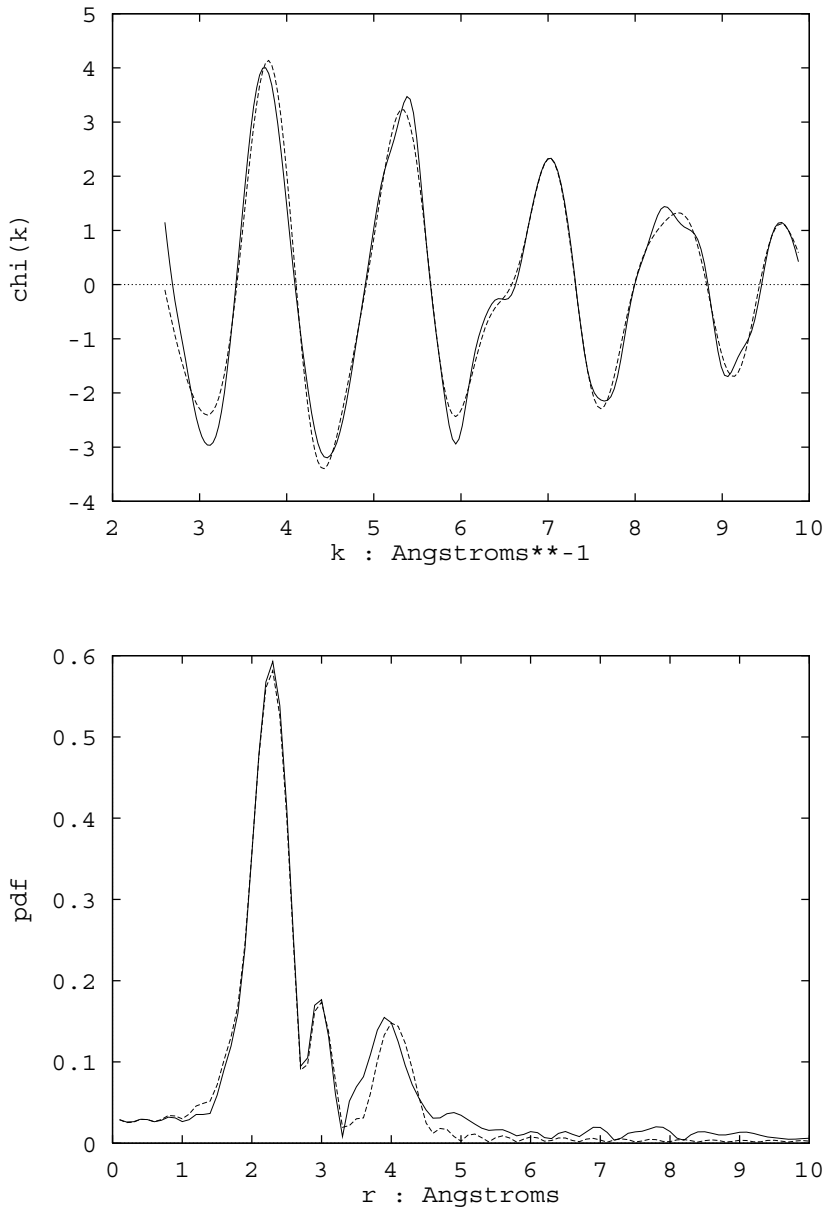

Figure 65: Top: Praseodymium metaphosphate glass EXAFS $\chi(k)$, Bottom: Praseodymium metaphosphate glass EXAFS pdf

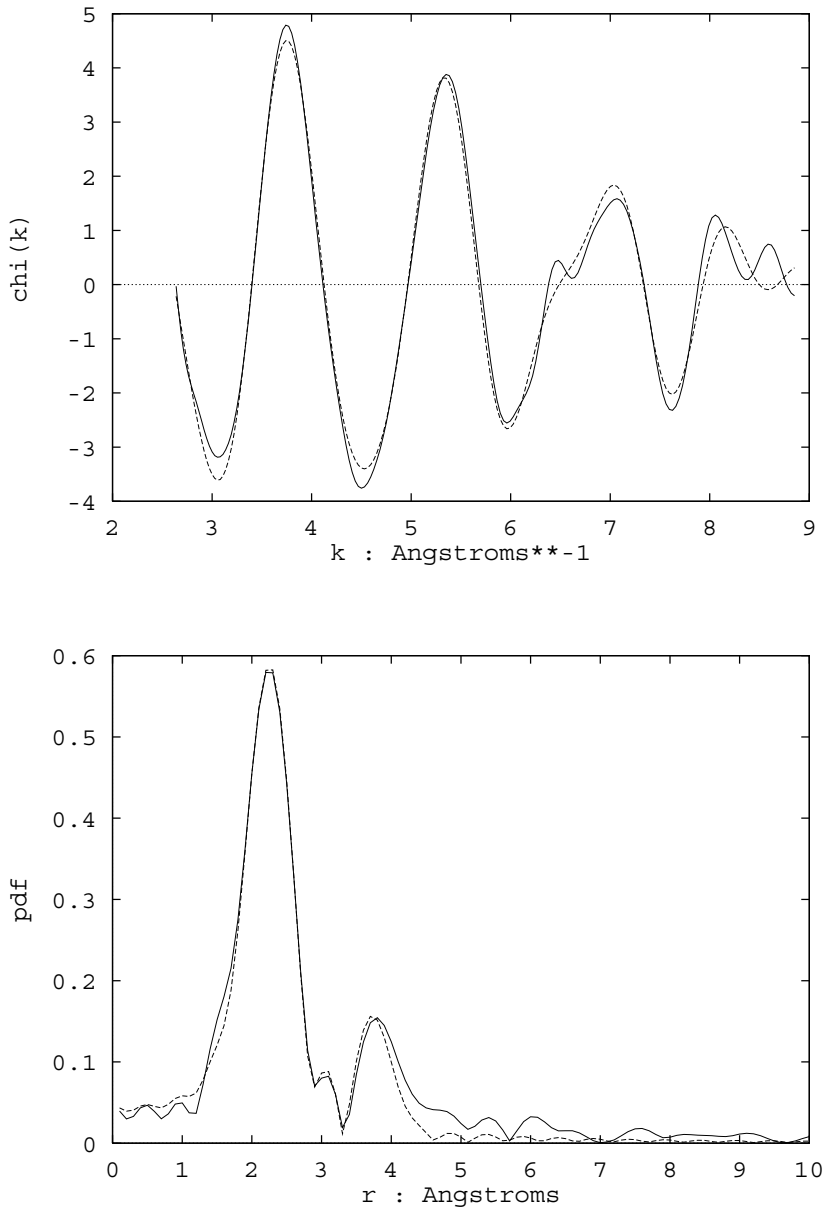

Figure 66: Top: Neodymium metaphosphate glass EXAFS $\chi(k)$, Bottom: Neodymium metaphosphate glass EXAFS pdf

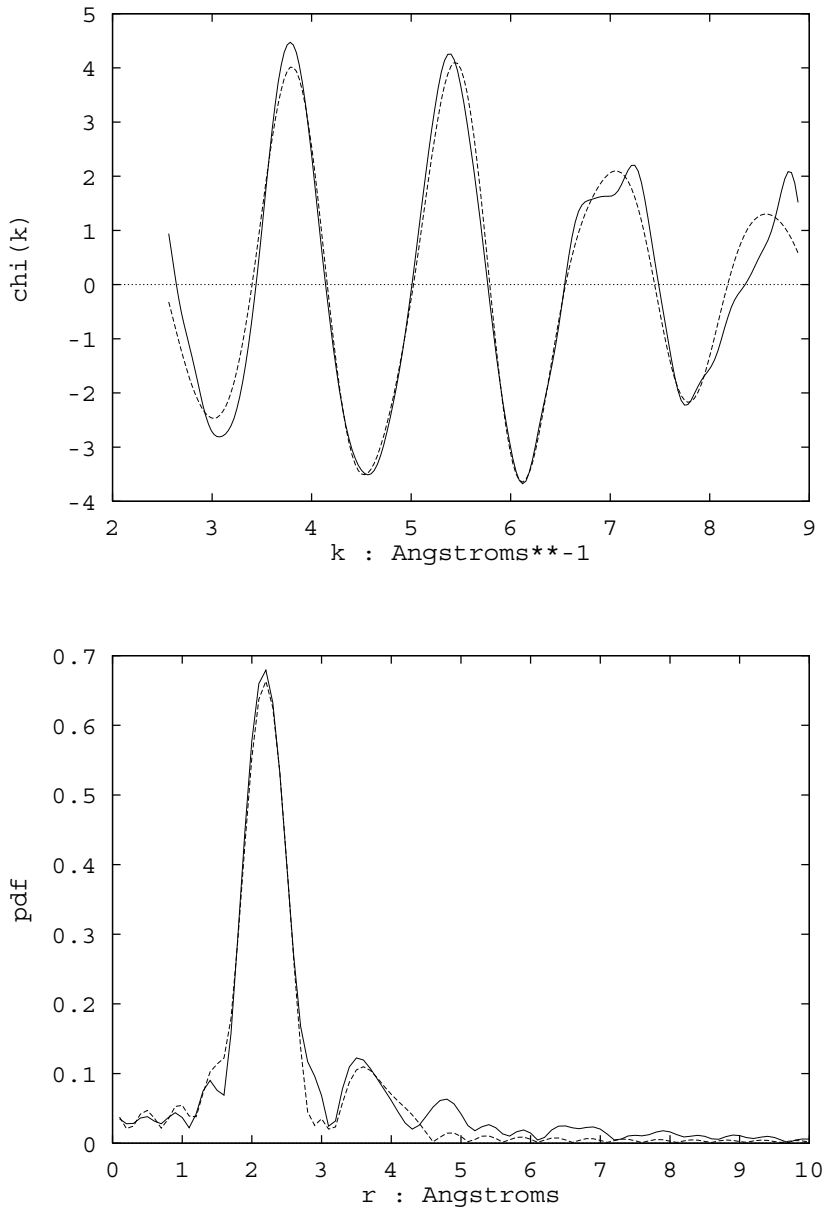

Figure 67: Top: Europium metaphosphate glass EXAFS $\chi(k)$, Bottom: Europium metaphosphate glass EXAFS pdf

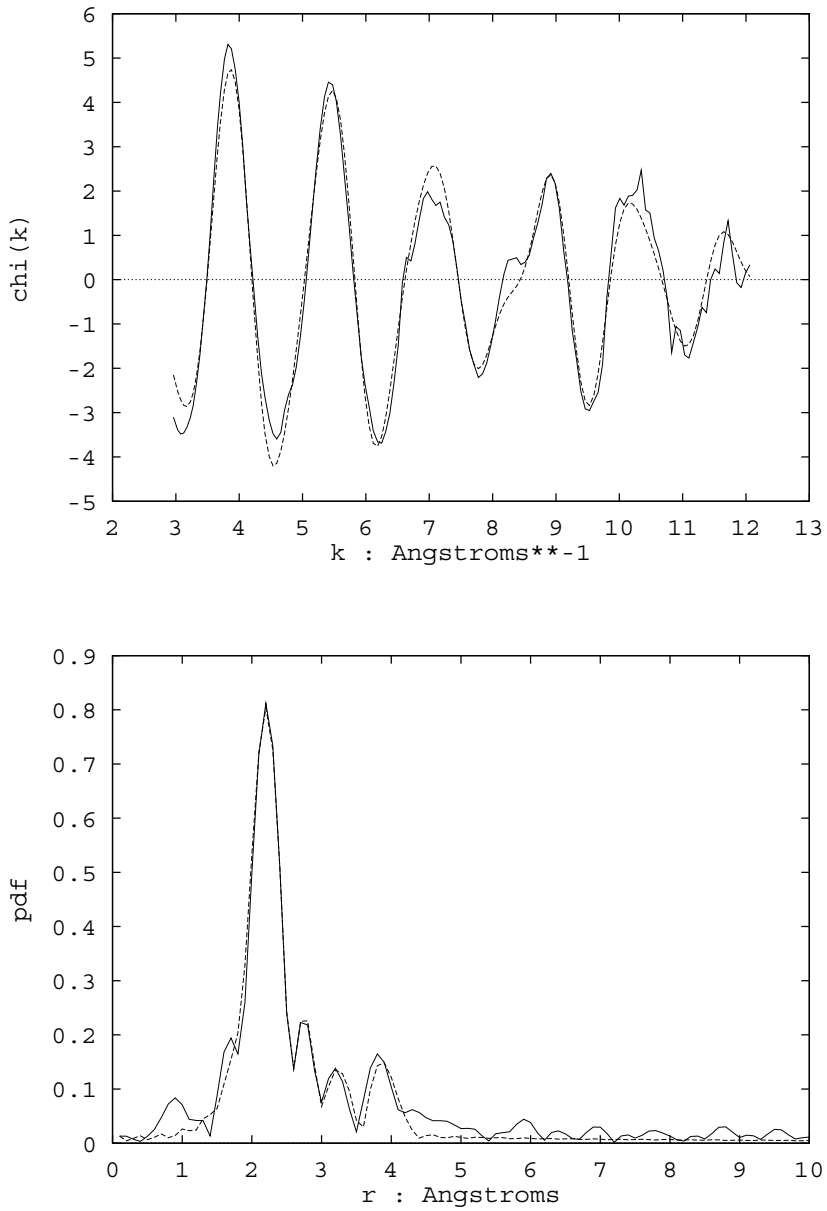

Figure 68: Top: Gadolinium metaphosphate glass EXAFS $\chi(k)$, Bottom: Gadolinium metaphosphate glass EXAFS pdf

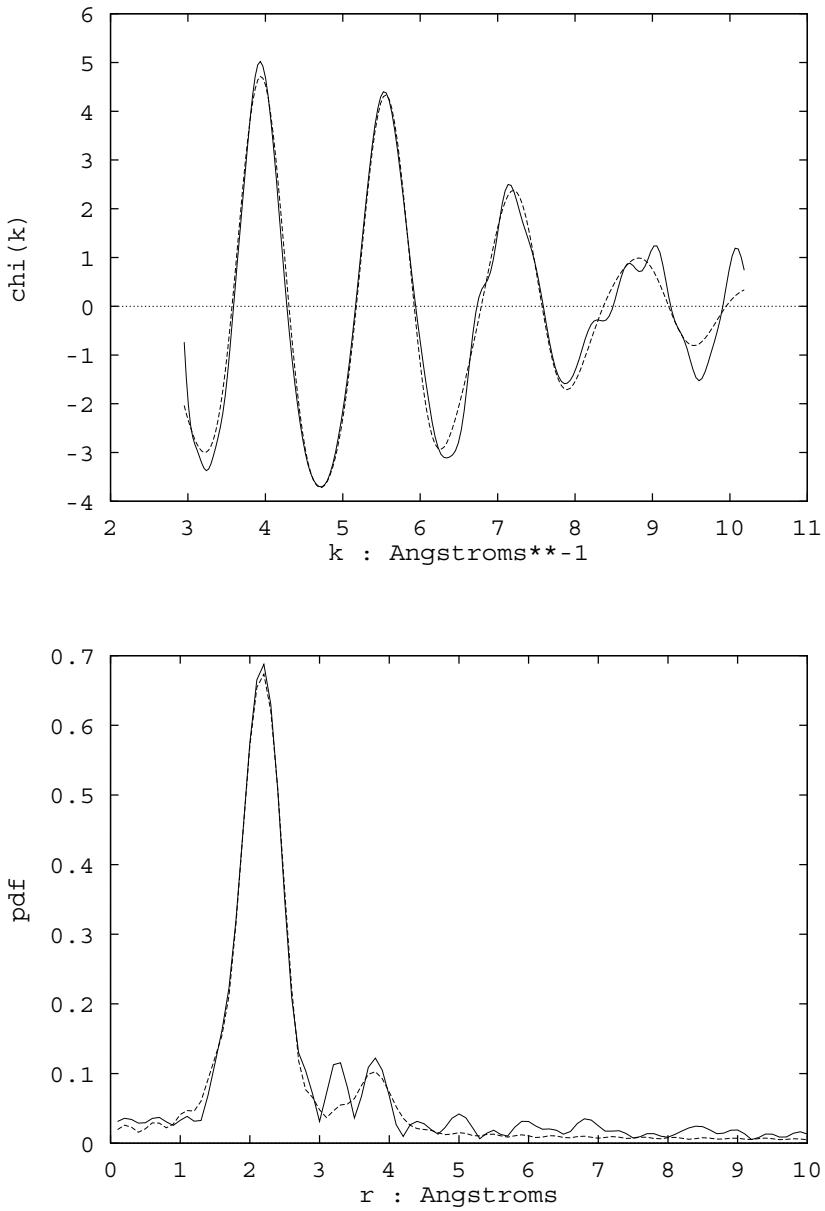

Figure 69: Top: Terbium metaphosphate glass EXAFS $\chi(k)$, Bottom: Terbium metaphosphate glass EXAFS pdf

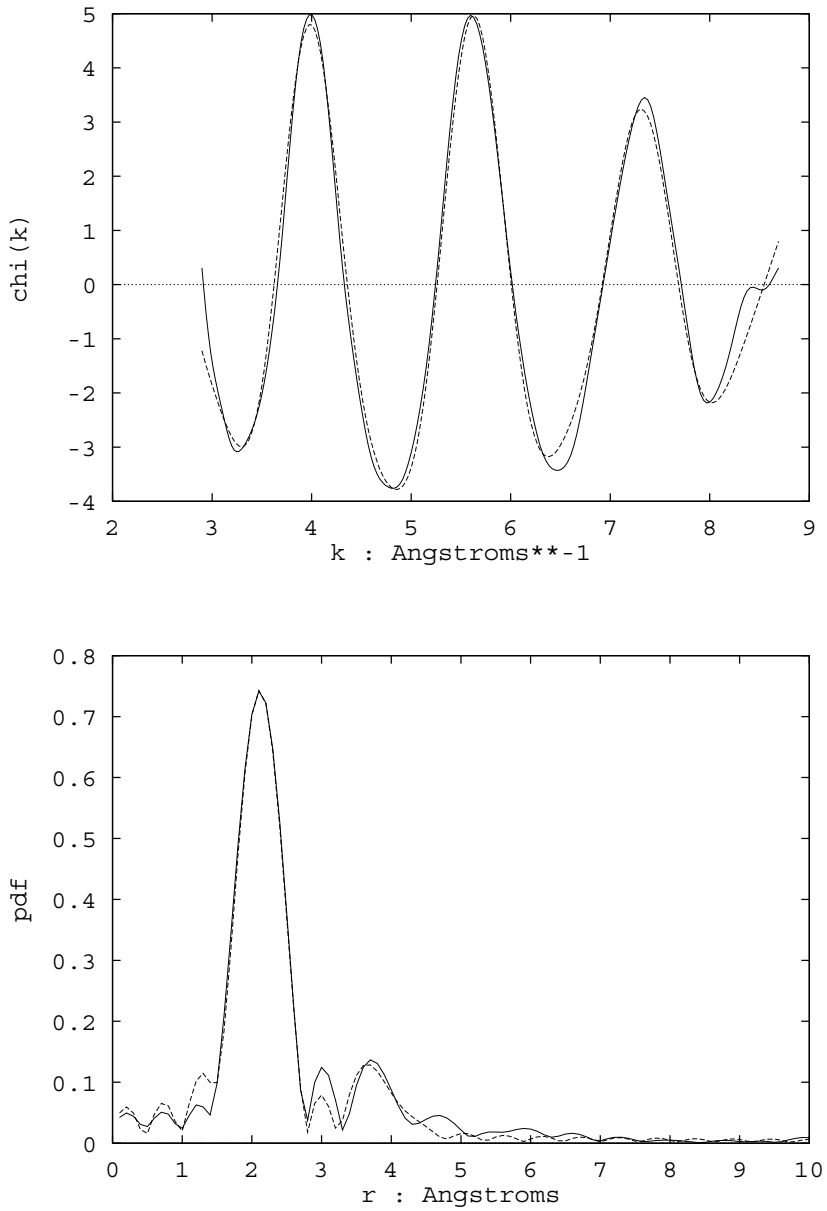

Figure 70: Top: Holmium metaphosphate glass EXAFS $\chi(k)$, Bottom: Holmium metaphosphate glass EXAFS pdf

has a high degree of crosslinkage between the PO_4 units, mediated by the incorporated rare earth ions. This high level of crosslinkage could play a significant part in the observed increased resistance to hygroscopic attack displayed by these glasses over other phosphate systems. The magnitude of the higher correlations visible in the diffraction $t(r)$ corroborate the coordination numbers obtained from the EXAFS data.

The evidence for the Lanthanide contraction being visible in metaphosphate glass systems is demonstrated by both the diffraction and EXAFS results. This trend being most clearly shown in the tabulated EXAFS results (Table 11), but also being visible in the second correlation distances extracted from the diffraction $t(r)$ (Tables 7,8 and 9).

The EXAFS data also show that there is no evidence for clustering of the rare earth ions within the glass, at least not on the short length scales probed by this technique. This fact has important implications for understanding the mechanisms that govern the physical properties of these glasses, for example their magnetic properties and optical properties.

Chapter 10

Conclusions

10.1 Fibre optic preforms

The application of the EXAFS and X-ray diffraction techniques to spatially resolved studies of the core region of fibre optic preforms, has proven to be an extremely challenging problem. The use of a synchrotron radiation source for provision of X-rays, has been a vital aspect of the project; the small sample areas and dilute dopant species of interest demanding extremely high photon flux levels. Even so, this project to study the rare earth and codopant local atomic environments within the bulk silica matrix, has pushed currently available technology to it's utmost limits. The demand being for higher incident flux to improve counting statistics and to allow for smaller probing beam sizes.

The use of EXAFS to probe the rare earth site was attempted but due to the very low concentrations of these atomic species within the sample, obtaining analysable data has proved to be impossible with current facilities. Although it has been possible to measure concentration profiles across the core region demonstrating the correlation

between dopant species, erbium and germanium, and emphasising the need for spatially resolved studies if the physical properties of doped fibre preforms are to be fully understood. The performance of fluorescence mode EXAFS experiments would have proved to be a great advantage but unfortunately the gain in concentration sensitivity was outweighed by the loss of detected photon flux, resultant from the small solid angle subtended by the standard fluorescence detectors, and the very small sample volumes being probed. A possible improvement to the experimental system, that may yield improved results would be the use of a closely positioned fluorescence detector that could maximize the solid angle through which fluorescence photons can be detected.

Transmission EXAFS experiments were performed at the erbium edge of the higher dopant concentration samples, but proved that as expected these concentrations typically 1 wt.%, were too low to yield data of analysable quality via this technique. The difficulty being in obtaining an edge-step of significant size, necessary for data normalization, and minimisation of signal to noise errors evident in the collected data. The fluorescence experiments led to the detection of the absorption edge, but yielded an EXAFS signal devoid of significant oscillatory features, again due to the poor signal obtained from the small sample area being probed.

The diffraction experiments were useful mainly to prove that the bulk glass structure of the preforms is fused silica, and that the incorporation of the dopant atoms does little to distort the atomic matrix over the longer length scales. Attempts at differential anomalous X-ray scattering were made in an attempt to obtain local structural information relating to the germanium codopant site within the silica, but were foiled by the unsuitability of the Daresbury source, for this kind of work. This again is an area that further work may lead to fruitful results, although currently the problems

that would have to be overcome are significant, not least an improved understanding of how to perform accurate incoherent scattering corrections to diffraction data, suffering from increased contamination from fluorescence and resonant Raman effect events; these being due to data collection near an X-ray absorption edge of one of the sample constituent elements.

Other work that would be particularly useful to the ultimate goal of obtaining definitive short range structural information as to the kind of site occupied by the rare earth ions doped into a silica matrix, would be the performance of the above techniques on a series of doped silica samples prepared with much higher concentrations of dopant species, this could only really be achieved with rare earth dopants if Al_2O_3 were one of the codopants to help disperse the rare earth ions and prevent clustering. This would be a worthwhile study in itself as the mechanisms governing the incorporation of metal ions into silicate glasses are still not fully understood [30]. These samples are of little interest to the optics community due to having very poor optical properties, but would prove useful as benchmark standards upon which to build structural models.

Useful information as to some structural aspects of the fibre preforms was obtained, particularly with the relation to the germanium codopant incorporated into the silica matrix to raise the refractive index of the core region of the preform, and ultimately the fibre. Notably the occupation of eightfold, oxygen coordinated sites by the germanium ions, most likely being bonded in an ionic fashion. Evidence for a significant degree of correlation between the germanium and erbium sites was found by comparison of the concentration profile maps obtained by measuring the absorption of the sample as a function of position of the incident beam upon the core, at the erbium L_{III} and germanium K absorption edges. More definitive information

could possibly be gained if these EXAFS experiments at the germanium K edge were reperformed on an instrument allowing a larger energy range of data collection, a short limit being imposed by the focussing mirror used to increase the incident flux on station 8.1 at the SRS, Daresbury.

10.2 Metaphosphate glasses

The diffraction and EXAFS results obtained from the rare earth metaphosphate glass samples prove the power of application of a combination of analysis techniques to the structural study of amorphous materials. These samples being particularly well suited to both a diffraction and EXAFS study, and also available in a range of compositions allowing for trend analysis of the effects of variation in the species of rare earth inclusion in the bulk phosphate network.

The results obtained, allow the foundations of a structural model for these types of glasses to be laid, building upon much of the current models for phosphate glasses in general. Further work on model structures is probably best pursued by application of the developing range of advanced computational techniques currently being investigated by various research groups for example, Reverse Monte Carlo (RMC) modelling and Molecular Dynamics (MD) techniques. These techniques are too specialised for detailed introduction in this work and descriptions can be found in many texts for example [89, 15].

In addition to the X-ray techniques applied in this work, other techniques would also provide much complementary information relating to these glasses, notably neutron diffraction, where the weightings to the contributions from the various *partial* distribution functions i.e. from the atomic pair correlations that contribute to the

diffraction *t(r)*, would accentuate the contribution to the total *t(r)* from the phosphate network, rather than the heavy weighting in favour of the rare earth elements probed by X-ray diffraction. This information allowing yet another complementary piece of information to be used in building model structures. Techniques such as Raman spectroscopy can also provide much useful information on the lattice properties of the atomic network although this is an indirect probe and it can often prove difficult to interpret the results meaningfully.

Further areas worth investigating for the improvement of the X-ray work performed on these glasses could come with the study of some well characterised calibration samples, particularly useful for fixing parameters in the EXAFS analysis, critical for accurate determination of physical properties. Such calibrant compounds would have to be of known crystal structure and preferably of a similar chemical composition to the metaphosphate glasses so as to provide a relatively comparable environment for the electron scattering processes involved in EXAFS. Suitable compounds of rare earth salts are not easy to obtain and often suffer problems of environment sensitivity requiring data collection in controlled atmospheres, such as under nitrogen or argon. Problems which would have to be overcome if useful data were to be obtained.

The work presented here has demonstrated the power of a combined EXAFS and Diffraction approach to structural determination, and in combination with the range of samples studied, much useful information has been obtained. Notably the determination that the rare earth ions are incorporated into the phosphate glass in highly coordinated sites, with coordinations on average of between 6 and 8 oxygen atoms about each rare earth ion, the discovery that the Lanthanide contraction is visible across the range of metaphosphate glasses studied and that no evidence is found for clustering of rare earth ions within the bulk phosphate glass matrix.

10.3 Closing remarks

Throughout this work, the main aim was to isolate structural information relating to rare earth doped glasses, this being pursued in the study of the core region of silicate glass fibre optic preforms, an area of current industrial interest, and in the study of rare earth doped metaphosphate glasses, materials which currently hold mainly academic interest, may in future play key roles in optical and magnetic devices.

The techniques used to probe these glasses were chosen for their complementary nature, i.e. the short range and atomic type specific probe EXAFS and the more general and short/medium range structural probe, X-ray diffraction. Their combination has been shown to be highly successful in elaborating on the information each technique alone could obtain, and through combination, a degree of calibration was obtained even in the absence of what would usually be vital calibration compounds.

Ideally, it would have been desirable to have access to a higher photon flux than present synchrotron facilities offer, but even without this advantage useful data was still been obtained, albeit in a more inferred fashion than usual. Advances in synchrotron radiation technology on both the production and detection sides should soon lead to the routine performance of experiments on systems as challenging as the fibre optic preforms. Advances in computational analysis procedures may also hold the key to viable model structure generation, but as yet, these remain problems for the future.

Appendix A

Publications

- 'EXAFS and X-ray Structural Studies of $(Tb_2O_3)_{0.26}(P_2O_5)_{0.74}$ Metaphosphate Glass', D.T.Bowron, R.J.Newport, B.D.Rainford, G.A.Saunders and H.B.Senin.

  Conference paper presented at the American Crystallographic Association Annual Meeting 1994, Atlanta, Georgia, U.S.A
  Full version submitted for publication

- 'An X-ray Absorption Study of Doped Silicate Glass, Fibre Optic Preforms', D.T.Bowron, R.J.Newport, J.S.Rigden, E.J.Tarbox and M. Oversluizen.
  Submitted for publication

- 'EXAFS studies of Rare Earth Metaphosphate Glasses', D.T.Bowron, R.J.Newport, B.D.Rainford, G.A.Saunders and H.B.Senin.
  In preparation

- 'X-ray diffraction studies of Rare Earth Metaphosphate Glasses', D.T.Bowron, R.J.Newport, B.D.Rainford, G.A.Saunders and H.B.Senin.
  In preparation

Appendix B

Shots in the dark, or 'firing blanks'

In the course of this project, several experimental techniques were applied with less than glowing success, the motivation being to attempt to elucidate more about the structure of the rare earth doped fibre preform samples. Notably first order difference anomalous X-ray scattering and fluorescence/transmission EXAFS at the rare earth L_{III} absorption edge were tried. There follows a few words on the conclusions that were drawn from these attempts.

B.1 Anomalous X-ray scattering

As mentioned in chapter 3, the variation in the atomic scattering factors close to an elemental X-ray absorption edge can be used to advantage in the technique of Anomalous X-ray Scattering (AXS) [67, 90]. The principle being to make use of the difference in an element's scattering potential close to one of its absorption edges,

to separate out some of the partial terms contributing to the general composite X-ray diffraction radial distribution function. In theory, if enough experiments are performed changing the scattering potentials of all the elements present in the sample, the individual pair correlation functions for each atom type can be isolated. However, in practice this has proved beyond current ability as there are many effects that are not understood in sufficient detail to allow adequate data correction. A simplification of the technique is first order difference AXS, where two experiments are performed at differing X-ray wavelengths close to one of the sample's constituent element absorption edges. Once these measurements have been made, a difference between the two should theoretically lead to a isolation of a partial radial distribution function where all the contributing correlations include the element who's edge is being probed. This is very similar to the kind of function obtained from an EXAFS experiment. An illustration of two diffraction patterns taken for sample PD265 at wavelengths corresponding to X-ray photon energies 100 and 500eV below the germanium K absorption edge is shown in Figure 71.

In practice the experiments are identical to those of conventional diffraction, except that two wavelengths of incident X-rays are chosen, close to an absorption edge relevant to the sample. Each data set obtained is analysed as a normal X-ray diffraction experiment until an interference function $i(k)$ has been produced. At this point a difference between the two functions labelled $i(k)_{E1}$ and $i(k)_{E2}$ for convenience, is taken resulting in a difference function $i(k)_d$ i.e.

$$i(k)_d = i(k)_{E1} - i(k)_{E2} \tag{101}$$

This difference function can then be Fourier transformed to produce a partial distribution function.

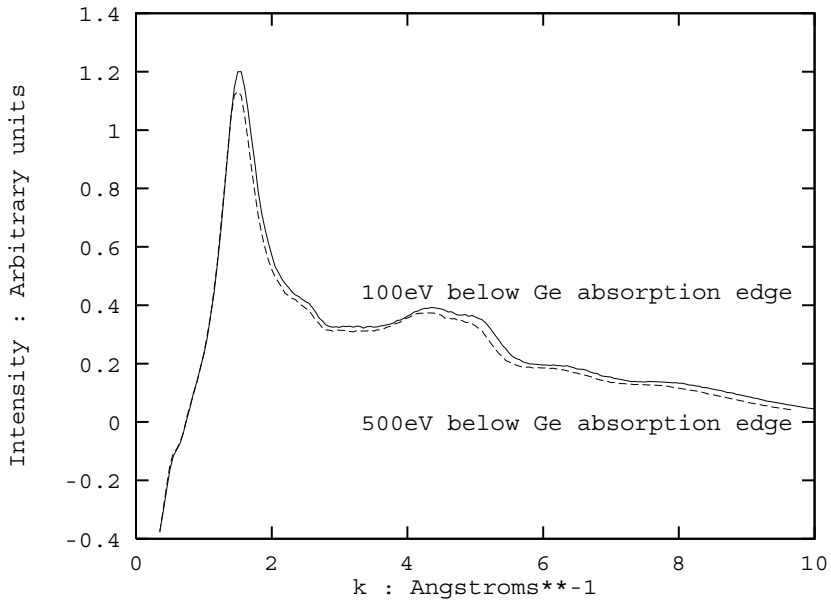

Figure 71: Diffraction patterns measured for central core region of sample PD265 at X-ray energies 100 and 500eV below the *Ge* K-edge (11104eV)

The first order difference experiments attempted upon the rare earth doped fibre preform samples were performed close to the germanium K absorption edge (11104eV). The energies chosen being 50, 100 and 500eV below the edge, three energies being taken in an attempt to increase the chances of finding an optimum combination - the closer to the absorption edge the greater the change in scattering potential, but the greater the necessary corrections for parasitic effects such as X-ray fluorescence and resonant Raman scattering [65, 66].

On attempting an analysis of the data it was discovered that, as yet, it is impossible to correct for many experimental factors; this failure leading to unphysical artifacts in the obtained difference function that completely dominated the data. It is believed that the instability of the X-ray beam at the Daresbury source was a major contributing factor to the problems encountered; beam instabilities making accurate calibration of incident wavelength difficult, as incidence angles for the white

radiation of the source upon the monochromator can vary with time and hence affect the transmitted wavelength. Also, no truly adequate methods of correcting the data for the parasitic effects of fluorescence, resonant Raman scattering or Compton scattering have yet been developed. In addition the problems of a poor signal to noise ratio are significant, since the change in the scattering profiles is of the order of a few percent, and the low statistical quality of the data becomes a hindrance once the difference function is obtained. In the course of investigations into the $i(k)$ it was found that these depend critically upon the fitting of the self scattering contribution if a usable difference function is to be obtained; a serious problem if oscillations persist in the diffraction signal out to high angles; this being associated with the necessity for choosing wavelengths corresponding to an element's absorption edge, hence the wavelength is often restricted to values that preclude the collection of data at large k.

B.2 EXAFS

EXAFS at the rare earth L_{III} absorption edge for the fibre preform samples was extremely problematic. Difficulties arose from the very low concentration of rare earth ions within the silica glass, coupled with the need for small incident X-ray beam sizes to probe the core region of the preform. An unfortunate side effect of the small beam size required for spatial resolution is the reduction in incident photon flux at the sample.

For the study of dilute systems by EXAFS, the fluorescence geometry is preferable, this being a more sensitive technique when low concentrations of the atomic species to be probed are all that is present within the sample.

A problem which arose from studying the small core regions of the preforms resulted from the large size of the fluorescence detector available on the experimental station. The size of the detector precluded close placement to the sample, once mounted on the collimation stage; this meant that only a small solid angle for detection of the fluorescence photons was subtended by the detector, compounding the problem of low flux produced by the pinhole collimation system.

A solution to the problem of low counting statistics may be to use a much smaller fluorescence detector allowing closer placement to the sample. This was tried with a single photomultiplier tube and demonstrated the feasibility of the approach, although usable data was not attainable as the supporting electronics allowing energy windowing of the fluorescence signal was not available at the time. This energy windowing is vital if contaminant fluorescence effects are to be minimised in the collected data.

In an attempt to obtain EXAFS from the slightly higher concentration doped samples (e.g. sample ND204: 1 wt% Er_2O_3), transmission experiments were tried (Figure 72). As expected, the concentrations of rare earth ions were too low to give a significant edge-step in the data when the experiments were performed in the conventional transmission geometry. Some signal was evident in the data that was obtained (Figure 73), although the signal to noise ratio was particularly poor and definitive information could not be obtained. It was however possible to obtain some tentative information regarding first and second shell atom types and distances, even from data of this poor quality for sample ND204. Coordination numbers were not accessible due to the lack of any significant edge step within the data. Scans were made using a 100 micron diameter X-ray beam spot, data being taken at the centre, mid and edge of core regions of the fibre preform. An example of the type of fit

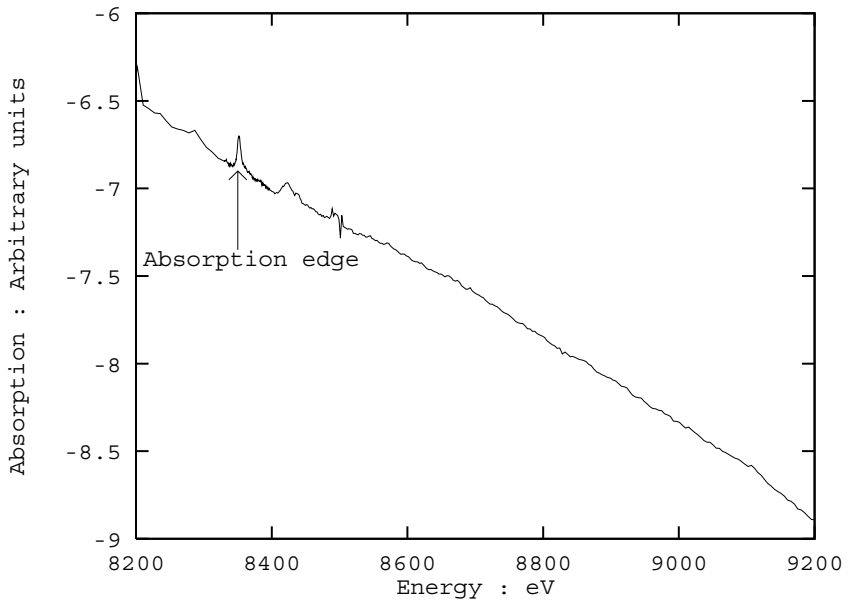

Figure 72: Transmission X-ray absorption spectrum obtained on the central core region of sample ND204

attempted is shown in Figure 74 and the shell assignments are given in table 12, the associated error with the distance value is large and these tables only illustrate the possibilities for future work if instrumentation limitations can be overcome.

Edge of core	
Atom correlation	Distance Å
$Er - O$	2.32
$Er - Er$	3.57

Mid Point of core	
Atom correlation	Distance Å
$Er - O$	2.41
$Er - Er$	3.68

Center of core	
Atom correlation	Distance Å
$Er - O$	2.42
$Er - Er$	3.67

Table 12: Er L_{III} edge transmission EXAFS fit parameters

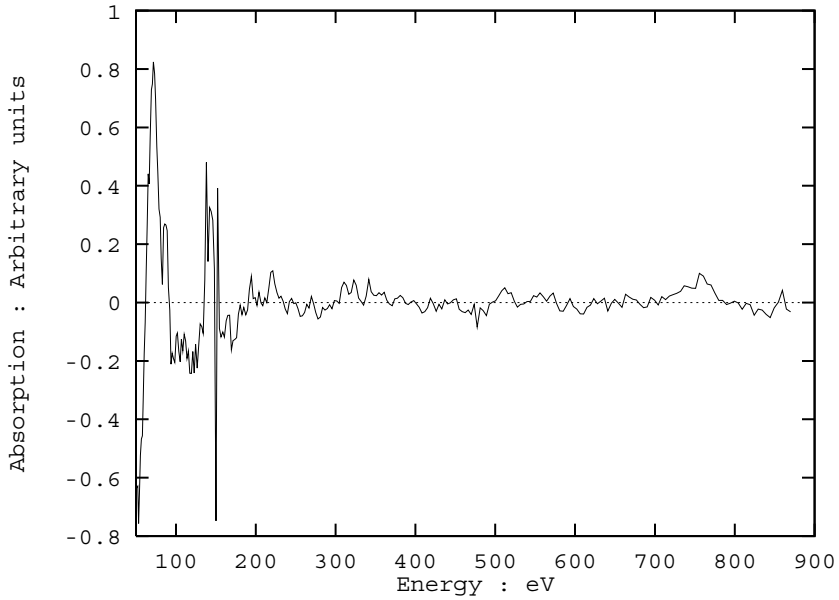

Figure 73: Isolated EXAFS signal obtained for the central core region of sample ND204

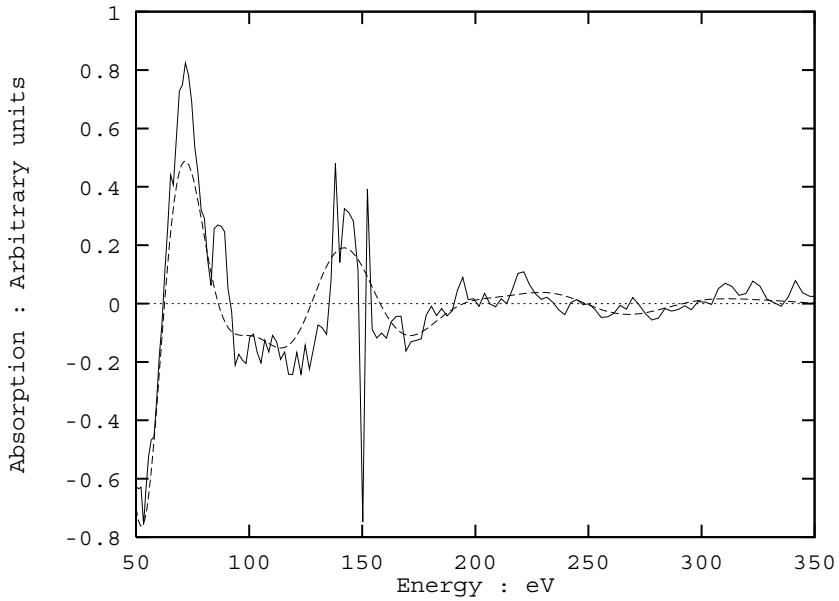

Figure 74: EXAFS signal and fit for central core region of sample ND204

B.3 Future possibilities

The above mentioned techniques and their application to systems of this complexity may soon become viable with the next generation of synchrotron sources being constructed. These new sources offer a much higher photon flux and increased stability over those currently available. Both techniques would benefit greatly from the improved statistical accuracy offered by a high intensity source such as the newly proposed MEXS [1], and the spatially resolved studies of the fibre preform samples would in addition benefit from a high brilliance source such as the ESRF [2]; AXS in particular would benefit from the increased stability of the beam.

Other instrumental improvements that could have significant impact on future work such as AXS, is the development of image plate technology for the collection of diffraction data. This offers the possibility to collect data of high statistical quality, due to not restricting the data collection to a single scattering plane. The choice of systems suitable for study by AXS could be also improved, since probing the germanium K-edge restricts the effective **k**-range, making the fitting of the self scattering profile extremely difficult. Systems containing elements with higher energy absorption edges of suitable characteristics may allow a more successful application of the technique.

[1] Medium Energy X-ray Source, proposed to replace the SRS towards the turn of the century.

[2] European Synchrotron Radiation Facility, Grenoble, France. - Currently in commissioning stages.

Bibliography

[1] W.H.Zachariasen. *J. Amer. Chem. Soc.*, **54**:3841–3851, 1932.

[2] B.E.Warren. *Z. Krist.*, **86**:349–358, 1933.

[3] R.J.Bell and P.Dean. *Nature*, **212**:1354–1356, 1966.

[4] R.J.Bell and P.Dean. *Phil. Mag.*, **25**:1381–1398, 1972.

[5] R.L.Mozzi and B.E.Warren. *J. Appl. Cryst.*, **2**:164–172, 1969.

[6] P.H.Gaskell and I.D.Tarrant. *Phil. Mag. B*, **42**:265–286, 1980.

[7] W.Y.Ching. *Phys. Rev. B*, **26(12)**:6610–6621, 1982.

[8] L.F.Gladden. *J. Non-Cryst. Solids*, **119**:318–330, 1990.

[9] N.Valenkov and E.Poray-Koshitz. *Z. Krist.*, **95**:195–229, 1936.

[10] J.C.Phillips. *Solid State Physics*, **37**:93–171, 1982.

[11] J.C.Phillips. *J. Non-Cryst. Solids*, **63**:347–355, 1983.

[12] R.Hosemann, M.P.Hentschel, and U.Schmeisser. *J. Non-Cryst. Solids*, **83**:223–234, 1986.

[13] S.R.Elliott. *Nature*, **354**:445–452, 1991.

[14] S.R.Elliott. *J. Phys.: Condens. Matter*, **4**:7661–7678, 1992.

[15] N.E.Cusack. *The Physics of Structurally Disordered Matter.* Adam Hilger, 1988.

[16] R.W.G.Wyckoff. *Crystal Structures, Volume 1.* Robert E. Krieger Publishing Company, Malabar, Florida, 1982.

[17] F.L.Galeener and A.C.Wright. *Solid State Comm.*, **57(8)**:677–682, 1986.

[18] G.N.Greaves. *J. Non-Cryst. Solids*, **71**:203–217, 1985.

[19] J.Van Wazer. *Phosphorus and its Compounds Vol II.* Interscience Publishers, New York, 1951.

[20] S.W.Martin. *Eur. J.Solid State Inorg. Chem.*, **28**:163–205, 1991.

[21] A.Mierzejewski, G.A.Saunders, H.A.A.Sidek, and B.Bridge. *J. Non-Cryst. Solids*, **104**:323–332, 1988.

[22] A.Musinu, G.Piccaluga, and G.Pinna. *J. Non-Cryst. Solids*, **111**:221–227, 1989.

[23] A.Musinu, G.Piccaluga, and G.Pinna. *J. Non-Cryst. Solids*, **122**:52–58, 1990.

[24] B.C.Sales. *J. Non-Cryst. Solids*, **119**:136–150, 1990.

[25] Y.Kowada, H.Adachi, and T.Minami. *J. Phys. Chem.*, **97**:8989–8992, 1993.

[26] G.N.Greaves, S.J.Gurman, L.F.Gladden, C.A.Spence and P.Cox, B.C.Sales, L.A.Boatner, and R.N.Jenkins. *Phil. Mag. B*, **58(3)**:271–283, 1988.

[27] Ya.S.Bobovich. *Opt. Spect.*, **13**:274 – 277, 1962.

[28] K.Sun and Jr. W.M.Risen. *Solid State Comm.*, **60(9)**:697 – 700, 1986.

[29] Paul Urquhart. *IEE Proceedings*, **135(6)**:385–407, 1988.

[30] V.McGahay and M.Tomozawa. *J.Non-Cryst. Solids*, **159**:246–252, 1993.

[31] C.K.Kao. *Optical Fibre*. Peter Peregrinus Ltd. for the IEEE, 1988.

[32] B.Kikuchi et al. *Fujitsu Sc. Tech. J.*, **11**:99, 1975.

[33] E.Desurvire. *Physics Today*, **Jan.**:20–27, 1994.

[34] M.J.F.Digonnet and C.J.Gaeta. *Applied Optics*, **24(3)**:333–342, 1985.

[35] M.Artiglia, P.DiVita, and M.Potenza. *J.Opt.Commun.*, **13(3)**:104–113, 1992.

[36] B.Pedersen, A.Bjarklev, H.Vendeltorp-Pommer, and J.H.Povlsen. *Optics Communications*, **81(1,2)**:23–26, 1991.

[37] R.I.Laming, J.E.Townsend, D.N.Payne, F.Meli
and G.Grasso, and E.J.Tarbox. *IEEE Photon. Tech. Lett.*, **3(3)**:253–255, 1991.

[38] N.Edagawa, S.Yamamoto, H.Taga, and M.Suzuki
and H.Wakabayashi. 2nd international conference on optical fibre submarine telecommunications systems. Conference Proceedings : SUBOPTIC 1993, April 1993. pp: 55-60.

[39] P.L.Scrivener, P.D.Maton, A.P.Appleyard, and E.J.Tarbox. *Electron. Lett.*, **26(13)**:872–873, 1990.

[40] A.P.Appleyard, P.L.Scrivener, and P.D.Maton. *Rev. Sci. Instrum*, **61(10)**:2650–2654, 1990.

[41] R.Kashyap, J.R.Armitage, R.J.Campbell, D.L.Williams
and G.D.Maxwell, B.J.Ainslie, and C.A.Millar. *BT Technol. J.*, **11(2)**, 1993.

[42] R.M.Atkins and V.Mizrahi. *Electron. Lett.*, **28(18)**:1743–1744, 1992.

[43] S.B.Poole, D.N.Payne, R.J.Mears, M.E.Fermann, and R.I.Laming. *J. Lightwave Tech.*, **LT-4(7)**:870–876, 1986.

[44] T.F.Morse, L.Reinhart, A.Kilian, W.Risen Jr., and J.W.Cipolla Jr. *Proc. SPIE Fibre Laser Sources and Amplifiers*, **1171**:72–79, 1989.

[45] J.A.Bebbington, G.Barbarossa, J.R.Bonar, and J.S.Aitchison. *Appl. Phys. Lett.*, **62(4)**:337–339, 1993.

[46] J.E.Townsend, S.B.Poole, and D.N.Payne. *Electron. Lett.*, **23(7)**:329–331, 1987.

[47] B.J.Ainslie, S.P.Craig, and S.T.Davey
and B.Wakefield. *Materials Letters*, **6(5,6)**:139–144, 1988.

[48] B.E.Warren. *X-ray Diffraction.* Dover Publications, New York, 1990.

[49] D.W.Huxley. *Diffraction Studies of Amorphous Materials.* PhD thesis, The University of Kent at Canterbury, England, 1991.

[50] N.S.Gingrich. *Rev. Mod. Phys.*, **15(1)**:90–110, 1943.

[51] K.Furukawa. *Repts. Prog. Phys.*, **25**:395–440, 1962.

[52] R.F.Kruh. *Chem. Rev.*, **62**:319–346, 1962.

[53] H.H.Palman and C.J.Pings. *Rev. Mod. Phys*, **35(2)**:389–399, 1963.

[54] C.H.Macgillavry and G.D.Rieck, editors. *International Tables of X-ray Crystallography*, volume III. Kynoch, 2nd edition, 1968.

[55] J.Waser and V.Schomaker. *Rev. Mod. Phys.*, **25(3)**:671–690, 1953.

[56] P.A.Lee and J.B.Pendry. *Phys. Rev. B*, **11(8)**:2795–2811, 1975.

[57] E.A.Stern. *Phys. Rev. B*, **10(8)**:3027–3037, 1974.

[58] P.A.Lee, P.H.Citrin, P.Eisenberger, and B.M.Kincaid. *Rev. Mod. Phys.*, **53(4) Part 1**:769–806, 1981.

[59] D.C.Koningsberger and R.Prins, editors. *X-Ray Absorption, Principles, Applications, Techniques of EXAFS, SEXAFS, and XANES.* John Wiley & Sons, 1988.

[60] B.K.Teo. *EXAFS: Basic Principles and Data Analysis.* Springer-Verlag, 1986.

[61] S.S.Hasnain, editor. *Synchrotron Radiation and Biophysics*, chapter 1. Ellis-Horwood, 1990. Chapter author S.J.Gurman.

[62] S.J.Gurman. *J.Phys.C: Solid State Physics*, **21**:3699–3717, 1988.

[63] S.J.Gurman, N.Binsted, and I.Ross. *J.Phys.C: Solid State Physics*, **17**:143–151, 1984.

[64] C.R.A.Catlow and G.N.Greaves. *Chemistry in Britain*, **Sept.**:806–809, 1986.

[65] C.J.Sparks Jr. *Phys.Rev.Lett.*, **33(5)**:262–265, 1974.

[66] P.Eisenberger, P.M.Platzman, and H.Winick. *Phys.Rev.B*, **13(6)**:2377–2380, 1976.

[67] P.H.Fuoss. *Structural Studies of Amorphous Materials Using X-ray Anomalous Scattering.* PhD thesis, Standford University, USA, 1980. Standford Synchrotron Radiation Laboratory Report No. 80/06.

[68] B.E.Warren and G.Mavel. *Rev.Sci.Instr.*, **36**:196, 1965.

[69] G.Bushnell-Wye, J.L.Finney, J.Turner, and D.W.Huxley and J.C.Dore. *Rev.Sci.Instr.*, **63**:1153–1155, 1992.

[70] D.T.Cromer and J.T.Waber. *Acta Cryst.*, **18**:104, 1965.

[71] J.A.Ibers and W.C.Hamilton, editors. *International Tables for X-ray Crystallography*, volume IV. Kynoch Press, 1974.

[72] F.Hajdu. *Acta Cryst.*, **A27**:73, 1971.

[73] F.Hajdu. *Acta Cryst.*, **A28**:250, 1972.

[74] J.Krogh-Moe. *Acta Cryst*, **9**:951–953, 1956.

[75] N.Norman. *Acta Cryst.*, **10**:370–373, 1956.

[76] J.Chaboy, J.García, A.Marcelli, and M.F.Ruiz-López. *Chem. Phys. Lett.*, **174(5)**:389–395, 1990.

[77] P.D'Angelo, A.Di Cicco, A.Filipponi, and N.V.Pavel. *Phys.Rev.A*, **47(3)**:2055–2063, 1993.

[78] J.Chaboy and T.A.Tyson. *Phys. Rev. B*, **49(9)**:5869–5875, 1994.

[79] N.Binsted, J.W.Campbell, S.J.Gurman, and P.C.Stephenson. *EXCURV90.* SERC Daresbury Laboratory, Daresbury, Warrington, Cheshire, UK. EXAFS Analysis Suite program (1991).

[80] P.D.Cluskey. Structural analysis of metal clusters using EXAFS. Master's thesis, The University of Kent at Canterbury, England, 1992.

[81] R.W.Joyner, K.J.Martin, and P.Meehan . *J.Phys.C: Solid State Physics*, **20**:4005–4012, 1987.

[82] S.J.Gurman, R.J.Newport, M.Oversluizen, and E.J.Tarbox. *Physics and Chemistry of Glasses*, **33(1)**:30–32, 1992.

[83] D.W.Oblas, T.Wei, W.J.Miniscalco, and B.T.Hall. *Mat. Res. Soc. Symp. Proc.*, **172**:315–320, 1990.

[84] M.A.Marcus and A.Polman. *J. Non-Cryst. Solids*, **136**:260–265, 1991.

[85] J.Wang, W.S.Brocklesby, J.R.Lincoln, J.E.Townsend, and D.N.Payne. *J.Non Cryst. Sol.*, **163**:261–267, 1993.

[86] E.Delevaque, T.Georges, M.Monerie, P.Lamouler, and J.F.Bayon. *IEEE Phot. Tech. Lett.*, **5(1)**:73–75, 1993.

[87] SERC Daresbury Laboratory, Daresbury, Warrington, Cheshire, UK. *EXCALIB.* EXAFS Analysis Suite program.

[88] SERC Daresbury Laboratory, Daresbury, Warrington, Cheshire, UK. *EXBACK.* EXAFS Analysis Suite program.

[89] J.D.Wicks. *Studies of disordered materials.* PhD thesis, Lincoln College, Oxford University, 1993.

[90] J.B.Suck, D.Raoux, P.Chieux, and C.Riekel, editors. *Methods in the Determination of Partial Structure Factors.* World Scientific, 1993.